

Copyright

by

Jason Michael Haber

2016

**The Dissertation Committee for Jason Michael Haber Certifies that this is the approved version of the following dissertation:**

**Microfluidic PCR With Plasmonic Imaging for Rapid Multiplexed  
Characterization of DNA from Microbial Pathogens**

**Committee:**

---

Konstantin Sokolov, Co-Supervisor

---

Peter Gascoyne, Co-Supervisor

---

James Bankson

---

Xiang-Yang Han

---

David Hawke

**Microfluidic PCR With Plasmonic Imaging for Rapid Multiplexed  
Characterization of DNA from Microbial Pathogens**

**by**

**Jason Michael Haber, B.S.B.E.**

**Dissertation**

Presented to the Faculty of the Graduate School of

The University of Texas at Austin

in Partial Fulfillment

of the Requirements

for the Degree of

**Doctor of Philosophy**

**The University of Texas at Austin**

**December 2016**

## **Dedication**

To my wife, Emily-

When you first read this note, it will have been a year since we were married. I'm quite confident it will have been a year full of joy and wonder, surpassing even the amazing times we've had together so far. I am so thankful to you for your support and never-ending patience with me as I finished my experiments and dissertation, and for propping me up when I wasn't sure I could pull it off. You mean everything to me, and I hope to continue to see your smile for the rest of my life.

## **Acknowledgements**

There are many friends, colleagues and family whom I would like to thank for their tremendous contributions to my life and work through the doctoral process. First, I would like to thank my advisor, Konstantin Sokolov both for his support and magnanimously taking me in as an orphaned graduate student. His assistance in formulating ideas and directions to approach problem solving have been invaluable. Secondly, I would like to thank my co-advisor, Peter Gascoyne, who never gave up on me and has continued to give me encouragement and joy to this day. I would like to thank all the members of the BOND lab, past and present while I've been working there, as well as those formerly of Dr. Gascoyne's lab. All of you have at one time or another provided me with valuable insight, laughter and the drive I needed to push through to the end. I would like to thank my parents and brothers, who always pushed me to succeed to the best of my abilities, and I would like to profusely thank my wonderful fiancée, who has held me together throughout the dissertation process.

# **Microfluidic PCR With Plasmonic Imaging for Rapid Multiplexed Characterization of DNA from Microbial Pathogens**

Jason Michael Haber, Ph.D.

The University of Texas at Austin, 2016

Co-Supervisor: Konstantin Sokolov

Co-Supervisor: Peter Gascoyne

Bloodstream infections (BSIs) are a critical concern in modern medicine due to their continued prevalence in modern hospitals, along with high costs and attributable mortality, particularly among those who are immunocompromised. The current gold standard for detection and characterization of causative pathogens involves cell culture, which can take 24-48 hours to complete, increasing time to adequate treatment and thus mortality. The rise of antimicrobial resistance in hospital acquired infections has reduced the effectiveness of broad spectrum antimicrobial treatments, resulting in a clear need for a rapid, sensitive technique for characterization of resistance markers in microbial pathogens without cell culture. Here we present the development of a microfluidic platform for polymerase chain reaction (PCR) mediated amplification of microbial gene targets in a continuous flow system for potential coupling with sample preparation systems to reduce time to diagnosis from days to within two hours. This culminated in a thermoelectric cooler mediated fluidic thermocycler with a recirculating assay region for real-time hybridization measurements to minimize assay time.

We subsequently demonstrated development of a low-cost optical system for localized surface plasmon resonance imaging using a digital micromirror device and tuned nanoprism monolayers for DNA hybridization with a spectral resolution of 2nm. This LSPR imaging system was integrated in-flow into the microfluidic thermocycler, enabling detection of input *E. coli* DNA samples at a minimum concentration of 5fg/ $\mu$ L. We further demonstrated multiplex detection of target markers, indicating potential for assaying target panels for characterization of pathogens. Overall, the studies in this dissertation demonstrate a microfluidic PCR system with built-in sensitive LSPR detection of DNA hybridization. It should serve as a starting point for exploration of and expansion with fluidic sample preparation with a focus on rapid characterization of pathogens.

## Table of Contents

List of Tables .....	xii
List of Figures .....	xiii
Chapter 1: Introduction .....	1
1.1 Medical Diagnostics and the Modern Age.....	1
1.2 Microfluidics and Point-of-Care .....	3
1.3 Nanotechnology and the Interface with Microfluidics .....	5
1.5 Outline of Specific Aims .....	7
Chapter 2: Background .....	10
2.1 Motivation: Bloodstream Infections .....	10
2.2 The Rise of Superbugs .....	12
2.3 Approaches to Resistance Characterization.....	13
2.4 Polymerase Chain Reaction .....	15
2.4.1 Principles of Operation .....	15
2.4.2 Thermocycling Methods .....	18
2.5 Micro-Total Analysis Systems.....	21
2.5.1 Principles and History.....	21
2.5.2 Fluidic Control Systems.....	24
2.6 DNA Detection Strategies.....	26
2.7 Noble Metal Plasmonics .....	27
2.7.1 Surface Plasmon Resonance .....	27
2.7.2 Localized Surface Plasmon Resonance .....	30
2.7.4 Optical Measurements of LSPR.....	31
2.7.3 Nanoparticle Synthesis: Shapes and Sizes.....	32
2.8 Relevant Literature Synopsis .....	34
Chapter 3: Development of Rapid, Recirculating Microfluidic PCR .....	36
3.1 Abstract .....	36
3.2 Introduction.....	37
3.3 Materials and Methods.....	39



3.3.1 Synthesis of Microfluidic Chips .....	39
3.3.2 Microelectrode Patterning.....	40
3.3.3 Thermocycling Control.....	40
3.3.4 Piezoelectric Pumping .....	41
3.3.5 Bacterial Culture .....	42
3.3.6 DNA Isolation Protocol .....	42
3.3.7 PCR Protocols.....	42
3.3.8 Agarose Gel Electrophoresis.....	43
3.4 Results.....	44
3.4.1 Disk/Cartridge Based PCR .....	44
3.4.2 Thermoelectric Thermocycling.....	46
3.4.3 Pumping and Flow Control Systems.....	55
3.4.4 PCR Verification.....	59
3.5 Discussion .....	61
3.6 Acknowledgements.....	62
Chapter 4: Digital Micromirror LSPR Imaging and Optimized Tunable Nanoprism Synthesis .....	64
4.1 Abstract .....	64
4.2 Introduction.....	65
4.3 Materials and Methods.....	68
4.3.1 Silver Nanoprism Synthesis.....	68
4.3.2 Characterization of Silver Nanoprisms .....	69
4.3.3 Nanoprism Stability Calculations .....	70
4.3.4 Nanoprism Adhesion to Glass Substrates .....	70
4.3.5 Silver Nanoprism Functionalization .....	71
4.3.6 Hyperspectral Imaging.....	71
4.3.7 LSPRi Optical Assembly.....	72
4.3.8 2D Spectroscopic Imaging Analysis.....	72
4.4 Results.....	73
4.4.1 Selection of Nanoprism Synthesis Regime.....	73

4.4.2 Optimization of Silver Nanoprism Synthesis .....	76
4.4.3 Functionalization and Adhesion of Nanoprisms.....	86
4.4.4 Development of Optical LSPR <sub>i</sub> System .....	89
4.4.5 Verification of Optical LSPR Imaging .....	93
4.5 Discussion.....	95
4.6 Acknowledgements.....	96
Chapter 5: Microfluidic PCR with On-Chip LSPR <sub>i</sub> for Rapid Characterization of Bacterial Genetic Markers .....	97
5.1 Abstract.....	97
5.2 Introduction.....	98
5.3 Materials and Methods.....	99
5.3.1 Nanoprism Synthesis .....	99
5.3.2 Nanoprism Adhesion to Glass Substrates.....	99
5.3.3 DNA Probe Bioconjugation.....	100
5.3.4 Fabrication of PCR Chip.....	100
5.3.5 Piezoelectric Pumping .....	101
5.3.6 Thermocycling Control.....	102
5.3.7 LSPR <sub>i</sub> Optical Assembly .....	102
5.3.8 LSPR Imaging Data Analysis .....	103
5.3.9 Hyperspectral Imaging.....	104
5.3.10 DNA Isolation Protocol .....	104
5.3.11 PCR Protocols.....	105
5.3.12 Experimental Setup.....	105
5.4 Results.....	106
5.4.1 DNA Probe Functionalization Kinetics .....	106
5.4.2 Verification of Combined LSPR/PCR Chip .....	107
5.4.3 Limit of Detection Analysis.....	111
5.4.4 On-Chip Multiplex PCR .....	113
5.5 Discussion.....	115
5.6 Acknowledgements.....	116

Chapter 6: Conclusions and Future Directions .....	117
6.1 Conclusions.....	117
6.2 Future Directions .....	119
6.2.1 Optical and Microfluidic Improvements.....	119
6.2.2 Sample Preparation Systems.....	120
6.2.3 Electrophoretic DNA Focusing.....	121
6.2.4 Parallel Assays .....	124
Appendix A Circuit Diagram of TEC Thermocycler .....	125
Appendix B PID Control Program for Arduino - AmpliTaq Gold PCR .....	126
References.....	130
Vita .....	151

## **List of Tables**

Table 1.1:	Selected Commercial Microfluidic Applications.....	4
Table 3.1:	Temperature Calibration for IR and RTD Sensing.....	49

## List of Figures

Figure 2.1: Schematic of Polymerase Chain Reaction Operation .....	16
Figure 2.2: Schematic of Surface Plasmon Resonance and Kretschmann Configuration .....	29
Figure 3.1: CAD Diagrams of Early Disk and Cartridge-Based PCR Thermocycler Designs.....	45
Figure 3.2: Materials Testing for PCR Inhibition .....	47
Figure 3.3: Thermocycling Temperature Control and Stability .....	50
Figure 3.4: Well-Based PCR Chip Design and Results .....	51
Figure 3.5: Continuous Flow PCR Chip Designs and Fabrication.....	52
Figure 3.6: Continuous Flow PCR Chip Results.....	54
Figure 3.7: Piezoelectric Pumping Principles and Test Chip .....	57
Figure 3.8: Piezoelectric Pumping Flow Rates: Voltage and Frequency .....	58
Figure 3.9: Continuous Flow PCR With In-Loop Pumping Results .....	60
Figure 4.1: Representative Extinction Spectra of Various Nanoprism Synthesis Regimes.....	74
Figure 4.2: Glass Adhesion Test for Nanoprism Synthesis Regimes.....	75
Figure 4.3: Nanoprism Instability Demonstration.....	75
Figure 4.4: Reaction Schematic of Optimized Nanoprism Synthesis .....	76
Figure 4.5: Effects of Ascorbic Acid Concentration and Seed Solution Aging on Nanoprism Spectra and Stability .....	78
Figure 4.6: Effects of Hydrogen Peroxide and Sodium Borohydride Concentration on Nanoprism Spectra and Stability .....	79
Figure 4.7: Effects of Seed Solution Dilution on Nanoprism Size.....	80

Figure 4.8: Absorbance Peak by Silver Nitrate Added for Varying Levels of Seed Dilution .....	81
Figure 4.9: Effects of Sodium Citrate Concentration on Nanoprism Spectra and Full-Width Half-Maximum .....	82
Figure 4.10: Effects of Silver Nitrate Addition Rate on Nanoprism Spectra and Stability .....	84
Figure 4.11: Representative TEM Images of Silver Nanoprisms.....	85
Figure 4.12: Demonstration of One-Pot Synthesis of Optimized Silver Nanoprisms .....	86
Figure 4.13: Comparative Spectra of Prisms Synthesized at Different Volumes .	86
Figure 4.14: Representative Extinction Spectra and Nanoprism Colors.....	87
Figure 4.15: Nanoprism Monolayer Stability Under Heating and Pumping.....	88
Figure 4.16: Proposed Optical Pathway for LSPR Imaging.....	89
Figure 4.17: Spectral Output of Halogen, Xenon and LED Sources.....	90
Figure 4.18: Nanoparticle Spectra Measured by Spatially Resolved Spectral Illumination.....	92
Figure 4.19: Diffraction Aperture Size Test With Bandpass Filters .....	93
Figure 4.20: Comparison of LSPRi and Hyperspectral: Nanoprism Monolayer with Various Solvents .....	94
Figure 5.1: Layout and Construction of LSPRi/Recirculating PCR Chip.....	101
Figure 5.2: DNA Probe Binding Optimization.....	107
Figure 5.3: Combined LSPR/PCR Chip Gel Electrophoresis Results .....	108
Figure 5.4: PCR Cycle Diagram for Typical Experiment .....	109
Figure 5.5: LSPR/PCR Results, Analysis Method 1 .....	110
Figure 5.6: Limit of Detection Series Results .....	112

Figure 5.7: Spectral Shift Over Time for 5fg/ $\mu$ L DNA Input .....	113
Figure 5.8: Demonstration of Multiplex PCR .....	115
Figure 6.1: Transverse Electrophoretic DNA Separation.....	122
Figure 6.2: Transverse Electrophoretic Separator Iterations and Results .....	123
Figure 6.3: Schematic of Isoelectric Focusing .....	124

## **CHAPTER 1:**

### **Introduction**

#### **1.1 MEDICAL DIAGNOSTICS AND THE MODERN AGE**

The field of medicine has seen something of a renaissance over the last century with the introductions of biochemistry, molecular biology and modern pathology. As recently as the 1920s, respected scientists and physicians ascribed to Galen's theory of the four humours, first originating in ancient Greece by Hippocrates and perpetuated through Roman medicine all the way up to the late 19<sup>th</sup> century when increased focus on microbiology and the physical underpinnings of disease finally began to put the theory to rest, largely as a result of the work of individuals such as Louis Pasteur[1] and Robert Koch[2], and aided by rapid development in microscopy technology led by Ernst Abbe and Carl Zeiss[3]. While support for such concepts had eroded over centuries of prior scientific advancement, this period of scrutiny and classification of pathogens and medical techniques, coupled with other factors such as the initial discovery of deoxyribonucleic acid (DNA) and the details of heredity, laid the groundwork for modern medicine.

Not to be outdone by the 19<sup>th</sup> century, the modern age has seen an explosion in medical technology, matching advances in science across the board. In medical imaging and diagnostics alone, numerous modalities have been proposed, developed and then improved again for application to increasingly varied problems. X-ray systems pioneered by Wilhelm Roentgen were adapted to tomography, then computed tomography (CT)[4], then variant analysis techniques such as dual energy. Magnetic Resonance Imaging (MRI),



initially developed as recently as 1971[5], has already expanded to a massive array of specialized systems and techniques, from fMRI to MR angiography. While these modalities, along with ultrasound, photoacoustic imaging and PET offer a wide range for macro-level and tissue measurements[6], and electron microscopy and NMR provide a wealth of information at the molecular level[7], in microbiology optical microscopy and imaging are still king, particularly in applications dealing with studies of microbial pathogens. Conventional light microscopy, fluorescence, confocal, super-resolution techniques (PALM, STORM, atomic force microscopy)[8], dark-field, hyperspectral and other spectroscopic methods all provide valuable information for a subset of applications. Faster cameras, digital interfaces, segmentation and other algorithms have all contributed to the potential for more complex imaging systems and diagnostics.

Optical imaging systems also have a strong cross-over potential with miniaturization, another modern trend in both consumer electronics and medical devices[9]. The dream of a small-scale diagnostic tool with a wide range of potential applications, much like the tricorder of Star Trek fame, has long been an attractive direction of research. The advent of molecular assays along with miniaturization of imaging technology and electrochemical detection techniques have brought this dream closer to fruition than ever before, but there is still a long way to go before it is possible to simply wave an instrument over a patient and instantly know anything that is wrong with them. To strive ever closer to this goal, assays and detection schemes must be designed and coupled with simple, rapid sensing in mind.

## 1.2 MICROFLUIDICS AND POINT-OF-CARE

Miniaturization of fabrication and molecular assay technology has led to the field of microfluidics, or systems designed to process samples in very small volumes, generally ranging from microliter down to picoliter scale[10]. Taking diagnostics down to such scales brings with it a number of highly attractive properties: high surface area to volume ratio is advantageous for a number of applications, such as sensing on arrays with improved detection efficiency[11]. Short cross-sectional distances allow for manipulation of samples with precise application of electric or magnetic forces, enabling Lab-on-a-chip applications designed to perform complicated tasks or assays on a single microchip. Of course, these advantages come with the drawback of very small sample volumes, which can make detection of low concentration analytes difficult and increases the challenges of scaling up throughput to match clinical samples in such cases[12].

Originally born out of MEMS (micro electromechanical systems) in the 1980s, such improvements in micromachining and patterning allowed for the fabrication of the level of small-scale chips necessary for microfluidics[13]. Since then, the field has spread to encompass a wide range of materials and disciplines, ranging from silicon-based MEMS to PDMS soft lithography[14] to paper-based assays that have been gaining ground in recent years[15]. The potential for highly sensitive bioassays using only a small sample has significant draw, and there have been several high profile successes related to microfluidics. Table 1.1 attempts to list some of the more notable microfluidic success stories, perhaps the most well-known of which are the blood glucose meter and the home pregnancy test.

**Table 1.1.** Selected commercial microfluidic applications.

System	Operating Principles	Year
Handheld Glucometer	Paper test strip, enzymatic assay	1981[16]
Home Pregnancy Test	Paper test strip, wicking + hCG sandwich immunoassay	1980s (1988 for monoclonal antibodies)[17]
IonTorrent (Roche)	Next-gen Sequencing, semi-conductor based pyrosequencing	2012[18]
LabChip (Perkin Elmer)	Capillary Gel Electrophoresis, Spectrophotometry	2000[19]
Ink-jet Printer Head	MEMS, Thermal Inkjet Printing	1985[20]

An important observation from such successes that is often overlooked, is that microfluidics has historically been at its most valuable when focused on point-of-care diagnostics. While complex lab-on-chip sensors can be of tremendous research value and demonstrate concepts that will certainly be useful in the years to come, many require careful external control and manipulation, with a dizzying array of parts and pumps to enable a complex assay on a microchip. In contrast to this vision of so-called ‘chip-in-a-lab’, microfluidics as a field is uniquely situated for point-of-care systems[21, 22], with simple to control assays that can quickly process clinical samples and provide feedback in a physician’s office, or at worst, hospital laboratory with minimal fuss, enabling early detection or rapid quantification of biomarkers[23].

In such a setting, the principle challenges are in developing low-cost robust fluidic assays with sensitive detection schemes and scaling up to systems capable of high throughput for analysis of clinical samples where necessary. Notably, applications such as simple molecular biomarker assays and blood tests[24], separation of molecules or even

cells[25], as in flow-assisted cell sorting and dielectric separation of circulating tumor cells (CTCs)[26], and identification of pathogens through antibiotic susceptibility testing[27], holography[28] or genetic characterization are ideal avenues of exploration for point-of-care focused microfluidic devices.

### **1.3 NANOTECHNOLOGY AND THE INTERFACE WITH MICROFLUIDICS**

Nanotechnology, broadly defined as the study and/or manipulation of matter with at least one dimension below 100 nanometers[29], has enormous and far reaching implications in medicine and diagnostics. While the term nanotechnology covers a vast array of technologies, applications in the biomedical field alone are staggering. Carbon nanotubes are being studied for targeted drug delivery[30], man-made metamaterials use nano-scale patterning to create bulk properties that flaunt established physics for advantageous attributes in applications such as hyperlenses for super-resolution imaging in both optical[31] (net negative refractive index) and ultrasound systems[32] (net negative density), nano-electronics allow for biosensing of minute electrochemical shifts during binding events[33, 34], and nanoparticles of all types have tremendous applications for both diagnostics – as the basis for highly sensitive assays or contrast agents for traditional imaging techniques[35] – and therapeutics – for thermal ablation of tumors[36] and drug delivery[37], among others.

Due to the similarity in scale, there is tremendous overlap between microfluidics and nanotechnology. Nano-fluidics and nano-electronics are the most obvious examples, the former is a mainstay of many classical microfluidic systems, and the latter allows for increasing levels of miniaturization in detection. Nanoparticles themselves also have

significant application in microfluidic devices, largely in terms of detection – plasmonic detection of noble metal nanoparticles has seen increasing use, as it can be label-free, highly sensitive, and couples well with flow cell design[38-40]. Paper-based microfluidics have also made extensive use of plasmonic nanoparticles, particularly the large shift in extinction peak observed when trapping gold nanoparticles in close proximity to each other in the presence of a target analyte[41] – an approach popular for some variants of the home pregnancy test[42]. In addition, magnetic nanoparticles, such as superparamagnetic iron oxide, have been used for magnetophoretic manipulation of sample flows and droplets to rapidly achieve complex mixing and washing steps for micro-assays[43, 44]. On the other side, microfluidic syntheses for a number of nanoparticle regimes have been demonstrated to improve monodispersity and reproducibility[45, 46], and more accurate characterization has been achieved through microfluidic monitoring of dynamic light scattering and zeta potential[47].

Of particular interest in this work are the applications of plasmonics and noble metal nanoparticles to biomarker sensing in microfluidic applications. Surface plasmon resonance (SPR)[48], localized surface plasmon resonance (LSPR)[49] and surface enhanced Raman scattering (SERS)[50] have all been successfully demonstrated for label-free sensing in microfluidic systems. In fact, the first commercial device incorporating SPR detection, from Biacore, fit squarely into this paradigm – utilizing a shallow flow cell with a thin gold layer coating the substrate for plasmonic sensing[51]. LSPR arrays have enormous potential as a sensing modality in microfluidics due to its applicability to a wide range of assay designs and potential targets. LSPR arrays formed from gold and silver

nanoparticles of a variety of shapes, as well as sputter coating mediated nanosphere lithography[52] and gold nanoholes[53] have been demonstrated for micro-assays.

#### **1.4 OUTLINE OF SPECIFIC AIMS**

The aims of this dissertation will guide development of a microfluidic system for the rapid characterization of microbial pathogens through real-time detection of PCR amplified genetic markers of antimicrobial resistances. The studies performed here will focus on the sequential design, prototyping, validation, and testing of the various components required for the functioning of such a device integrating microfluidic assays and nanoparticle-based detection techniques for exceptional sensitivity and multiplexing. Further, a prototype of a completed system will be verified and characterized for detection of amplified *Escherichia coli* DNA from bacterial lysate for both single target and multiplex analysis. To that end, the three aims of this dissertation are as follows:

- 1) First, we will construct and test the core microfluidic structure of the device. This includes developing a continuous flow Polymerase Chain Reaction (PCR) thermocycler and all attendant components with potential for addition of real-time detection of DNA amplicons. We will demonstrate a design paradigm culminating in a recirculating channel on a Peltier thermocycler for rapid continuous-flow PCR amplification. A recirculating channel will allow for more rapid detection of target markers than a traditional continuous flow system, as the amplicons will tend to accumulate in the looped channel and allow bulk PCR while maintaining fluidic flow rates. We will further demonstrate separate regulation of in-channel flow using pumping methods with no parts external to the channel, and characterize the resulting systems for optimal pumping

conditions to achieve desired flow profiles. These experiments will then lead to verification of a recirculating PCR thermocycling chip for amplification of target markers from E. coli DNA.

2) Secondly, we will develop and test an optical Localized Surface Plasmon Resonance Imaging (LSPRi) based detection scheme for use with a functional zone located inside the recirculating PCR channel. Silver nanoprisms have proven to be an ideal nanostructure for LSPR applications due to their high anisotropy and sharp edges[54], so silver nanoprism synthesis will be optimized for stability and functionalization for use in an LSPR array. An optical system will be constructed and verified in which white light is diffracted to separate out the visible spectrum and then directed onto a digital micromirror device (DMD), which will be used to isolate specific frequencies onto a fiber optic to pass them through the LSPRi detection zone and onto a CCD camera. The optical system will be characterized through imaging of nanoparticle monolayers under solvents with varying dielectric constants to demonstrate sensitivity.

3) Finally, we will finalize the device by combining the systems developed for aim 1 and aim 2 and then validate it using bacterial lysate. This will consist of integrating the LSPRi detection scheme into the microfluidic channel by immobilizing and functionalizing nanoprisms inside the recirculating PCR channel and wiring LED and camera control to function concurrently with fluidic power and control systems. . Real-time detection of target accumulation will be made by measuring the shift in the absorption of the hybridization region by integrating the difference between images at each wavelength and their corresponding reference images prior to analysis. The system will be verified for PCR

amplification and tested for limit of detection using a concentration series of input DNA from E. coli. Single target and multiplex PCR will be performed and matched to conventional PCR output to demonstrate functionality and potential for further development.



## **CHAPTER 2:**

### **Background**

#### **2.1 MOTIVATION: BLOODSTREAM INFECTIONS**

Bloodstream infections (BSIs, also called septicemia or bacteremia in the case of bacterial origins) are infections that have spread to the blood and are a critical concern in modern medicine[55]. BSIs can result from both bacterial and fungal infections, most notably those of the urinary tract, lungs, kidneys and abdomen[56, 57]. When left untreated, they can spread into the bloodstream, allowing for easy access of pathogens and toxins to other systems throughout the body, leading to significant risk of systemic infections that can be lethal[58]. Bloodstream infections presented at hospitals are grouped into three classifications: community acquired (unrelated to healthcare, presented with a BSI on admission), hospital acquired, and healthcare related (presented with BSI on admission, acquired through outpatient services)[59]. Approximately 2% of hospital admissions are related to cases of community acquired BSIs, most commonly related to respiratory tract infections[60].

In addition to patients who present with BSIs, hospital acquired, or nosocomial, BSIs remain a persistent problem even in the most advanced of clinics – most notably secondary infections related to main-line catheterization[61, 62]. In 2002 alone, an estimated 250,000 healthcare-associated infections occurred in the US, with over 30,000 estimated deaths[63]. While the causes and prognosis of BSIs in various forms has been well studied[64] and many procedural changes have been proposed/adopted to limit

them[61, 65, 66], BSIs continue to be a problem. Approximately 5% of all patients in the US get an infection during their hospitalizations[67], and the risks of such infections increase with duration of hospital stay, catheterization[68], low nurse-to-patient ratio[69] and a number of other factors[70]. The likelihood of nosocomial infection jumps dramatically for patients undergoing critical care, such as ICU patients[71, 72]. It also exceeds 15% among the immunocompromised[73], who are also at increased risk for polymicrobial infections[74] which carry an increased mortality[75], making BSIs a considerable risk for patients undergoing chemotherapy, a notable cause of neutropenia. In addition, hospital acquired and healthcare related BSIs are significantly more likely to be caused by drug resistant pathogens than community acquired ones, making treatment more difficult[57, 76].

Though generally treatable, these infections carry a high mortality rate, ranging from 16 - 40% in ICU patients[77, 78]. Time to adequate treatment has a significant impact on survival rate[79], but antibacterial resistance is linked to an increase in time to adequate treatment due to the likelihood that the initial round of antimicrobials is ineffective [80, 81]. To combat this, treatment of BSIs generally consists of broad-spectrum antimicrobials[82], however this can contribute to further antimicrobial resistances[83, 84], as well as increased cost. Rising rates of antibacterial resistance as well as increasing numbers of BSIs caused by fungi and gram positive bacteria have only worsened this effect[85, 86]. Even for those who survive BSIs, the length of hospital stay is prolonged by 4.5 - 32 days[77, 78, 87] and incur significant cost, up to \$39,000 per episode[78, 87, 88] leading to an estimated annual cost of \$60 – 460 million in the US alone[89]. As a

result, timely characterization of pathogens to facilitate effective intervention is critical to decreasing the burden of nosocomial infections.

## **2.2 THE RISE OF SUPERBUGS**

As discussed above, hospital acquired bloodstream infections are more likely to be caused by drug resistant pathogens, as well as gram positive bacteria or fungi that require different classes of antimicrobials and are thus generally increase time to adequate treatment[57, 76]. These are due to both the rising rates of antimicrobial resistance[90, 91], so-called superbugs, and hospital conditions that lead to more uncommon infections. Close proximity of patients[91], incomplete sanitization, and bodily fluids transferred from one room to another on lab wear can all contribute to bringing pathogens together[92, 93]. Bacteria often undergo conjugation, allowing plasmids containing genes that confer antimicrobial resistance to be passed between populations in a polymicrobial setting[94, 95]. In addition, incomplete treatment, due to improper dosage or duration[96], can result in surviving mutant populations with resistances that then spread through the hospital setting. While effective for reducing time to adequate treatment in BSIs with unknown pathogens, overtreatment with broad spectrum antimicrobials can also confer resistance through mutant populations[97, 98].

All of these factors contribute to the increasing rates of antimicrobial resistance, which is now considered by the CDC and medical community at large to be a global threat[99-102], resulting in at least two million drug resistant infections and upwards of 23,000 deaths in the United States alone[103, 104]. Notably, strains of some of the more common serious gram-negative pathogens, such as *Enterobacteriaceae* and *Acinetobacter*,

have developed resistances to virtually all known antimicrobials that would be used to treat them, becoming pan-resistant[105-107]. Rates of antifungal resistance have recently begun rising in common fungal infections, such as Candida[108, 109], indicating that they are not far behind on this trend.

The CDC has made a number of recommendations to stem the tide of antimicrobial resistances, most notably including more stringent preventative measure and sterilization, more controlled usage of antibiotics, and careful tracking of drug resistant strains and sharing of said data between hospitals.[103] While these recommendations will likely aid in reducing the rate at which drug resistance spreads, they can also make treatment of acute, unknown infections such as BSIs more difficult, as broad spectrum treatment without knowledge of efficacy or dosing would be inadvisable.

### **2.3 APPROACHES TO RESISTANCE CHARACTERIZATION**

As patient outcome in the case of bloodstream infection depends heavily on time to adequate treatment, there has been significant motion in recent years towards faster detection, however none have been able to supplant clinically standard procedures. The standard procedure for clinical lab work in the case of a suspected infection is to take an immediate blood sample for lab analysis[110]. Once in the lab, blood samples are treated with a blood lysis buffer, generally consisting of saponin, for aggregation and lysis of red blood cells, propylene glycol and sodium polyanetholesulfonate[111]. Following this, samples are often divided for different culture techniques, such as agar media culture and blood culture and then spread on the appropriate plate and left overnight[112]. Cell culture

can often take upwards of 24 hours[110], and is the limiting step in classical detection of microbial pathogens.

Following cell culture, resulting pathogens must be identified and characterized for resistances. One of the most common and direct techniques for detection of antimicrobial resistances, antimicrobial sensitivity testing (AST)[113, 114], probes the capability of commonly used antimicrobials to lyse bacteria to determine both resistance and the minimum inhibitory concentration (MIC), defined as the lowest concentration at which the pathogen does not grow. Common methods for AST include disk diffusion and microdilution testing. Disk Diffusion AST consists of a bacterial culture plate with a number of small disks carrying antimicrobial agents at known concentrations[115, 116]. Bacterial cells are smeared on the plate and allowed to grow. Antimicrobials they are susceptible to create a growth exclusion zone around the disk, the diameter of which correlates to susceptibility[117]. The downsides to this technique are that it is imprecise and very slow – matching cell culture times[113]. Microdilution testing is more precise, dilution series of an array of antimicrobial agents are loaded into a microwell plate[118]. Bacterial samples are loaded into each and observed for growth. This allows for precise margins on MIC determination, as well as testing for a wide range of antimicrobials. For these reasons, microdilution testing is currently the gold standard for antimicrobial susceptibility testing, but it is still slow – generally requiring overnight culture to complete[113].

Attempts have been made to speed up AST, forgoing or at the very least reducing the need for cell culture timeframes. In recent years, a number of alternative techniques

have been proposed, including MALDI-TOF[119], microfluidic AST[27], heated agarose inoculated with drugs for testing to trap and optically measure individual cell growth[120], fluorescent signal measurement[121], among others. While some of these techniques have resulted in highly sensitive, rapid detection, they still require large numbers of pathogen cells for functionality, preventing use directly from clinical samples.

Besides AST, and often run concurrently, is PCR (polymerase chain reaction) amplification of pathogen DNA targeting a panel of genes that can allow for the identification of species, and markers of antimicrobial resistances[122-124]. Since all biological activities depend on genetic code, markers exist and have been identified for a wide range of known bacterial drug resistances[125-127]. Multiplex PCR can be used to amplify a panel of such markers of resistance and/or pathogen species, and characterize the pathogens[128-130]. PCR is also highly sensitive, as will be discussed further below, creating strong potential for assays performed without prior cell culture. This technique does still have disadvantages – only known resistance markers can be assayed, and no dosing information is provided beyond prior experience with similarly characterized pathogens. It does still, however, provide an attractive, rapid, method for early characterization.

## **2.4 POLYMERASE CHAIN REACTION**

### **2.4.1 Principles of Operation**

Polymerase Chain Reaction (PCR) has become a cornerstone of modern molecular biology with a wide range of applications[131], from detecting bacterial resistance markers to crime labs[132, 133] to paternity tests[134, 135] to cloning for genomic sequencing[136,

137]. First developed in 1983 by Kary Mullis[138], PCR amplifies DNA by repetitively copying a target sequence to achieve a theoretical two-fold increase in copy number per cycle[139, 140]. With this geometric increase, a very small quantity of target DNA sequences can be amplified to copy numbers in the millions, limited only by starting concentrations of primers, free nucleotides and reaction kinetics[141].

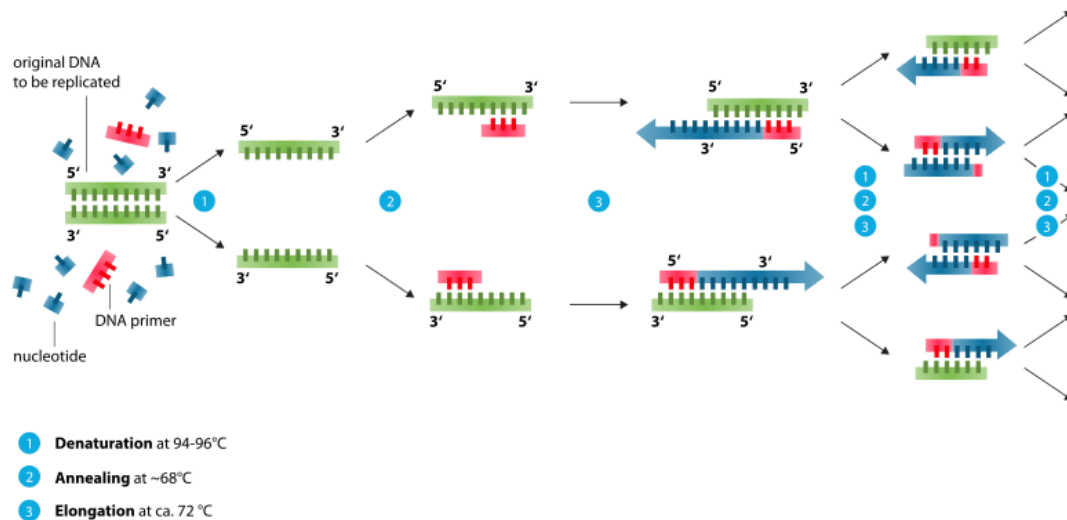


**Figure 2.1.** Schematic representation of polymerase chain reaction sequence of steps. In step 1, high heat denatures dsDNA molecules. In step 2, primers anneal to single stranded DNA at target sequences. In step 3, DNA polymerase incorporates free nucleotides to extend primers and complete dsDNA sequences. Image credited to the Wikimedia Foundation.

The technique relies on DNA Polymerase, an enzyme responsible for extending double-stranded DNA (dsDNA) from a starting primer bound to a template strand. Temperature cycling is utilized to achieve three sequential temperature steps.[138, 139] 1) Denaturation – at 94-96C, DNA denatures into complementary single stranded molecules (ssDNA). DNA denaturation temperatures (melting temperature,  $T_m$ ) vary significantly with the length of the sequence[142], GC content[143] and secondary structure[144], but 95C is sufficient for nearly all potential targets to melt. 2) Annealing – typically between

58-65C, the annealing temperature is defined by the melting temperatures of the primer sequences used[145, 146]. During this step, the temperature is held just below the  $T_m$  of the primers, allowing them to bind to the template DNA, the target sequences in the denatured DNA. Two primers are used per target gene, one for the 3' end, one for the 5', allowing for extension on both complementary halves of the denatured DNA. 3) Extension – typically at 72C, the ideal functional temperature for the Taq polymerase[147], the most commonly used polymerase in PCR. During this step, the polymerase enzyme binds to the primer/template complex and extends it using free floating nucleotides, creating two new dsDNA strands from the single strand present before the cycle. Other reaction components include free nucleotides (dNTPs), which are used to create new DNA strands, and magnesium ions ( $Mg^{2+}$ ), which are required for activation of DNA polymerase[148, 149].

PCR is a robust system, but there are a number of common failure modes. For most, precise temperature control is the key to prevention. Overheating during the denaturing step can lead to damage to the polymerase – even at standard denaturing temperatures, the Taq polymerase has a half-life of approximately 40 minutes[147, 150], and this decreases at higher temperatures. Cooling too far during the annealing step can lead to primer-dimer: at low temperatures the ordinarily unstable bond can form between the primers, leading to extension of small (~50bp) sequences[145, 151, 152]. Once this occurs, the primers can no longer be used to amplify target sequences. Notably, this effect can occur even in storage[153], which is why many modern polymerase enzymes have been modified to be so-called 'hot-start', meaning that they have been bound to an inhibitor, which is cleaved at ~90C, preventing primer-dimer extension in storage[154, 155]. Finally, some materials



can bind or damage DNA sequences[156], inhibit polymerase activity[157], or bind magnesium ions[158, 159], preventing polymerase activation (notably including EDTA, a metals chelator and common component in DNA storage media[160]). Some of these can be prevented using additives, common PCR adjuvants include bovine serum albumin[161, 162], which forms monolayers on material surfaces and improves biocompatibility, and TWEEN-20[163, 164], which neutralizes some detergents, such as sodium dodecyl sulfate (SDS), and prevents some protein interactions.

While PCR could theoretically turn even one copy of a target gene into a near infinite amount, there are both lower and upper bounds on its function. At the low end, a minimum number of copies the target are necessary for PCR to take place, though the precise number has been placed anywhere from 10-300 copies[165, 166]. This translates to theoretical minimum quantities of DNA from cellular sources – for a single allele target with only one copy per cell, 100 copies correlates to ~400pg for human cells (~4pg/cell) or 1.7pg for E. coli (~0.017pg/cell). At the upper end, very high initial DNA quantities can inhibit PCR – massive quantities of non-target DNA reduce access to the target sequences. This effect, combined with the half-life of polymerase and the limited quantity of dNTPs in a reaction lead to practical maximum amplification – the plateau region of the growth curve.

#### **2.4.2 Thermocycling Methods**

As precise temperature control during PCR steps is among the most important factors in ensuring successful amplification, conventional thermocycling systems are generally carefully engineered for thermal accuracy and stability over speed of cycling.

Over the years, commercially available thermocyclers have undergone a significant evolution, primarily focused on increasing cycling speed while maintaining precision – even slight decreases in the length of a cycle add up over the course of 40 cycles. The earliest thermocycling systems consist of heating blocks – large chunks of copper with holes drilled for vials or well plates[167]. The high thermal conductivity of copper (385 W/mK[168]) results in a homogenous temperature even with a heating source far removed from the sample wells, and relatively slow changes in temperature that can be precisely measured with a thermocouple[169]. Typically, these systems use one-directional thermal control – only heating is supplied, and cooling is achieved by allowing the block to radiate off excess heat. The next advance from these involved addition of a heated pad to sit on top of sample vials to reduce temperature gradients[170].

Modern PCR systems utilize a number of disparate approaches. The new common paradigm in commercial PCR utilizes air-heated systems[171, 172], in which samples are held in a small sealed air pocket which is heated while an internal fan keeps the air moving. While air has a much lower thermal conductivity (0.024W/mK), thermal homogeneity is maintained by the induced air flow, and the low density allows for fairly rapid heating. Cooling in these systems is much faster, as the seal is released to allow the air to mix with ambient until the temperature falls to the target point. This requires very careful automation, as the temperature falls rapidly, and failure to reseal the chamber can quickly lead to reduced temperatures and primer-dimer errors.

Smaller scale and microfluidic PCR systems often follow one of two designs: (1) reaction chambers, often fabricated from silicon, which are heated using an integrated

thermal sensor and a classic heating block design[173-175], and (2) temperature zones, in which a flow path repeatedly passes over a set of three zones set to PCR step temperatures[176, 177]. This creates slight temperature gradients at the boundaries between regions, but as long as flow rates are held evenly throughout the system, successful amplification can be achieved. The largest concern in microfluidic thermocycling is the formation of bubbles[178, 179] – microbubbles formed either from incomplete wetting at channel walls or a liquid sample that hasn't been degassed – expand rapidly under heating, wreaking havoc on carefully controlled flow rates and creating pressure spikes that can induce leaks and damage channels, and can also lead to nano-scale temperature gradients that interfere with precise thermocycling due to the aforementioned low thermal conductivity.

Regardless of thermocycling technique, precise control of temperature is critical to successful amplification, meaning that thermal sensing is a key part of any thermocycler. There are a number of precision thermal sensing systems – the most notable of which are thermocouples, thermistors, resistance thermal detectors (RTDs), material expansion sensors and infrared sensors. Classical analog thermometers use material expansion, historically of mercury, but more recently with colored water to avoid toxicity. While these can be made in digital forms, they have a slow response to change and are therefore uncommon in thermocyclers. Thermocouples are by far the most common thermal sensing element in modern use[180]: two different metals are joined, the difference in temperature gradient between the two results in electric current generation due to the Seebeck effect, or  $dV = -S(T)dT$ , where  $S(T)$  is a material dependent Seebeck constant. This same effect is

utilized in the opposite direction for Peltier-based thermoelectric heating elements. Thermocouples have a very wide range of operation, which has led to their use in commercial and industrial operations[181, 182].

First observed by Michael Faraday, thermistors[183, 184] and RTDs[185] have very similar methods of operation – both rely on temperature driven changes in resistance to measure. While RTDs are technically a sub-class of thermistors, RTDs are almost exclusively constructed from resistive metals such as platinum[186], while the term thermistor is generally used to refer to semiconductor or metal-oxide film based sensors. Both have improved reproducibility and reduced drift compared to thermocouples, but have a smaller operating range – generally up to a maximum of ~600F[187]. While thermistors are more tunable to specific application, the usage of resistive metals in RTDs allows for a linear dependence on temperature, while most thermistors are exponential.

## **2.5 MICRO-TOTAL ANALYSIS SYSTEMS**

### **2.5.1 Principles and History**

Following the first development of microfluidic systems, commonly attributed to the gas chromatograph by Terry, et al,[188] as the first miniature analysis system on silicon, it actually took years before the field hit its stride and expanded into biosensing, during which time research focus was primarily on fluidic control systems. In 1990, the term micro-total-analysis system ( $\mu$ TAS) was coined by Manz, et al,[189] though at the time it was ‘miniaturized total chemical analysis systems’, as biosensing had not yet become a mainstay. Micro-total analysis systems ( $\mu$ TAS) refers to a branch of microfluidics, also referred to as lab-on-a-chip, focused on systems capable of taking input samples and

performing assays and detection on the same device[190, 191]. Typically,  $\mu$ TAS design consists of some sample processing system as well as sensors and assay control for the specific application and a built-in detection regime to analyze output[13, 192, 193]. While such sensors are not limited to medical devices, and indeed did not begin there, the ultimate goal for any clinically relevant  $\mu$ TAS system is to be able to take a raw clinical sample as input and achieve sensitive and specific output data on target analytes or biomarkers[194].

Since their introduction,  $\mu$ TAS systems have seen a boom in applications in recent years, particularly in the late 1990s, as miniaturization techniques improved, leading to new control and fabrication paradigms, including the introduction of SU-8 photoresist mediated patterning[195, 196]. Micro-total analysis systems have been demonstrated for a stunning array of applications, from the initial  $\mu$ TAS for chromatography to biomarker analysis[197-199], to separations systems[44, 200, 201] and specific assays for applications such as antimicrobial susceptibility testing[27]. Detection schemes and assay design similarly run the gamut, though there are a number of commonalities throughout the field. Biocompatible materials such as polymethylmethacrylate (PMMA)[202, 203], polydimethylsiloxane (PDMS)[204, 205], polyetheretherketone (PEEK)[206, 207], silicon and glass are commonly used[208], as are photopolymers for precise formation of fluidic channel structures using photolithography[209], though there have been many successful systems based on other substrates, most notably paper, which has demonstrated popularity due to its significant potential for point-of-care assays[15, 210, 211]. Photolithography is also commonly used in conjunction with sputter coating to create patterned microelectrodes for both sensing and fluid flow systems[212]. Surface passivation systems, such as the

creation monolayers of biocompatible proteins such as bovine serum albumin (BSA) are commonplace in biosensing applications[213].

Advances in clean room techniques, including plasma-bonding for PDMS-glass interfaces[214], microcontact printing for simple patterning of minute features and molecular layers[215], and three-dimensional construction of microchips[216, 217] have all led to improvements in miniaturization and potential for biosensing. The advent of nanotechnology, rising from the same miniaturization trends that spawned microfluidics, has proved to have a strong cross-over with  $\mu$ TAS, providing further improvements in sensitivity and new potential assays for development.

While microfluidics and  $\mu$ TAS have grown exponentially in popularity and complexity, this has come at a price: ever increasing complexity of fabrication and structural design increases both the cost of construction and the likelihood of device failure. Highly complex microchips can also prove difficult to clean, preventing re-usability. This combined with limited reliability leads to limited application for point-of-care diagnostics. Miniaturization can also be taken too far, leading to low throughput and the infamous problem of ‘scaling up’ a microfluidic system[218]. As a result of these issues,  $\mu$ TAS systems have gained a reputation as ‘chip-in-a-lab’, envisaging a small microchip that can perform amazing feats – so long as it is hovered over by a team of watchful scientists. In order to take  $\mu$ TAS out of the research lab and into clinical usage, it is necessary to design systems to accommodate clinical samples from the start, not as an afterthought.

## 2.5.2 Fluidic Control Systems

Given the titular nature of ‘fluidics’ in microfluidics, control systems for fluid manipulation and flows are understandably a vital part of the field. One of the most central tenets of microfluidics is control of flow profiles – laminar and turbulent flow. While turbulent flow refers to the chaotic mixing and whorls often seen in fluid flows, laminar flow occurs when fluid forms parallel streams that characteristically do not mix. The crossover between the two forms of fluid flow were first demonstrated by Reynolds in 1883[219] where he showed that turbulent and laminar flow could be visualized using dye in a pipe under different circumstances, and that over a length, turbulent flow actually became laminar. He further postulated the Reynolds number,  $Re = \frac{\rho V D_H}{\mu}$ , where  $\rho$  is the density of fluid,  $\mu$  is the dynamic viscosity,  $V$  is the maximum velocity, and  $D_H$  is the hydraulic diameter of the channel,  $D_H = \frac{4A}{P}$ , where  $A$  is the cross-sectional area and  $P$  is the wetted perimeter. At low Reynolds numbers ( $<10^3$ , occurring when the channel has a large surface area-to-volume ratio, as in most microfluidics), laminar flow occurs, whereas turbulent flow occurs at higher Reynolds numbers[220]. As laminar flow is highly advantageous for a number of microfluidic applications[11, 221, 222], notably separations[223], maintaining a low Reynolds number is important.

Flow throughout microfluidic systems, especially continuous flow, is often maintained through external means. Fluid flow in microfluidics is generally seen as analogous to electrical current[224] – pressure is analogous to voltage, flow rate to current, and flow resistivity to resistance. Syringe pumps are heavily used to generate a constant

volumetric flow rate[12, 225], although these can result in large pressure spikes in highly resistive systems, leading to leakage and other problems. Alternatively, consistent pressure gradients can be applied either through pressure on a reservoir maintained through careful pressure sensing[224, 226], or by creating large height differentials between sample reservoirs to generate potential energy in the system[227]. In both of these cases, careful calibration and measurement of the resistance of fluidic structures to flow, usually measured in liquid ohms – or the linear ratio of pressure to flow rate, to extend the aforementioned analogy.

To achieve complex sample analysis schemes, internal control of fluidic structures is also necessary – valves, internal pumping, micromixers and the like[203, 228]. Pneumatic microvalves are a mainstay of PDMS based devices[229]: flow channels crossing over very thin boundaries with sample channels are used to obstruct those flows when the valve is closed, pneumatic flow is lessened to remove the obstruction when open. For internal pumping, a number of strategies have seen use. Electroosmotic pumping is among the most popular[224, 230], relying on the use of a microelectrode to create a voltage differential in the Debye layer across a permeable channel to create net flow. Electrokinetic[231] and electrothermal[232] systems use similar properties, though all three result in very low flow rates ( $<5\mu\text{L}/\text{m}$ ). For faster flow profiles, peristaltic pumping can be used in soft materials such as PDMS – a series of three pressure points are applied in series lengthwise in a channel to force flow[233]. Acoustic wave pumping using piezoelectric actuators has also been demonstrated[234], along with valveless piezoelectric



pumping, in which a buzzer is actuated between a pair of flow rectifiers to create net flow in one direction[235, 236].

## **2.6 DNA DETECTION STRATEGIES**

In order to identify DNA sequences, notably after PCR amplification, it is necessary to detect them in some way, and, if possible, quantify. The most classic regime for DNA detection is fluorescence – fluorescent dyes that intercalate into DNA sequences and increase their signal, such as SybrGreen, EvaGreen and ethidium bromide can be used to detect the presence of DNA, and to a limited extent quantify based on signal strength[237-239]. This is the basis of most real-time PCR (qPCR) systems, as it is a rapid and robust detection technique. The disadvantage of using such dyes is that they are non-specific – any DNA will bind and boost signal, preventing multiplex applications in real-time. Gel electrophoresis can separate DNA into bands by size[240], allowing for fluorescent imaging of multiple targets, but this cannot be done in a real-time analysis. Other systems have been proposed for non-targeted DNA measurements, but have not achieved saturation.

For multiplex, real-time applications, a further step is needed. DNA hybridization probes are short sequences of single stranded DNA, generally 20-25 base pairs in length, that bind with high affinity to a matching target sequence[241, 242]. This allows a target sequence to be detected. DNA probes are often bound to a fluorophore and a quencher in a hairpin configuration that keeps the fluorophore and quencher in close proximity[243] – on binding to target DNA, they are separated, allowing the fluorophore to emit light. While

this allows for specific targeting and multiplexing, it is limited by the number of distinct fluorophores that can be measured – generally only a few at a time using switching filters.

For massively multiplexed applications, the DNA hybridization array is ideal[244, 245]. Probe sequences are immobilized on a substrate surfaces, often through avidin-biotin binding[246]. While this allows for spatial resolution of fluorescent signals for a large number of target sequences, the necessity for binding to a substrate eliminates the possibility for the hairpin configuration, meaning that separate labeling probes are needed to bind to DNA-probe complexes on the hybridization array to achieve fluorescent signal[247], thus complicating the process and requiring additional wash steps – one to remove non-adsorbed DNA samples, and a second to introduces the fluorescent probes.

A number of approaches have been developed in recent years for label-free hybridization – meaning that no separate ‘labeling’ marker is required for detection beyond previously immobilized probes. Barbaro, et al, demonstrated hybridization on a metal-oxide-semiconductor field-effect transistor (MOS-FET) to detect electrical signal from binding events[248]. Perhaps of most interest due to potential application to a wide range of other assays, label-free plasmonic imaging of DNA hybridization has also been demonstrated for both surface plasmon resonance[249] and localized surface plasmon resonance systems[250].

## **2.7 NOBLE METAL PLASMONICS**

### **2.7.1 Surface Plasmon Resonance**

A peculiar effect arising in metal thin films is the surface plasmon: a charge density wave at the interface between a metal thin film and a medium with a positive dielectric

constant. P-polarized light reflected off of such an interface can, under certain circumstances, couple into these surface plasmons, reducing the energy of the reflected beam[48]. This effect only occurs under precise conditions, however. The metal film must have a negative dielectric constant, arising from a low refractive index and high extinction coefficient, which are only found in ‘noble’ metals – gold, silver and copper[251]. Even with such a thin film, the layer must be sandwiched between two dielectric media. Under these conditions, energy from light totally internally reflected of the surface will instead be partially transferred into surface plasmons, called plasmon coupling. This effect reaches a sharp peak at some angle past the critical angle for internal reflection, known as the surface plasmon resonant angle. This reflection angle depends on the wavelength of the light used, the thickness of the thin film, and the dielectric constants of the surrounding materials within reach of the evanescent field (~200nm)[252].

As the resonant angle depends on the local dielectric constant, it is possible to monitor changes such as those arising from increasing mass on the thin film surface[253]. Building from these basic principles, surface plasmon resonance was first utilized to interrogate monolayers on a substrate by Pockrand, et al in 1978[254], and subsequently for the first biosensing application by Liedberg, et al in 1983[255]. SPR biosensing utilizes total internal reflection off a noble metal thin film surface, typically ~5nm of gold, modulated to the resonant angle. Once tuned to the resonant angle, either angle or wavelength can be modulated to characterize plasmonic spectra[256]. The most common optical scheme for SPR was developed in 1971 by Kretschman, et al[257], utilizing a prism with a high refractive index to bend an incident light beam to an appropriate angle for total

internal reflection (Fig. 2.2). The light source can then be placed on a precise angular platform to allow for modulation of the reflection angle. This configuration has been reported to reach nanomolar detection for DNA hybridization applications[258], and the high level of sensitivity has led to the use of SPR in a wide array of sensing applications, including ELISA[259], allergen testing[260], and many others.

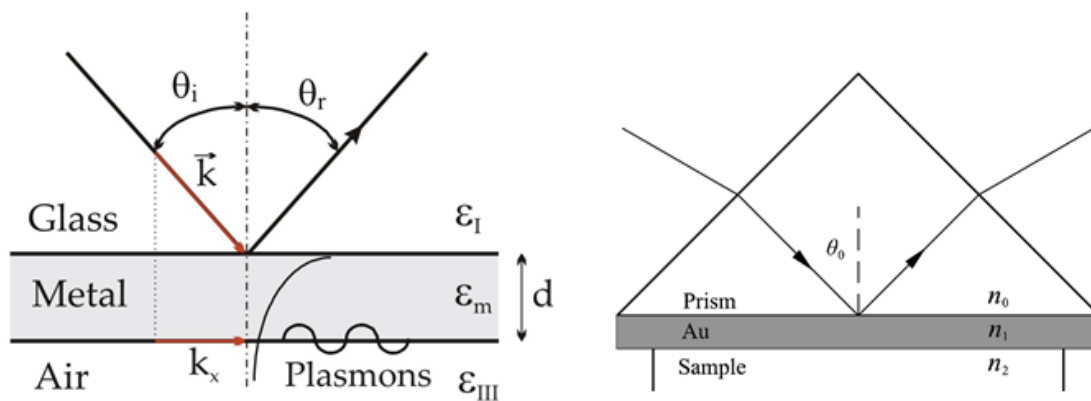


**Figure 2.2.** Schematic representation of surface plasmon resonance (left). At or near the resonant angle,  $\theta_r$ , energy from the reflected beam is transferred into surface plasmons along the boundary between the second dielectric and the metal film. (Right) Diagram of the Kretschmann configuration, in which a high refractive index prism is used to achieve bending of light for creating total internal reflection at angles sufficient for SPR to occur. Images credited to University of Liege HoloLab.

Since then, many novel variants on SPR have been reported to achieve improvements on the sensitivity. For example, Homola, et al, reported SPR using elliptically polarized light[261], fluorescent spectroscopy coupled with SPR has seen attomolar detection[262], and SPR arrays have been built into optical fibers[263]. In addition to these variants, 2-dimensional SPR imaging has been utilized for visualizing arrays[264], allowing for multiplexed analysis, and some live cell imaging[265], though

this technique is less sensitive than its cousins, as it measures simple change in reflected beam signal rather than utilize spectroscopic data for higher sensitivity.

### 2.7.2 Localized Surface Plasmon Resonance

Extending from Surface Plasmon Resonance biosensors, it was discovered that noble metal nanoparticles carried characteristic extinction peaks in the visible light spectrum due to a similar effect, and, much like plasmon coupling, the extinction peak depended in part on the local dielectric constant around the nanoparticle[49, 266]. This effect was termed localized surface plasmon resonance (LSPR). The precise location of this extinction peak is defined by Mie theory and Maxwell's equations, resulting in the equation for the extinction spectrum of a metal sphere:

$$E(\lambda) = \frac{24\pi^2 N a^3 \varepsilon_{out}^{3/2}}{\lambda \ln(10)} \left[ \frac{\varepsilon_i(\lambda)}{(\varepsilon_r(\lambda) + \chi \varepsilon_{out})^2 + \varepsilon_i(\lambda)^2} \right]$$

Where  $\varepsilon_r$  and  $\varepsilon_i$  are real and imaginary portions of the metal dielectric constant,  $\varepsilon_{out}$  is the external dielectric constant,  $a$  is the size of the particle, and  $\chi$  is a multiplicative factor that increases with aspect ratio.[266] This created the potential for biosensors based on direct transmission of light, eliminating the need for complex prism configurations for total internal reflection. Additionally, LSPR resulted in improved sensitivity over standard SPR, boasting picomolar detection.[267, 268] Mie theory also predicts significant red-shift in the extinction peak with close proximity between nanoparticles[269], which has led to further improvements on detection limit.

In addition to LSPR biosensors, the same phenomenon led to the development of Surface Enhanced Raman Scattering[270], which is believed to utilize excitation of

localized surface plasmons in nanoparticle surfaces to enhance Raman spectroscopy signal significantly. Both LSPR and SERS are commonly performed with carefully shaped nanoparticles such as rods or prisms, as such sharp edges lead to high anisotropy in the particles, and a large electromagnetic enhancement that increases shifts in the extinction peak[271].

While colloidal LSPR has been demonstrated, most research in the field is focused on surface-bound nanoparticle arrays[272]. Nanosphere lithography is commonly used to create a monodisperse array of precise prism shapes[273] and substrate silanization can be used to adhere particles through other reactions[274], both resulting in regular arrays of nanoparticles for LSPR or SERS. Recently, nanohole arrays have become an increasing mainstay of LSPR applications, generally fabricated by electron beam treatment of a gold thin-film surface[275]. These have significantly improved optical properties and layer uniformity by design, at the cost of expensive instrumentation and highly challenging synthesis.

### **2.7.3 Optical Measurements of LSPR**

Since LSPR results in a shift in the extinction peak of nanoparticles under changes in the local dielectric constant rather than an angular shift such as that in SPR, direct measurements are possible. As a result, spectroscopy is the most common technique used for analyzing LSPR shift.[276] In addition to UV-Vis spectroscopy, Rayleigh scattering and Raman scattering spectroscopy both see use, the latter notably in SERS. Imaging applications have been demonstrated using 2D spectrophotometers in conjunction with microscope objectives to reduce background[271]. Darkfield microscopy, in which a

patch-stop ring is used in conjunction with a condenser to obtain phase-shift information, is also a mainstay in imaging of plasmonic particles[277], particularly in live cell applications[278]. Spectroscopy in some form is key to any LSPR application, as extinction shifts are small and difficult to spot with simple colorimetric sensors. Spectral measurements allow for significantly improved sensitivity without resorting to particle labeling. Hyperspectral measurements are strongly applicable to plasmonics, though this imaging technique is slow and provides limited spatial resolution[279].

In most cases, LSPR is measured for particles immobilized on a substrate surface, generally functionalized with some probe in biosensor applications. Colloidal LSPR detection has also been demonstrated, but it is far less common[280]. Additionally, ultra-high sensitivity LSPR has been demonstrated using a hybrid technique in which immobilized particles form complexes with colloidal particles with probes specific to the same target molecule. While this makes the sensor no longer label-free, nanoparticles in close proximity significantly red-shift their optical extinction spectra, leading to the possibility of colorimetric detection[281].

#### **2.7.4 Nanoparticle Synthesis: Shapes and Sizes**

As the field of nanotechnology has grown and gained increasing recognition and funding, the number of nanoparticle syntheses have been rising commensurately. Nanoparticles are now a mainstay of modern medicine, with applications in imaging and diagnostics, and treatment, including radiation therapy. Nanoparticles now come in an array of materials, including silver[282], gold[283], iron and iron oxide[284], polymers[285], silica[286] and many more. An astounding number of shapes have also

been demonstrated across the field – spheres[287], prisms[288], cubes[289], wires[290], rods[291], bipyramids[292], clusters[293], hybrid particles[294], and even specialized shapes.

While nanoparticles of various types have a wide range of applications, LSPR and SERS require noble metal nanoparticles – gold and silver – due to their unique dielectric properties, as discussed previously. In addition, electromagnetic enhancement resulting from sharp edges makes shapes such as prisms, plates, cubes, wires and rods ideal for such applications. As a result, significant effort has been expended in discovery of novel shapes and synthesis techniques for noble metal nanoparticles. While nanocubes and nanowires generally require precise reaction conditions in solvothermal reactions[289, 290, 295], nanoprisms and nanorods have been demonstrated in simpler synthesis regimes. Gold nanorods can be formed using reduction reactions by controlling the ratios of surfactant, generally cetrymethyltriammonium bromide (CTAB)[291, 296].

Silver nanoprisms were first demonstrated by Jin, et al in 2001[288]. Starting from small silver nanospheres reduced from silver nitrate using sodium borohydride and sodium citrate, prisms were grown through photoinduction using light with peaks that stimulated the dipole and quadrupole moment of the desired prism size in the presence of a sequestering agent, bis(p-sulfonatophenyl)phenylphosphine (BSPP). They later expanded on this technique to allow for tuning of plasmonic peaks using laser light to excite the dipole moment[297].

Following the initial demonstration of silver nanoprisms, many other approaches have been demonstrated – solvothermal approaches[298], seeded growth[299] and



peroxide etchants[300]. Nearly all such nanoprism synthesis techniques utilize a similar basic methodology – silver nanospheres are formed via sodium borohydride reduction, followed by growth of prisms in the presence of a surface stabilization agent – often polyvinylpyrrolidone (PVP), sodium citrate, or other starch. This surface stabilization agent preferentially binds to the <100> facets of the nanoparticles, impeding addition of silver ions and creating directional growth on the <111> facets to form prism or bipyramidal shapes[301]. While surface stabilization is uniformly required to create the characteristic shape of nanoprisms, the actual technique for growth varies. Protocols have been reported utilizing a weaker secondary reducing agent, hydrogen peroxide as an etchant, or heat treatment to catalyze growth.

## **2.8 RELEVANT LITERATURE SYNOPSIS**

As discussed previously, the nature of often low pathogen concentrations present in bloodstream infections makes diagnosis directly from a clinical sample without cell culture difficult to accomplish - as reported by Seifert et al, many infections have bacterial concentrations below 15 CFU/mL[302]. As a result, rapid characterization of pathogens must be capable of detecting such low concentrations. As an amplification technique, polymerase chain reaction is an ideal pre-detection step, as it allows such small concentrations to be increased to detectable levels[166] and is already proven for resistance marker characterization in a wide range of pathogens[127, 303-305], meaning that the needed probe designs for detection are already extant.

Microfluidics provides significant advantage for PCR thermocycling, notably including more rapid temperature control, often below one minute per cycle[174, 306].

While microfluidics and PCR have a long history together[307-310], very little focus has been put into non-fluorescent real-time multiplex amplification, which would have tremendous value for diagnosis of bloodstream infections.

While microfluidics and PCR have long been tied together, the same is true of plasmonic detection and DNA hybridization. The label-free nature and high sensitivity of localized surface plasmon resonance simplifies DNA hybridization pathways[49], and easy binding of DNA probes to noble metal nanoparticles through thiol-binding[311] has made DNA detection an attractive research option for the study of LSPR, using both surface hybridization[268, 312] and colloidal aggregation, first reported by Alivisatos et al as a hybrid nanoparticle synthesis technique[313, 314]. Despite such intense interest in the field as a whole, as reported by Sepulveda et al, there has been very little attention to multiplex detection outside of highly complex surface patterns such as nanorings[267]. Similarly, there has been surprisingly little usage of digital micromirror devices as an inexpensive alternative to spectroscopy in LSPR detection outside of waveguides[315, 316]. Clearly there is potential for expansion into low-cost, multiplex LSPR imaging coupled with PCR amplification, with an application waiting in pathogen characterization from bloodstream infections.

## **CHAPTER 3:**

### **Development of Rapid, Recirculating Microfluidic PCR**

#### **3.1 ABSTRACT**

Microfluidic systems, and micro-total analysis systems in particular, have become a mainstay of biosensing in recent years. Due to the potential for rapid assays, sensitive detection, and manipulation of fluid streams for accomplishing sample preparation, assay and detection tasks in series on a single device, microfluidics is ideal for applications such as detecting DNA markers correlating to antimicrobial resistance from low concentration pathogen samples. Polymerase Chain Reaction (PCR) is capable of robust, specific amplification of target genes from bulk DNA, even at very low quantities, leading to the possibility of detection from low pathogen concentrations. While microfluidic PCR has previously been demonstrated, the use of a recirculating thermocycling region with in-built detection zone has not. Such a system carries the advantage of true real-time detection to reduce assay time, in addition to having potential for multiplexing and amplification of very low concentrations due to bulk thermocycling.

In this chapter, we demonstrate the development of a microfluidic thermocycler utilizing thermoelectric heating with resistance temperature detector-mediated control for rapid cycling and precise control. We demonstrate between-step thermal cycling times below 10 seconds and a temperature precision within 0.5°C. Further, in-flow piezoelectric pumping is demonstrated to achieve potential flow rates of over 150 $\mu$ L/m in a recirculating channel. These elements are combined to demonstrate successful amplification of DNA with the potential for expansion using DNA hybridization array-based detection for multiplex analysis.

### 3.2 INTRODUCTION

Due to the high cost and significant mortality incurred by hospital-acquired bloodstream infections[77, 78, 87], broad spectrum antibiotic treatments prior to receiving results from cell culture have become a standard treatment to presentation with BSI related symptoms, particularly in the immunocompromised[82]. While such treatment generally reduces the time to effective relief and thus mortality rate, it carries its own risks such as contributing to the increase in antibacterial resistance rates[83] – a critical concern in modern medicine. As a result, there is considerable interest in the development of techniques for faster characterization of pathogens while maintaining the sensitivity and precision of cell culture-dependent methods.

One avenue for rapid analysis that has gained significant traction in recent years is microfluidics – small volume assays carry potential for a number of valuable advantages, including nano-scale physics for highly sensitive detection systems, ability for rapid and automated mixing and manipulation of small volumes, and integration of disparate systems without need for robotics[13, 190]. These advantages have led to the rise of so-called micro-total analysis systems ( $\mu$ TAS)[189], which aim to perform robust molecular assays directly from clinical samples, in both research applications and commercial systems for a wide range of target applications. Such  $\mu$ TAS systems are ideal for cases where low analysis time is necessary for a complex input sample, such as blood samples from suspected BSIs.

While microfluidics carries these myriad strengths that can be applied to detection systems such as bacterial characterization, it also has a number of intrinsic downsides and design challenges to overcome. Microfluidics are often limited by small sample volumes, which reduces both throughput and the limit of detection[218] – while such assays are often highly sensitive, a low enough initial concentration of target analytes can result in none at

all being present in a tiny sample volume. Together, these effects lead to significant challenges in ‘scaling up’ a fluidic device to successfully process clinical samples. In addition, all microfluidic designs require careful consideration of flow profiles, surface wetting, microbubbles, materials selection and assay design.

There are a number of potential avenues that have been explored for identification and characterization of bacterial samples, including genetic methods, holography[28], protein analysis[317], cytometry[318] and antimicrobial susceptibility testing[113]. While holography and cytometry have proven well-suited to microfluidic design, they are limited in the quantity of achievable information – species and a couple of molecular targets can be interrogated, but there is not enough potential for the level of detailed analysis needed for characterization of resistances to antibacterial drugs. Antimicrobial susceptibility testing is robust, but it is difficult to perform on small samples due to the limited quantity of pathogens present in blood specimens. Genetic analysis using polymerase chain reaction (PCR) to amplify target genes for subsequent measurement is a proven gold standard method that is regularly used following cell culture[128] and is also an attractive system for microfluidic  $\mu$ TAS design due to its relative simplicity and power.

Fundamentally, PCR involves cycling through a series of precisely controlled temperatures that are designed to denature DNA, followed by annealing target sequences to short primer chains, and then extending those primers with a DNA polymerase enzyme. PCR is highly robust and sensitive, capable of amplifying samples down to very low quantities of a target gene[166], as well as being extendable to multiplex amplification[129]. Because it is non-destructive, it can be used in conjunction with any DNA detection method. A number of microfluidic PCR temperature cycling schemes have been demonstrated, generally utilizing either sample flow over a spatially-distributed series of temperature-controlled zones[176], or else holding the sample still in wells that are

subjected to local thermocycling[173], through either air- or substrate-based control. Detection methods are most commonly fluorescent qPCR or post-analysis fluorescent hybridization arrays, though other techniques have been demonstrated. The downside of these systems is that they either allow for real-time PCR, or a flow-through design that allows for higher throughput and analysis of clinical samples, but not both. For true rapid characterization of clinical scale pathogenic samples, both continuous flow and real-time detection are necessary.

This chapter enumerates the development of a microfluidic thermocycler for continuous flow PCR amplification with potential for multiplexed real-time analysis. Beginning from air-based thermal zone designs, the design path evolved towards a continuous-flow, looped thermocycling system with potential for in-loop DNA hybridization-based multiplex detection for real-time measurements of PCR. In addition, this chapter demonstrates the development and characterization of an acoustic pumping regime for separated in-channel flow management of the looped thermocycling region. Finally, the chapter provides verification of successful PCR amplification using fluorescent detection of target DNA sequences.

### **3.3 MATERIALS AND METHODS**

#### **3.3.1 Synthesis of Microfluidic Chips**

The microfluidic chips used in this chapter were synthesized through a number of fabrication approaches. Most commonly, chips were fabricated using channel structures cut using a VL-200 CO<sub>2</sub> laser (Universal Laser Systems, Scottsdale, AZ) from layers of dry-film adhesive (3M) (commonly called “transfer tape”), of 50 or 100 $\mu$ m thickness bonded to polymethylmethacrylate (PMMA) or glass substrates. PMMA substrates were

cut to desired shapes and inlets/outlets using the same VL-200 laser. For channel structures with taller form profiles, shim materials of desired thicknesses, ranging from 50-400 $\mu\text{m}$ , (Artus, Englewood, NJ) were cut using a VL-200 laser and then bonded between layers of dry-film adhesive. PCR chips were constructed with a bottom layer of 36-gauge aluminium to maximize thermal conductivity.

### **3.3.2 Microelectrode Patterning**

Microelectrodes were prepared using a photolithographic process. First, a negative mask of the desired microelectrode pattern was cut into a 5nm layer of chromium flash plater with  $\sim 0.2\text{nm}$  gold on a glass substrate using a Promaster Atlex SI exciplex laser (ATL Lasertechnik, Carlsbad, CA). A second gold blank was spin-coated in darkness with negative photoresist and then illuminated through the cut mask for 30 seconds with collimated UV light. The second blank was then immersed in aqua regia (80%v/v hydrochloric acid 30%, 20%v/v nitric acid 70%) for approximately 2 min, until the soft, unexposed photoresist and the gold layer beneath it were etched away. Finally it was immersed in concentrated sulfuric acid at 80°C until the underlying chromium layer and all remaining photoresist had dissolved away. The resultant patterned electrode on the second blank was then washed repeatedly with deionized water to remove any remaining acid.

### **3.3.3 Thermocycling Control**

Heating for thermocycling was provided using a VT-127-1.0-1.3-7.1 30mmx30mm Peltier device (TE Technology, Traverse City, MI). Power was supplied using a 24V, 4A power

supply (BioTec NG 60-5). Temperature control was managed using a resistance thermal detector (RTD, 615-1123-ND 1k $\Omega$ , DigiKey, Thief River Falls, MN) connected to an Arduino Uno microcontroller running a custom PID control program. The circuit diagram and PCR thermocycling control code may be found in the appendix.

### **3.3.4 Piezoelectric Pumping**

Piezoelectric pumping was accomplished using a AB1290B-LW100-R ceramic piezoelectric buzzer on a 12.3mm brass disc (DigiKey, Thief River Falls, MN), powered by an HP 33120A signal generator and connected via a Model 7500 10x voltage amplifier (Krohn-Hite, Brockton, MA) to provide an excitation voltage in the range from 30-100V at frequencies from 50-150Hz. The signal generator controls were used to set the AC peak-to-peak voltage amplitude and frequency and connected to the amplifier. The output of the amplifier was connected directly to the piezoelectric buzzer leads. The buzzer was set into fluidic chips using dry-film adhesive (3M) and sealed into place with a carefully applied ring of two-part epoxy (Loctite). All fluidic chips were fabricated a circular chamber that matched the dimensions of the piezoelectric buzzer and with no-moving-parts (NMP) valves fabricated on either side to create flow rectification. Two designs of NMP valves were utilized: a simple nozzle designed to compress laminar flow on one side and create turbulent flow on the other, and a recirculating nozzle designed to amplify that effect[319, 320].



### **3.3.5 Bacterial Culture**

Stbl3 *Escherichia coli* (ThermoFisher, Waltham, MA), a variant of the HB101 strain, were transformed using the pUC19 plasmid (ThermoFisher) for selection by ampicillin. 1µL of concentrated pUC19 plasmid were injected into a prepared hot-shot vial of E.coli, and mixed by gently turning the vial back and forth. The E.coli were allowed to incubate at room temperature with the plasmid for 30m before injecting 4µL into a prepared vial of 2mL LB Broth and 100µg/mL ampicillin. The vial was then incubated at 37C in a Model 10-140 Incubator (Quincy Lab, Chicago, IL) for two days to allow the ampicillin resistant bacteria to grow. The bacteria were then centrifuged for 1m at 2000g to form a pellet. The pellet was resuspended in 100µL of LB Broth, and then mixed with 100µL of 50% LB Broth, 50% glycerol prior in a screw-cap vial prior to storage at -20C.

### **3.3.6 DNA Isolation Protocol**

DNA solutions were prepared from Stbl3 E.coli transformed with the pUC19 plasmid (Sigma Aldrich, St. Louis, MO). Bacteria were grown in an incubator at 37C for two days in LB Broth containing 100µM ampicillin prior to harvesting and centrifugation. The resulting bacteria were then lysed and DNA was isolated using a DNEasy Blood and Tissue Kit (Qiagen) for solid phase extraction and purification of DNA. DNA samples were then analysed using a NanoDrop (ThermoFisher) to determine concentration and verify purity.

### **3.3.7 PCR Protocol**

Two PCR mixes were used for the experiments in this chapter. The first was TopTaq Master Mix (Qiagen), and the second was AmpliTaq Gold Fast Master Mix

(ThermoFisher). Experimental solutions consisted of 1X Master Mix, 500nM DXS forward primer 5'-CGAGAAACTGGCGATCCTTA,, Sigma Aldrich), 500nM DXS reverse primer (5'-CTTCATCAAGCGGTTTCACA, Sigma Aldrich) and DNA solution prepared from the bacterial lysate at final concentrations ranging from 5pg/ $\mu$ L to 5ng/ $\mu$ L in deionized, RNase and DNase pure water. All solutions were prepared fresh just prior to thermocycling. The PCR protocol utilized depended on the master mix used. For TopTaq master mix, a cycling protocol of 30s at 94C, 30s at 60C and 1m at 72C for 40 cycles was used. For AmpliTaq Gold Master Mix, an initial hot start step of 10 min at 95C was used, followed by a cycling protocol of 3s at 96C, 3s at 60C and 10s at 68C for 35 cycles.

### **3.3.8 Agarose Gel Electrophoresis**

Agarose gels were prepared using UltraPure Agarose (Invitrogen, Carlsbad, CA). 1g of agarose was added to 50mL of 0.5x Tris-Acetate-EDTA buffer and heated using a microwave oven until the agarose powder fully dissolved into solution. The resulting 2% agarose solution was then poured into a gel casting mold. The gel was allowed to cool until it had firmly set, and then was stored in 0.5x TAE buffer until needed for use. In a typical electrophoretic experiment, samples were incubated in 1X SybrGreen for 30 minutes to allow the dye to intercalate into any DNA present in the sample. 2 $\mu$ L of bromophenol blue tracking dye (10X BlueJuice, Invitrogen) was then added to 20 $\mu$ L sample aliquots just prior to loading into the wells of the agarose gel by pipette. Agarose gel electrophoresis was then performed at 100V on a JouleBox electrophoresis system (Stratagene, San Diego, CA) with the anode at the base of the gel until the tracking dye neared the end of the gel. The gels

were then photographed using either a BioRad transmission UV plate reader or an UltraLum UV Transilluminator.

## **3.4 RESULTS**

### **3.4.1 Disk/Cartridge Based PCR**

With Polymerase Chain Reaction (PCR) as an ideal starting point for detection of genetic resistance markers in bacterial samples in a microfluidic setting, the first step was to develop a system for rapid thermocycling that could be used in conjunction with fluorescent imaging of DNA intercalated with a dye molecule such as SybrGreen or EvaGreen – DNA specific dyes commonly used in real-time PCR (qPCR). The initial design paradigm was based on the premise of a disk-based fluidic chip 3D printed using a powder-based Z-Printer (Z-Print) for low-cost assembly (Fig. 3.1). The design utilized a series of wells that could be connected to channel structures for centrifugally controlled flow of reagents. With reagents and DNA samples loaded into the wells, the disk would rotate the wells between three ‘oven’ zones heated by metal thin-film heaters controlled by a resistance thermal detector (RTD) connected to a Basic Stamp control board. A similarly 3D-printed tray for the disk was used to house the heating elements. The tray was coated in Teflon spray in order to minimize friction from the rough surface.

Early testing of this design demonstrated that the use of Z-Printed materials was not viable for microfluidic design – rough surfaces and high porosity led to poor flow in channel structures, and liquid samples were absorbed into the surface during PCR experiments.

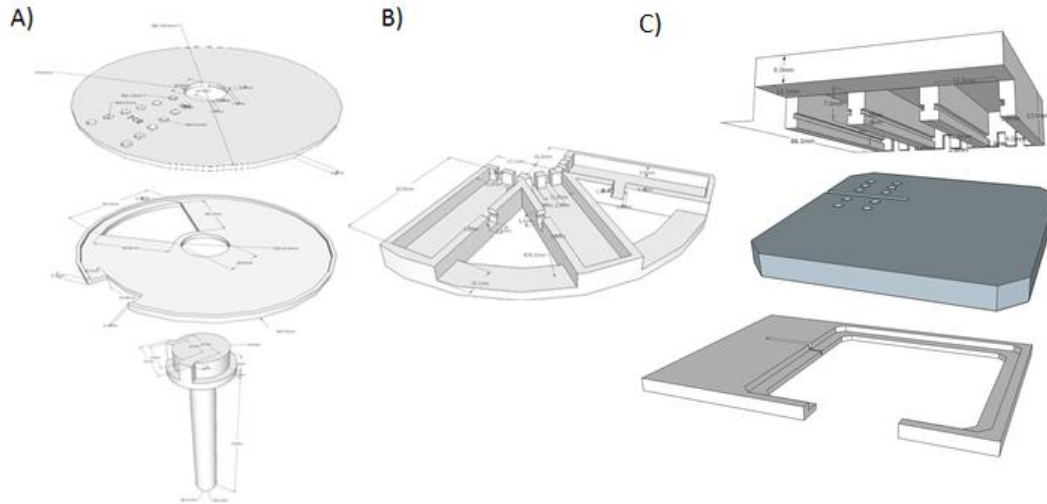


**Figure 3.1.** CAD diagrams of early disk and cartridge-based PCR system components. A) Stacked diagrams of test PCR disk with sample wells, disk tray with slots for central spindle, camera, and thermistor mounting, and central spindle for rotation of the disk using stepper motor control. B) Diagram of heater assembly with minimal material between oven zones to reduce thermal bleed. Kapton thin-film heaters were adhered into the base of chambers, with slots in the sides for thermistor leads. During construction, all gaps were sealed to create airtight chambers. C) Stacked diagram of cartridge-based PCR system, with 3D printed oven and stage assemblies surrounding a cartridge constructed from laser etched PMMA with wells and a slot to act as a track for a thermistor.

Following these results, the use of 3D-printed materials was discontinued for PCR chips – surface roughness and high porosity were found to be a hallmark of 3D-printed structures from all but prohibitively expensive photopolymer printers. The disk based design was also set aside due to a lack of planned utility for the capabilities of centrifugal force and the significant unnecessary design considerations required for it to function. A cartridge-based design that could be loaded into a desktop device was selected for the next design paradigm (Fig. 3.1C). A similar assay design was utilized – a series of wells patterned into a thin polymethylmethacrylate (PMMA) cartridge which could then be

moved on a ratcheted gantry between three oven zones set to PCR temperatures with fluorescent detection through a custom optical system.

Testing on the cartridge-based thermocycling chip design revealed that in the absence of absorption effects from chip materials, the oven-based design was inadequate for successful PCR, resulting in no detectable fluorescence bands following gel electrophoresis. Notable design failings included significant temperature lag due to the insulating effect of PMMA (0.18 W/mK thermal conductivity), and difficulty sealing the oven zones in the mobile system that led to waste heat and difficulty maintaining the high temperatures required for the DNA denaturation step of PCR.

### **3.4.2 Thermoelectric Thermocycling**

To address the failings of the cartridge thermocycling design, another paradigm was adopted. Instead of utilizing a series of ovens for temperature control, a single thermoelectric heating element (TEC) was used in contact with a PCR microchip containing sample wells, controlled using a custom circuit described in the appendices. In short, an Arduino Uno control board connected to an L6203 relay (DigiKey) was used to regulate input current from a 24V, 4A power source (NG60-5, BioTec) to a VT-127-1.0-1.3-7.1 30mmx30mm Peltier device (TE Technology, Traverse City, MI). The thermoelectric (Peltier) heating element allowed for rapid cooling in addition to heating, by far the most time-consuming step in traditional PCR systems. In order to minimize temperature lag between the TEC and the sample inside the microchip, it was decided to use a material with a high thermal conductivity as the base substrate. To this end, potential chip construction materials were tested for PCR inhibition with and without the presence

of bovine serum albumin, a common PCR adjuvant for increasing biocompatibility of substrates. Fig. 3.2 shows the results of these experiments. 20 $\mu$ L PCR samples, each with 50ng of E.coli DNA were prepared with primers for the DXS target gene, loaded into 200 $\mu$ L tubes and covered with 10 $\mu$ L of mineral oil. A small piece of test material was then loaded into each tube prior to undergoing PCR in an Eppendorf thermocycler. The materials tested were aluminum and copper as thermally conductive substrates (205 and 385 W/mK respectively), PMMA and dry-film adhesive (3M). The samples including aluminum, BSA coated PMMA and the adhesive all resulted in positive PCR results, while the copper (both conditions) and uncoated PMMA were both found to inhibit PCR.

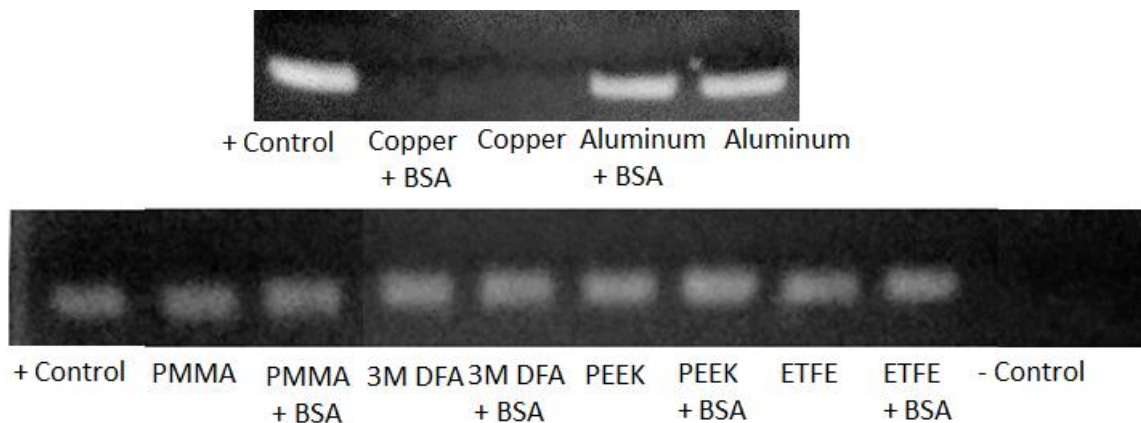


**Figure 3.2.** Results of agarose gel electrophoresis on samples incubated with 1x SybrGreen following PCR performed on an Eppendorf Thermocycler during incubation with various materials, with and without the presence of bovine serum albumin (BSA). All samples tested showed positive PCR results with the exception of copper, which demonstrated PCR inhibition regardless of BSA.

Due to the inhibitory effect demonstrated by copper on PCR, a test chip for the TEC thermocycler was constructed from 36-gauge aluminum form-pressed into wells and adhered to a band of BSA coated PMMA by dry-film adhesive to allow for a layer of

mineral oil to prevent evaporation (Fig. 3.4A). This chip was then placed into contact with the TEC via a thin layer of thermal paste (Tuniq, Taiwan).

To handle temperature control, two approaches were tested. First, an infrared thermal sensor designed for use with a BasicStamp control board aimed at the aluminum wells, and second, a 1k $\Omega$  RTD (DigiKey) was utilized in a wheatstone bridge configuration, connected to an op-amp to achieve a 10-fold voltage increase on input to an Arduino Uno control board (see appendix for circuit diagram). Custom PID (proportional-integral-differential) control software was written for the Arduino Uno control board utilizing the RTD as a thermal sensor (see appendix for code). PID control constants were tuned experimentally to achieve stable ramping and temperature control with minimal overshoot and oscillation.

To verify the calibration of the thermal sensors and ensure proper PCR thermocycling, a melt test was performed. Microchip wells were filled with compounds with known melting points close to common target temperatures for PCR thermocycling, P-bromophenol ( $T_m = 66.4C$ ), 2-Nitroaniline ( $T_m=71.5C$ ) and Benzil ( $T_m=95C$ ). A fourth well was filled with deionized water to determine the measured temperature at boiling. A program was set up to hit each of these temperatures and hold for 30 seconds in series and adjusted until the appropriate compound began to melt while held at temperature. Table 3.1 shows the measured temperatures from both the RTD and the IR sensor at the melting points of each compound, and the boiling point of water. The RTD measurement was consistently slightly high, ranging from 1-3 degrees above the target, likely due to the placement in contact with the TEC surface creating a differential with liquid samples in the

microchip wells. Microchip wells were filled with deionized water, and heated. During heating, both sensors were monitored and compared to each other as well as observed temperature when the water in the wells began to boil. Table 3.1 shows the relative temperatures measured during several points in heating, as well as when the water sample began to boil. The IR sensor consistently resulted in temperatures 10-15 degrees lower than the RTD placed on the TEC surface. The RTD also proved significantly more accurate during the boiling test. This was likely due to a combination of interference from the layer of mineral oil coating the well structure reducing the measured temperature from the IR sensor, and the high reflectivity of aluminum to IR signals. As a result, the RTD sensor was used in all further experiments. The target temperatures for PCR were adjusted to account for the differences between measured and actual results.

**Table 3.1.** Temperature calibration table for infrared thermal sensor and resistance thermal detector (RTD) using phase changes of compounds with known transition points. Data points represent approximate measured temperatures (+/- 1C) at which the transition point was observed for each sensor.

	<b>P-Bromophenol Melt (66.4C)</b>	<b>2-Nitroaniline Melt (71.5C)</b>	<b>Benzil Melt (95C)</b>	<b>Water Boil (100C)</b>
<b>IR Sensor</b>	50	55	84	87
<b>RTD</b>	67	73	97	102

Once the temperature measurements were verified, the stability of the system was tested. The thermocycling program was adjusted to utilize the target temperatures and timing of the TopTaq PCR protocol (Qiagen, Hilden, Germany), microchip wells were filled with deionized water, and the system was allowed to run for a 40 cycles. To test for



gradients across the TEC in this experiment, a second RTD was placed on the other side of the TEC and measured for the same period. Figure 3.3 shows an average cycle for timing of temperature changes, and the stability of holding at each target temperature for both RTDs. The time between temperature points was found to be 3s from 72 to 95C, 3s from 95 to 65C and 2s from 65 to 72C, much lower than that from the Eppendorf thermocycler, with comparable cycles of 22s, 34s, and 14s, respectively. A slight gradient of approximately one degree was observed between the two measured RTDs, but this was within the margin of error (~5% tolerance). The control program also resulted in temperatures consistently within 0.5C of target temperatures (Fig. 3.3B).

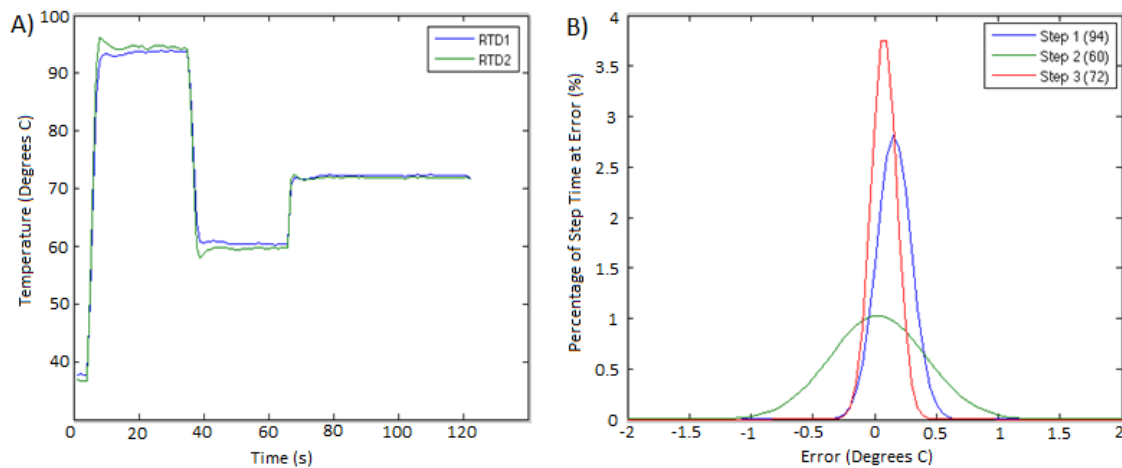


**Figure 3.3.** A) Measured temperature at two points on the chip surface over time during a PCR cycle with TopTaq protocol. RTD1 measurements were used for control of the PID heating system. B) Histogram of thermal stability at each step as measured over the course of 40 cycles. Error was consistently within 0.5 degrees of target temperature, with a slight positive bias (~0.1C) at the denaturing step.

With both temperature measurement and stability of thermocycling verified, a PCR test was run utilizing TopTaq master mix and primers for the E.coli DXS gene. 20 $\mu$ L samples including 50ng each of E.coli DNA were prepared and pipetted into the wells of a freshly prepared and autoclaved microchip. The PID control program was run for 40 cycles to allow for adequate thermocycling. Simultaneously, identical samples were run using an Eppendorf thermocycler as a positive control. Following completion, the samples were incubated with 1x SybrGreen dye for 30 minutes and loaded onto a 2% agarose gel with bromophenol blue tracking dye. Fig. 3.4C shows the resulting gel following reading on a BioRad Transmission UV gel reader. The TEC thermocycler resulted in a DNA band comparable to that of the Eppendorf system, indicating successful PCR.

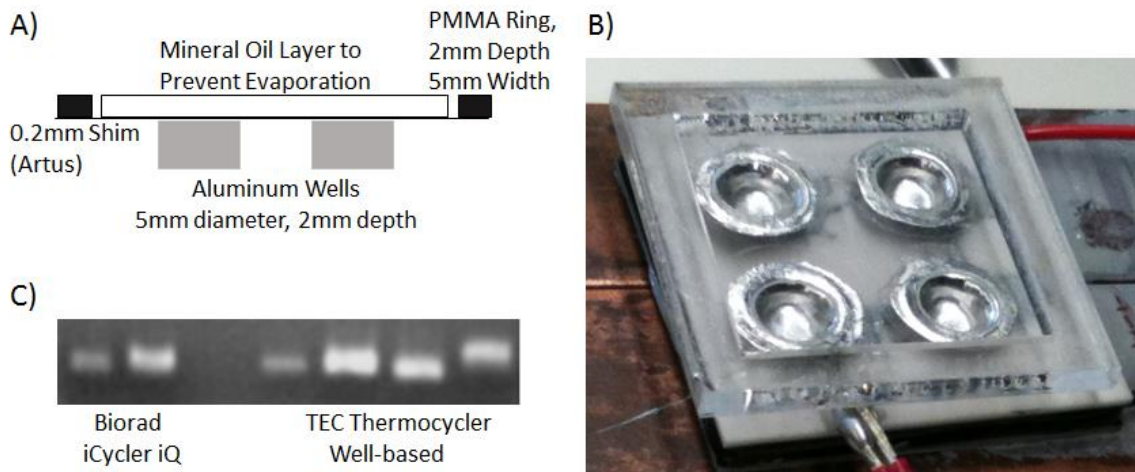


**Figure 3.4.** A) Cross-section of well-based PCR chip. 3M dry-film adhesive (100 $\mu$ m) used to bind components. B) Image of PCR chip set on TEC thermocycler. Thermal paste used to maximize heat transfer between TEC, aluminum wells and RTD sensor. RTD localized to external edge of well 1. C) Agarose gel electrophoresis of PCR results from TEC thermocycler wells and BioRad iCycler iQ for positive control following incubation for 20m with 1x SybrGreen dye.

Following verification of the thermocycling assembly using simple wells for PCR, a new microchip design was implemented to test for flow-through PCR in order to reduce the time required for analysis of clinical scale samples (~2mL) and allow for sample preparation systems and other assays to be added to the system in future work. To accomplish this, a channel-based design was utilized. Two primary designs were considered. In both cases, a consistent cross section for the microfluidic channel was maintained at 300 $\mu$ m depth and 2mm width (Fig. 3.5). For the first design, the channel structure was formed from pressed aluminum adhered to BSA-coated PMMA by dry-film adhesive (Fig.3.5D), and in the second the channel structure was prepared from layered dry-film adhesive between flat layers of 36-gauge aluminum and BSA coated PMMA (Fig. 3.5B).

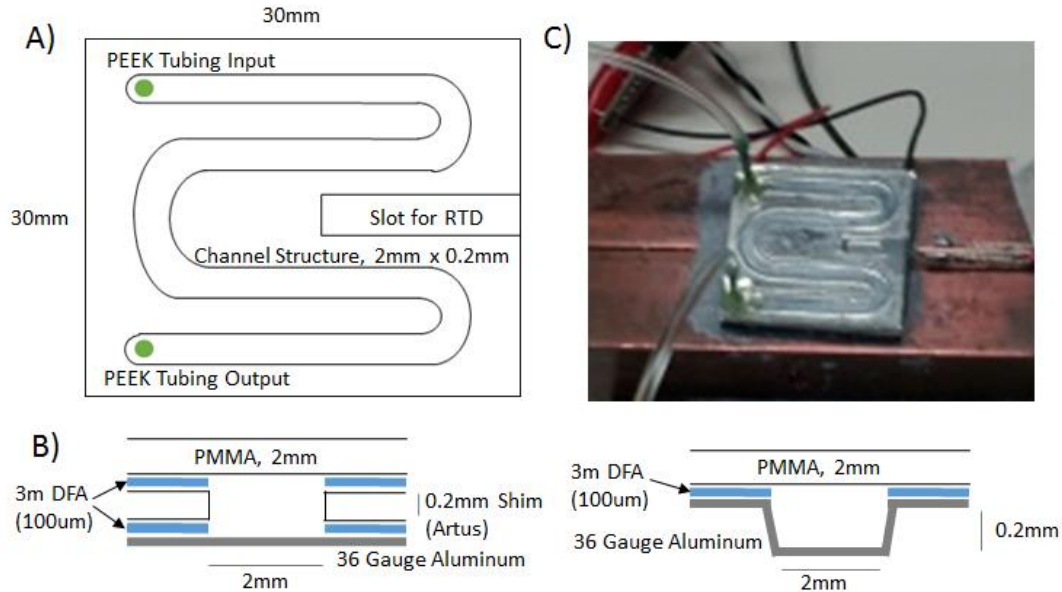


**Figure 3.5.** A) Top-down diagram of continuous flow PCR test chip. 2mmx0.2mm cross section either formed from pressed aluminum or cut from 3M dry film adhesive. PMMA Substrate used for top of chip, with inlets cut for 0.062”OD PEEK tubing. B) Cross section diagrams for channel structures formed from 3m DFA (left) and pressed aluminum (right). C) Image of pressed

aluminum channel test chip on TEC Thermocycler. Input tubing fed from KD100 syringe pump, output to sample collection tube.

To verify that these designs were functional, they were utilized for PCR on the TEC thermocycler using the SybrFast master mix protocol (ThermoFisher, Waltham, MA). 200 $\mu$ L of PCR sample were prepared as described above, including 250ng of DNA to maintain consistent concentration, and loaded into the microchip for thermocycling. While the SybrFast protocol calls for a 10 minute heating step for hot-start, this was not used for the microchip thermocycling to simulate continuous flow conditions in which a hot start could not be included on the TEC. Fig. 3.6A shows the resulting gel utilizing the microchip with channel structures cut from the dry-film adhesive. While the PCR was successful, the resulting bands were faint – likely due to the lack of a hot-start cycle in the experiment.

To confirm this, a second set of verification experiments were performed using the AmpliTaq Gold master mix protocol (ThermoFisher, Waltham, MA), chosen for both speed of thermocycling (16 seconds for an ideal cycle) and lack of SybrGreen in the reaction mix as an unnecessary complicating factor. First, the shortest necessary hot-start period was determined using an Eppendorf thermocycler. Seven 20 $\mu$ L samples were prepared using the AmpliTaq Gold master mix, primers for the E.coli DXS gene and 50ng of E.coli DNA each. One sample was placed into the thermocycler at the start of the 10 minute recommended hot-start period, and the others were added with 5m, 4m, 3m, 2m, 1m, 30s and 0s remaining. The resulting samples were run on a 2% agarose gel, which is shown in Fig. 3.6B. The minimum necessary hot-start time period for successful PCR using this reaction mixture was found to be two minutes. To allow for a safety margin, the PID

controller for the TEC thermocycler was set for a hot-start period of 240 seconds. A 200 $\mu$ L PCR sample was prepared using the same proportions as those used on the Eppendorf thermocycler and loaded into a microchip and run for 35 cycles on the TEC thermocycler. The resulting samples were then run on a 2% agarose gel and read using an UltraLum UV Transilluminator (Fig. 3.6C). Since successful PCR was achieved with this chip design, the pressed aluminum chip was discontinued due to the rounded channel edges achieved and difficulty in preventing tears.

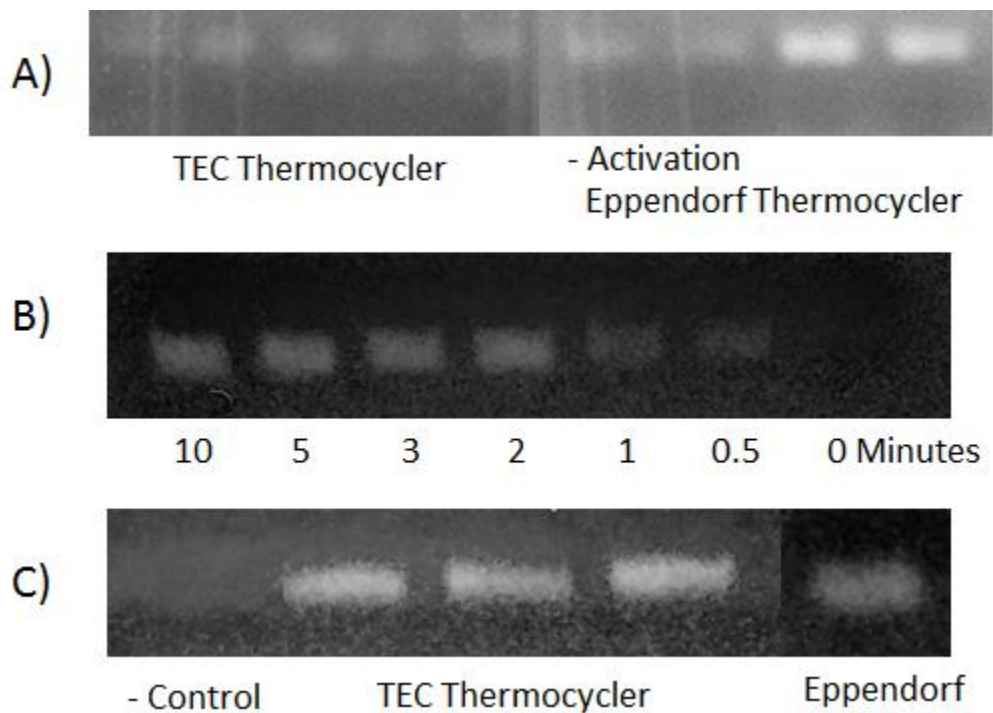


**Figure 3.6.** Gel electrophoresis results for PCR output from TEC Thermocycler compared to Eppendorf commercial thermocycler following incubation for 20m with 1x SybrGreen dye. A) SybrFast PCR protocol, all samples for TEC Thermocycler performed without hot-start activation step. B) Minimum Hot-start time verification performed on Eppendorf MasterCycler Gradient. Minimum hot-start period with no loss in PCR signal was two minutes. C) AmpliTaq Gold PCR protocol, including hot-start activation step, performed on TEC thermocycler and Eppendorf MasterCycler Gradient.

### 3.4.3 Pumping and Flow Control Systems

Multiplex detection is necessary for any rapid characterization of resistance markers in a bacterial sample due to the multitude of such markers to test for and the range of possible bacterial species. As a result, DNA hybridization array detection was selected as an ideal readout for the device due to its sensitivity[244] and strong compatibility with PCR. DNA probes are generally 20-30 nucleotides in length, however, resulting in melting temperatures between 70-80C, which would make consistent measurement in a thermocycling region impossible – thus limiting real time PCR in a continuous flow detector. This effect can be used for advantage, however – nearing the melt point of a DNA probe reduces the likelihood of mismatch and non-specific binding, resulting in much greater specificity of a hybridization array located spatially close to a thermocycling region[321, 322].

To utilize this effect, a novel design paradigm was implemented in which a looped section was utilized consisting of the thermocycling zone localized directly above the TEC thermocycler, and a DNA hybridization detection zone outside, but spatially near the thermocycler. In order to allow for a continuous flow system with such a design, an integrated pumping system in the loop to maintain flow separate from the main flow in the device was required. The system needed to be fully located within the volume of the loop to prevent excess volume from being external to the thermocycling zone, which could lead to primer-dimer effects due to significant temperature drop[151], as well as longer PCR times. Four potential in-channel pumping regimes were considered: electrokinetic (EK), electroosmotic (EO), pneumatic and acoustic pumping. While EK and EO pumping both

maintained the advantage no moving parts, pumping speed was heavily dependent on ionic strength of the solution – a factor that could not be considered consistent in clinical samples – and resulted in low flow rates even at ideal conditions ( $<10\mu\text{L}/\text{m}$ ). Pneumatic pumping required both significant use of moving parts that could break down, as well as the use of a deformable substrate such as PDMS that could lead to bubble formation under PCR conditions. Acoustic pumping (also known as piezoelectric, Fig. 3.7) utilized minimal moving parts while still maintaining high flow rates, so further experimentation was performed using this regime.

As the acoustic pumping system relied on flow rectification to create a net flow in one direction, the design of the required no-moving-parts (NMP) valves was considered to maximize flow profiles. Two main designs were considered for the NMPs utilized in flow rectification (Fig. 3.7B): a nozzle-NMP (nNMP), a simple constriction designed to constrict laminar flow before a sudden opening[323], leading to turbulent flow on the other side to create a flow differential; and a recirculation NMP (rNMP), a series of constrictions and openings designed to increase the flow differential in the two directions through multiple layers of laminar/turbulent flow shift[319, 320].

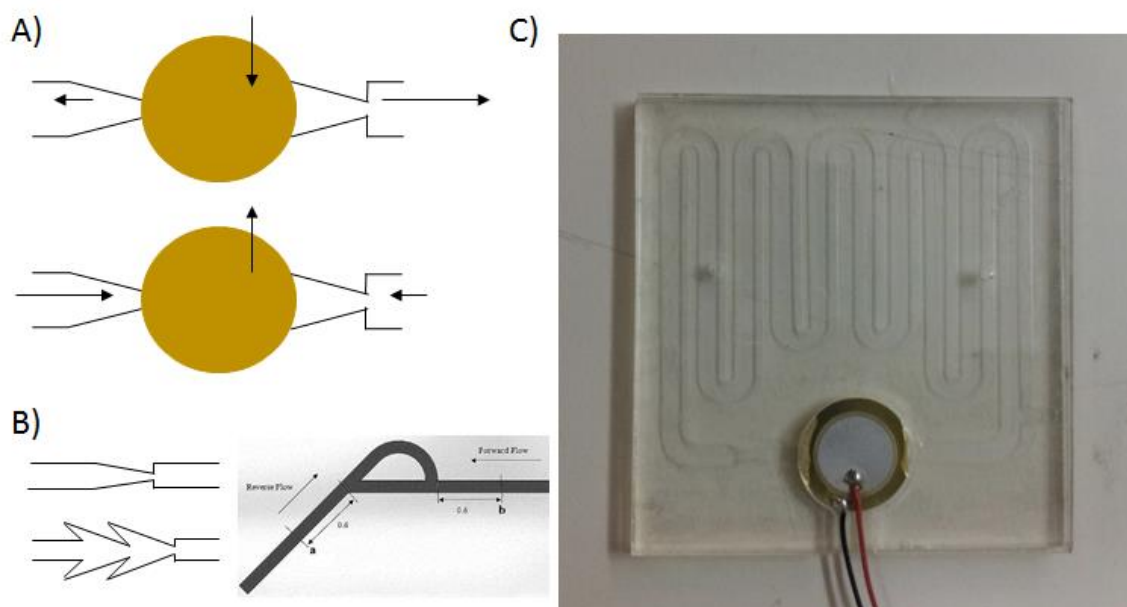


**Figure 3.7.** A) Operational principle diagram of piezoelectric pump. No-moving part (NMP) valves used to rectify flow created from deflection of the piezoelectric buzzer. Flow enters the chamber when the buzzer deflects upwards, and out when it deflects downwards. The NMP valves each limit flow in one of these directions, leading to a net flow through the pump. B) Fluidic NMP valve designs, nozzle (top left), recirculating (bottom left), Tesla Valve (right, reproduced from Thompson, et al)[324]. C) Image of a test chip for piezoelectric pumping flow. Channel structures cut from 3M dry film adhesive (200 $\mu\text{m}$ ) between layers of PMMA. Nozzle NMP design used for this chip.

In order to compare the two designs, looped flow chips were fabricated from PMMA with channel structures cut from a 300 $\mu\text{m}$  layer of dry-film adhesive to mimic the structure of thermocycling PCR chips used (Fig. 3.7C). One each was prepared for the two NMP designs. A series of marks were etched into the surface of the PMMA at 1mm intervals using a CO<sub>2</sub> laser to serve as a ruler. The chip was then filled with deionized water mixed with a small quantity of 45 $\mu\text{m}$  diameter silicon microbeads and placed under a Zeiss microscope. The etched ruler region was placed in focus, and the piezoelectric buzzer was activated with a signal generator and the ruler zone recorded. First, the frequency was



modulated from 50-150Hz and the flow rate measured by calculating the velocity of microbeads through the ruler zone at 70V input(Fig. 3.8A). The maximum flow rate was found to occur at a signal frequency of 110Hz for both nNMP and rNMP, though the nNMP had a significantly higher flow rate. The frequency was then set to 110Hz, and the voltage modulated from 30-100V and the results recorded as before for both nNMP valve (Fig. 3.8B) and rNMP valve (3.8C). Due to its higher flow rate, the nNMP was chosen for future usage, with a 70V input to match a desired flow rate of  $160\mu\text{L}/\text{m}$  in the PCR loop.

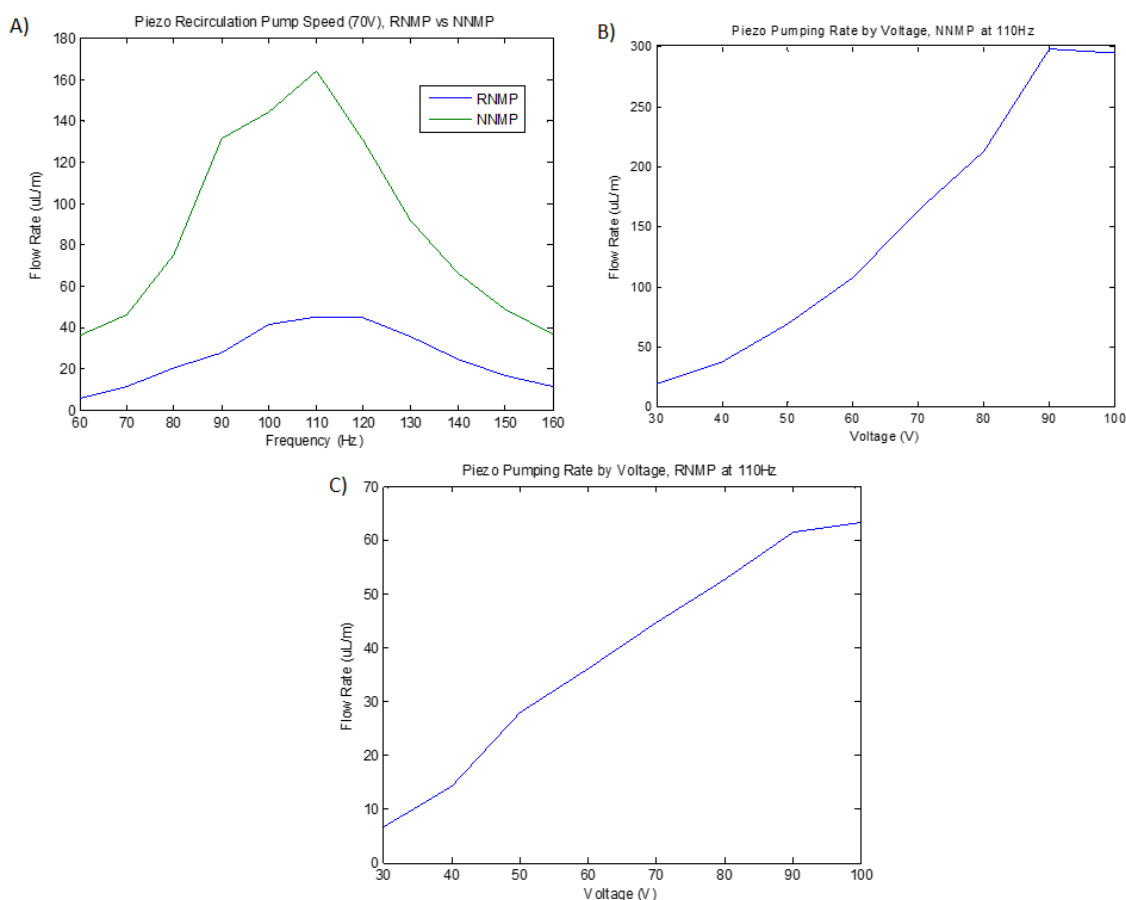


**Figure 3.8.** A) Flow rate generated from piezoelectric pump at 70V for nozzle and recirculating NMP valve designs at frequencies from 60 to 160Hz. Maximum flow rates occurred at 110Hz for both valve designs, resulting in a peak of  $162\mu\text{L}/\text{m}$  for the nozzle valve, and  $40\mu\text{L}/\text{m}$  for the recirculating valve. B) Pumping flow rate for nNMP valve by voltage while frequency was held

constant at 110Hz. Maximum attained flow rate was 300 $\mu$ L/m, well above desired in-loop flows. C) Pumping flow rate for rNMP valve by voltage while frequency was held constant at 110 Hz. Flow rate appeared to plateau at a maximum of approximately 60 $\mu$ L/m.

### **3.4.4 PCR Verification**

While acoustic pumping proved ideal for consistent and tunable flow rate regardless of solution ionic strength, the requirement for a piezoelectric buzzer carried some risks for PCR – nearly all piezoelectric buzzers use brass as the deflecting metal, and as brass is an alloy of copper and tin, it carries copper ions that can inhibit PCR. To test if this concern was warranted, 20 $\mu$ L PCR samples utilizing AmpliTaq Gold master mix, primers for the E.coli DXS gene and 50ng of E.coli DNA were loaded into tubes with small slivers of brass cut from a piezoelectric buzzer, uncoated and coated with BSA. As shown in Fig. 3.9A, the brass was found to inhibit PCR, both coated and uncoated.

In order to avoid this problem, three potential modifications were made to avoid contact between the brass and PCR solution while maintaining the flexibility required for pumping: coating the brass with a layer of dry-film adhesive, with a layer of dry-film adhesive followed by a layer of aluminum foil (0.016mm), and a PDMS coating. The experiment was then repeated with each of these conditions. As shown in Fig. 3.9B, all three treatments resulted in successful PCR, though the dry-film adhesive alone, and PDMS both resulted in a broadened DNA band on the gel indicative of damaged product.

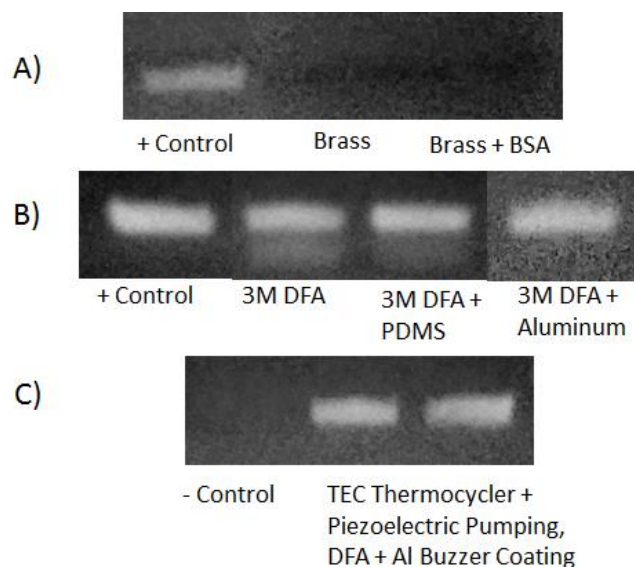


**Figure 3.9.** Gel electrophoresis results for PCR samples following incubation for 20m with 1x SybrGreen Dye. A) Samples incubated with brass and BSA-coated brass during PCR on Eppendorf thermocycler. In both cases, copper ions leached from the brass inhibited amplification. B) Test series for buzzer coatings to prevent PCR inhibition. Dry film adhesive (3M) was used for adhesion to buzzer and subsequently coated with nothing, polydimethylsiloxane (PDMS) and aluminum (0.016mm). All three resulted in amplification, though DFA alone and DFA/PDMS coatings resulted in broken products. C) On-chip PCR results from TEC Thermocycler while undergoing piezoelectric pumping with a buzzer coated in DFA and aluminum.

As a result, the piezoelectric buzzer was coated with a 100 $\mu$ m layer of dry-film adhesive, followed by aluminum foil and placed into a thermocycling chip. The chip was then loaded with 200 $\mu$ L of PCR sample utilizing AmpliTaq Gold master mix, primers for the E.coli DXS gene and 2.5ng/ $\mu$ L of E.coli DNA. The chip was then placed on the TEC thermocycler and run for 35 cycles while under acoustic pumping at 70V and 110Hz. Fig. 3.9C shows the results after incubating with SybrGreen and loading onto a 2% agarose gel. The strong DNA bands indicated successful PCR, and thus prevention of contamination by copper ions from the brass disc in the piezoelectric buzzer.

### **3.5 DISCUSSION**

Polymerase chain reaction serves as an ideal assay for characterization of bacterial resistance markers due to its applicability to a wide range of genetic sequences with extant probe panels designed for detecting common pathogens and resistance markers, in addition to ease of multiplexing and translatability of a thermocycling design to other assays such as HDA and LAMP. While these strengths have led to the ubiquity of PCR as a gold standard in pathogen characterization, it also carries a number of unique challenges for a microfluidic system. These include precise temperature control and prevention of thermal gradients, material properties under high temperature, microbubble prevention and high pressure under heating in a microchamber.

As discussed in this chapter, a number of design approaches were undertaken to address such potential failure modes. Rough surfaces, such as those from 3D-printed materials were found to contribute to microbubble formation due to interfacial trapping at channel walls during sample loading, air heated oven designs resulted in significant temperature lag in enclosed chips due to low thermal conductivity of transparent substrates. Open well systems avoided this constraint as well as high pressure under heating, but required separate loading of reagents into wells and a mineral oil layer to prevent evaporation.

TEC mediated heating using an RTD for temperature measurement and control resulted in rapid and accurate thermocycling that could be applied to an enclosed microfluidic structure fabricated with a highly thermally conductive substrate such as aluminum. With careful use of dry-adhesive film as a bonding agent and externally applied

pressure, leaks due to spikes in microchip pressure were avoided leading to successful thermocycling as demonstrated by fluorescent measurement of DNA intercalating dyes. Temperature control was tuned to prevent temperature overshoot and characterized, demonstrating minimal time between PCR steps and consistent thermal stability within 0.5C of target temperatures.

To minimize assay time for clinical samples, a continuous-flow microchip design was implemented and adapted to a looped thermocycling system with built-in hybridization detection zone for real-time measurements with strong binding specificity. In-line pumping strategies were evaluated to allow for separated control between the loop and overall device flow. Piezoelectric pumping was selected for minimal moving parts and rapid net flow profiles. Characterization of this pumping regime demonstrated maximum achievable flow rates in excess of 120 $\mu$ L/m, well above the desired 80 $\mu$ L/m loop internal flow rate.

A fully constructed thermocycling loop microchip with built-in acoustic pumping was demonstrated and successful PCR was verified under an internal pumping rate of 80 $\mu$ L/m using measurement of DNA intercalating fluorescent dye following gel electrophoresis. DNA band strength was found to be comparable to that resulting from an Eppendorf Thermocycler. This opened the way for development of a loop-internal DNA hybridization array for multiplex PCR detection.

### **3.6 ACKNOWLEDGEMENTS**

The author would like to thank Lorenzo D'Amico for his invaluable help in learning PCR techniques and photolithography. He would also like to thank Thomas Anderson for

his assistance in 3D printing and machining of fluidic structures, as well as instruction in the use and maintenance of both a CO2 and exciplex lasers.

## CHAPTER 4:

# Digital Micromirror LSPR Imaging and Optimized Tunable Nanoprism Synthesis

### 4.1 ABSTRACT

Even with Polymerase Chain Reaction (PCR) mediated amplification of DNA, highly sensitive detection is required to attempt to detect the lowest possible concentrations of DNA, resulting in both more rapid detection and sensing of low concentration targets. While fluorescence quantification is standard for sensitive DNA hybridization systems, the need for floating label molecules in the reaction mix that can inhibit PCR and complicate the system. In this regard, nanoparticles provide a solution: localized surface plasmon resonance provides a highly sensitive, label-free detection regime that couples well with DNA hybridization mechanics through 5'-thiol modified DNA probes. While LSPR holds many attractive properties, it is underutilized in microfluidics, likely due to the difficulties inherent in nanoparticle synthesis, tuning, and optical interrogation.

In this chapter, silver nanoprism synthesis is optimized to achieve stable, monodisperse colloids capable of thiol-binding for easy adhesion to glass substrates – important not only for LSPR applications described here, but also SERS and Raman Scattering. Numerous synthesis techniques have been reported, but the influence of reagents on reproducibility and stability of nanoplates has not been characterized. We studied a citrate-stabilized, peroxide-based synthesis of AgNPrs and demonstrated that concentration of secondary reducing agent is critical to AgNPr stability. We further demonstrated that varying the concentration of sodium citrate in the seed solution, dilution factor, and rate of silver nitrate addition can be used to tune nanoprisms with a wide variety of sizes and narrow absorption peaks while still allowing functionalization with thiol-

binding. These findings will allow for more precise control of chemical AgNPr synthesis for solution and surface-based plasmonic applications.

Additionally, we demonstrated the development, characterization and optimization of a low-cost spectroscopic imaging system for LSPR utilizing spatial diffraction onto a digital micromirror device to generate frequency discrimination. The resulting device achieved 2nm resolution across a band of light from 560-640nm, capable of taking a spectral image in 40 seconds for a spot size of 3.3mm diameter. The system was able to strongly resolve spectral changes under treatment of nanoparticle layers with different dielectric solvents, demonstrating potential for detection of DNA hybridization events.

## **4.2 INTRODUCTION**

While the results of the previous chapter described a microfluidic thermocycling chamber with potential for in-channel real-time detection, the actual detection system was left nebulous. While a number of microfluidic detection methods have been demonstrated for DNA, including hybridization[325], and electrochemical effects[326], simultaneous detection of multiple targets in a multiplexed assay necessitates the use of probes specific to targeted DNA sequences. In this situation, hybridization arrays are the gold standard – spatial separation of target-specific probes immobilized on a surface to allow parallel detection of a large number of target molecules[247].

Classically, DNA hybridization arrays utilize fluorescent markers for detection – hairpin probe sequences maintain a fluorescent marker covalently linked to a quencher, which are then cleaved by DNA binding events. While this approach is simple and lends itself well to optical detection, it lacks in sensitivity and has limited specificity – once the bond between marker and quencher is cleaved, even by non-specific binding, it cannot be reformed[327]. This can be avoided by use of labeled markers in the reaction solution that



bind to the probe-target sequence complex, but adds an additional layer of complexity and floating labels can contribute to primer-dimer errors during PCR amplification.

A number of alternative approaches to detection of hybridization events have been studied in recent years, including electrochemical measurements[326], molecular transistors[248], and plasmonic systems[249, 250]. Of particular interest are plasmonic approaches, utilizing the unique properties of noble metals to measure target binding. As demonstrated for surface plasmon resonance (SPR), thin layers of noble metals (gold, silver and copper) can couple the evanescent field of totally-internally-reflected (TIR) light into surface waves known as plasmons at a characteristic reflection angle for each wavelength of incident light that changes with the local dielectric constant on the other side of the noble metal surface – allowing for highly sensitive detection of changes in mass of biomolecules in close proximity to the surface, such as DNA targets binding to probes[48].

Localized Surface Plasmon Resonance (LSPR) serves as an extension of these findings – noble metal nanoparticles have a strong extinction at characteristic wavelengths of light in the visual to near-infrared range, depending on the size and shape of the particle[49, 266]. As with SPR, this extinction peak shifts with changes in the local dielectric constant, allowing for measurement of hybridization effects among many other potential assays. Whereas SPR requires a complex prism configuration for precise angles and TIR, LSPR measures direct extinction of light passing through a nanoparticle monolayer, greatly simplifying the necessary optical pathway. With 2D spectroscopic analysis, LSPR can be used for imaging of a hybridization array for highly sensitive detection[271].

The use of LSPR imaging in a potentially noisy system such as that present in a microfluidic system relies on the strength of extinction peak shift of the nanoparticles adhered to the substrate when the local dielectric constant changes. Shaped nanoparticles

with sharp edges or corners, such plates, cubes, prisms and nanoholes significantly increase the local electric field at these points, leading to a marked increase in the optical shift[54]. Due to their greatly improved optical properties over spherical particles, triangular nanoprisms are commonly used for SERS and LSPR applications[49]. While any of the noble metals carry the necessary properties for LSPR, gold and silver offer the strongest responses. Silver nanoplates offer a stronger spectral response than gold, but can be more difficult to synthesize and cannot be utilized *in vivo* due to their natural toxicity[328]. As a result, silver nanoprisms are ideal for *in vitro* analysis where toxicity is not a concern.

There are numerous techniques currently described for synthesizing silver nanoplates, ranging from the photoinduced[288] methods to solvo-thermal[298] and seeded growth[301]. In virtually all synthesis techniques, a simple reduction reaction is first used to synthesize small silver nanospheres (3-5nm diameter), after which varying approaches are taken to reach a nanoplate structure. For photoinduced methods, a ligand (BSPP) is used to sequester silver ions from the bulk reaction and slowly release them over time under a laser tuned to the dipole moment of the desired size of nanoprism. A second laser tuned to the quadrupole can be used to isolate a specific size rather than two bands[297]. These techniques are well studied and produce a relatively monodisperse sample, though they suffer the drawback that the necessary ligand is believed to inhibit particle functionalization due to strong adhesion to the particle surface.

Solvo-thermal techniques avoid the problem of surface binding ligands, instead relying on thermodynamic control to tune the final shape of the particles. These techniques rarely result in monodisperse samples and can be difficult to control without precision equipment. Seeded growth techniques utilize an etchant, such as hydrogen peroxide, in combination with a second weaker reducing agent and a surface stabilization agent to induce directional growth of nanoparticles under slow addition of silver ions, with final

size depending on the amount of silver added[300]. These techniques rely on the ratios of etchant/reducing agent as well as the stabilization agent used to control the reaction. For the purposes of an LSPR imaging based biosensor, a monodisperse sample of nanoprisms with strong edges resulting in a narrow absorption peak is critical. The particles must also be functionalizable and be stable over time to allow for storage.

This chapter enumerates both the selection and optimization of silver nanoprism synthesis with an eye towards use in an LSPR imaging system, as well as the design and testing of a low-cost optical system for 2D spectroscopic imaging of nanoparticle monolayers. Optimization of silver nanoprism synthesis was accomplished by interrogating the effects of reagents and conditions on particle stability, functionalizability, and optical properties to obtain prisms with strong absorption peaks capable of thiol-binding to substrates and probes. An optical imaging system using diffracted light and a digital micromirror device to achieve spectroscopic images was constructed and evaluated for strengths and weaknesses, and potential for detection of DNA hybridization events following PCR amplification in a microfluidic system.

## **4.3 MATERIALS AND METHODS**

### **4.3.1 Silver Nanoprism Synthesis**

Prior to synthesis, all reagent solutions were prepared fresh – sodium borohydride and L-ascorbic acid are reducing agents and thus lose reduction potential over time due to oxidation. In a typical experiment, a solution consisting of 39.3mL diH<sub>2</sub>O, 2mL Trisodium Citrate (TSC) (75mM), 256μL Hydrogen Peroxide (H<sub>2</sub>O<sub>2</sub>) (0.6%), 186μL Silver Nitrate (AgNO<sub>3</sub>) (10mM) was prepared (Sigma Aldrich, St. Louis, MO). Under vigorous stirring, 192μL of Sodium Borohydride (NaBH<sub>4</sub>) (100mM) (Sigma Aldrich) was rapidly added to initiate reduction, and the solution immediately changed to a pale yellow color. After about five minutes, the color shifted to a golden yellow. After this color shift, the solution was

stored overnight at room temperature to allow the  $\text{NaBH}_4$  to complete its reduction. Following this aging period, 2.1mL of the seed stock were added to a clean 8mL vial and stirred vigorously. 200 $\mu\text{L}$  of L-Ascorbic Acid (5mM) (Sigma Aldrich) were added to this mixture, followed by addition of  $\text{AgNO}_3$  (10mM) dropwise until the solution reached a color indicative of desired nanoprism size (i.e. purple for  $\sim 35\text{nm}$  edge length particles with an extinction peak at 550nm) was reached (typically 100 $\mu\text{L}$ ).

When performing flow rate experiments to determine the optimal conditions for nanoprism synthesis, a modified version of the above protocol was used. Seed stock was prepared as before, after which 2.1mL of the seed stock were added to a clean 8mL vial and stirred vigorously. 200 $\mu\text{L}$  of L-Ascorbic Acid (5mM) were added to this mixture. A KD Scientific syringe pump was then used to inject 100 $\mu\text{L}$  of  $\text{AgNO}_3$  at a controlled rate (between 15 $\mu\text{L}/\text{min}$  and 400 $\mu\text{L}/\text{min}$ ).

Larger nanoplates were synthesized by diluting seed solution prior to the addition of L-ascorbic acid and silver nitrate. Seed solutions were prepared proportionally in smaller quantities and then diluted by addition of  $\text{dH}_2\text{O}$  to reach 2.1mL. The reaction then proceeded as above. Typically, dilutions were used as follows: 1x for nanoplates with absorption peaks up to  $\sim 550\text{nm}$ , 1/2x for  $\sim 550\text{-}590\text{nm}$  (1.05mL seed stock, 1.05mL  $\text{dH}_2\text{O}$ ), 1/4x for  $\sim 590\text{-}630\text{nm}$ , 1/8x for  $\sim 630\text{-}700\text{nm}$  and 1/12x for NIR nanoplates.

#### **4.3.2 Characterization of Silver Nanoprisms**

Characterization of the size and morphology of silver prisms was performed using TEM. Samples were placed as drops onto 100 mesh formvar/carbon coated copper for approximately 1 hour. Samples were blotted dry from the grids with filter paper and samples were allowed to dry. Samples were then examined in a JEM 1010 transmission electron microscope (JEOL, USA, Inc., Peabody, MA) at an accelerating voltage of 80 Kv. Digital images were obtained using the AMT Imaging System (Advanced Microscopy

Techniques Corp., Danvers, MA). Optical spectra were determined using a BioTek SynergyHT UV-Vis spectrometer. Samples were diluted to an optical density less than four, after which 300 $\mu$ L was placed in a single well of a 96 well plate for reading. Absorption spectra were then normalized to have an Area-Under-the-Curve (AUC) of 1.

### 4.3.3 Nanoprism Stability Calculations

Changes in absorption spectra of nanoparticle samples were used as an indicator of stability in solution. Calculations were performed by first normalizing both initial absorption spectra of a nanoplate solution and those obtained after 24 hours by their AUC to obtain area-weighted spectra. Relative error was then calculated as the disagreement between the two spectra expressed as a percentage of the agreement according to the following formula:

$$Instability = I_{init} \oplus I_{24h} / I_{init} \cap I_{24h}$$

From the nanoplate spectra, this was calculated using the following equation:

$$Instability = \frac{2(\sum(I_{init}^n - I_{24h}^n))}{(2 - \sum(I_{init}^n - I_{24h}^n))}$$

Ideal stability (i.e. no change in the absorption spectrum) would result in a 0 under this calculation. Anything below 0.15 can be considered to be stable due to noise in spectral measurements.

### 4.3.4 Nanoprism Adhesion to Glass Substrates

Two techniques were used for nanoprism adhesion to glass, which were subsequently compared to determine which was preferable for usage in the completed device. First, a solution of 2% (3-mercaptopropyl)trimethoxysilane, 5% diH<sub>2</sub>O in 2-propanol was prepared. Standard glass slides were treated with 0.05M Sodium Hydroxide for 30m at 80C and then washed with diH<sub>2</sub>O. 50 $\mu$ L droplets of the MPTMS solution were

placed on the surface of the slides and placed in an oven heated to 90C for two hours, which evaporated the MPTMS solution and allowed for an even surface coating. The slides were then removed from the oven and washed in diH<sub>2</sub>O before being left in the nanoprism solution overnight.

In the second technique, glass cover slips were placed in a solution of 0.1% poly-L-lysine for 30 minutes, after which they were removed and dried under a jet of nitrogen. The PLL coated slides were then placed in the nanoprism solution for one hour. The optical density of the nanoprism solution used varied, but was always held above 3.

For both methods, after the nanoprism incubation, the slides with nanoprism monolayers were removed, washed in diH<sub>2</sub>O and placed in a separate diH<sub>2</sub>O bath to prevent drying. When ready to be used, the nanoprism coated cover slips were removed from the deionized water bath and dried under a jet of nitrogen prior to functionalization.

#### **4.3.5 Silver Nanoprism Functionalization**

Thiol-linked probes targeted to the DXS gene were obtained from Sigma Aldrich, 5'-[Thi-C6]ATCGCTGAACGCTACGCTGGTCGATAT. A droplet containing DNA probes (35μM) was incubated on the detection zone of a nanoprism coated coverslip for one hour. The coverslip was then washed with diH<sub>2</sub>O and dried under a nitrogen jet. The probe concentration was chosen as the minimal concentration required to maximize shift in the absorption spectra of the nanoprisms.

#### **4.3.6 Hyperspectral Imaging**

Hyperspectral imaging of silver nanoprism monolayers was accomplished using a Leica DM6000M microscope and PARISS control software (LightForm, Asheville, NC). The microscope was set to brightfield transmitted light using a halogen lamp and 20x objective. PARISS control software was used to control stage movement and image acquisition. Prior to taking hyperspectral measurements, a lamp spectrum was recorded by

placing an uncoated glass slide on the microscope stage, appropriately setting integration time and taking 10 acquisitions of a single slice. Once the lamp spectrum was acquired, the nanoparticle coated slide was placed on the stage and the integration time was set as before. The hyperspectral image was then taken using 100 acquisitions with 5 averages.

After image acquisition, resulting data were analyzed in MatLab using custom functions. Lamp spectra were used to normalize sample spectra to obtain 2D maps of absorption spectra. These maps were then averaged to obtain the average absorption spectra of nanoplates in the imaging area between 450 and 800nm.

#### **4.3.7 LSPRi Optical Assembly**

A custom optical system was developed to image the nanoprism monolayer detection zone of the microfluidic chip and measure nanoplate spectral changes over time correlating to shift in the local dielectric constant. White light was supplied using a CREE XP-G2 5W Warm White LED (RapidLED, Burlingame, CA). Light from the LED was collimated through a narrow slit onto a diffraction grating (600 grooves/mm). The diffracted light was then incident onto a DLP3000 608x684 pixel digital micromirror device (DMD) (Texas Instruments, Dallas, TX) creating a spatial resolution of wavelengths. The DMD was used to reflect specific frequency bands onto an optical fiber, after which it was collimated into a 3.3mm diameter beam passing through the nanoprism-coated detection zone of the PCR chip and incident onto a Hamamatsu C2400 CCD camera with images collected by frame grabber at 29.97 frames per second. Later experiments replaced the Hamamatsu CCD with a Reitiga EXi camera (QICam) with 250ms integration time.

#### **4.3.8 2D Spectroscopic Imaging Analysis**

An initial spectral sweep was performed from 550-650nm and recorded. This was used as the baseline data set for determining optical shift. During imaging, this spectral

range was repeatedly swept using the optical assembly. The image taken at each wavelength was normalized on a pixel-by-pixel basis by the spectral output of the LED at that wavelength and then subtracted from the matching image from the baseline sweep to create a difference map. The difference maps were then summed across the entire spectrum to obtain an integrated difference map which was then displayed using false color.

## **4.4 RESULTS**

### **4.4.1 Selection of Nanoprism Synthesis Regime**

Following the selection of silver nanoprisms as the ideal form of nanoparticle for use in an in-vitro LSPR based biosensor, it was necessary to develop a reproducible synthesis for monodisperse, stable nanoprisms. Particles with an absorption peak around 600nm were ideal to take advantage of optical detection utilizing visible light by a simple CCD for minimal detector cost while maximizing spectral shift under a changing local dielectric field. In order to determine an appropriate starting point for nanoprism synthesis, a number of representative synthesis techniques were utilized to prepare particles, which were then compared for monodispersity and functionalizability.

Representative techniques for photo-induced synthesis[288, 329], hydrogen peroxide mediated seeded growth[300, 330], starch-stabilized seeded growth[331] and ascorbic acid mediated seeded growth[301] were utilized to synthesize silver nanoplates. Figure 4.1 shows absorption spectra acquired from each synthesis technique. As demonstrated, photo-induced, starch-stabilized and one citrate-stabilized seeded growth technique resulted in relatively monodisperse nanoprisms. No solvo-thermal methods were tested, as they require significantly more complex reaction chemistries and precise control of high temperature/pressure systems. Poly-vinyl pyrrolidone stabilized synthesis was similarly avoided for suspected issues with bioconjugation[330].



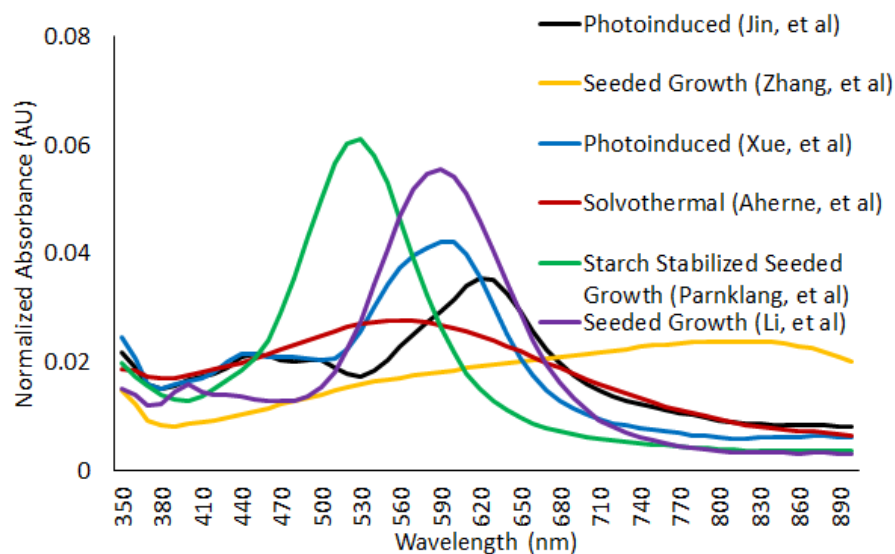


**Figure 4.1.** Representative optical extinction spectra for various silver nanoprism synthesis techniques, all spectra normalized to an area-under-the-curve (AUC) of 1. Photoinduced techniques include Jin, et al and Xue, et al. Solvothermal techniques include Aherne, et al. Seeded growth techniques include Zhang, et al and Li, et al. Parnklang, et al utilizes soluble starch as a stabilizer for peroxide etchant growth.

In order to assess the ability of the nanoparticles from each of these syntheses to be functionalized, a simple click-chemistry experiment was utilized to qualitatively measure both thiol binding and surface adhesion to a glass substrate. In short, glass slides were incubated for 30 min in a 0.01% solution of Poly-L-Lysine and then dried under a jet of nitrogen. The coated slides were then incubated for one hour in colloidal nanoprism solutions from each of the preparations diluted to an OD of 3, after which they were washed and dried under a jet of nitrogen. Silver nanoprisms with a maintained affinity for thiol binding would form bonds with the –SH groups on cysteine in the Poly-L-Lysine physisorbed to the glass substrate, resulting in a visible monolayer of nanoprisms. As shown in Figure 4.2, only the citrate-stabilized seeded growth method resulted in a visible monolayer, and thus functional nanoplates.

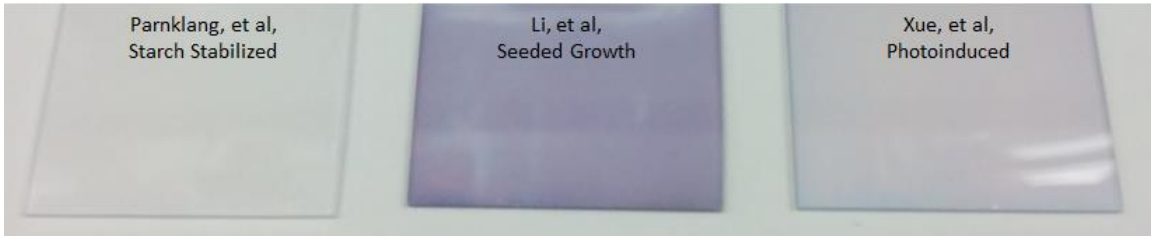


**Figure 4.2.** Poly-L-Lysine modified glass slides incubated for 30 minutes in OD 3 colloidal nanoprisms solutions prepared using starch stabilized, seeded growth and photoinduced synthesis techniques. No monolayer was formed from starch-stabilized nanoprisms. Photoinduced nanoprisms demonstrated adhesion, but to a lesser degree than citrate-stabilized seeded growth.

The citrate-stabilized, hydrogen peroxide mediated seeded growth method for silver nanoplate synthesis carried the additional benefit of easily tunable absorption peaks dependent on the quantity of silver ions added during the growth phase. However, as shown in Figure 4.3, the synthesis was found to lack reproducibility and stability.

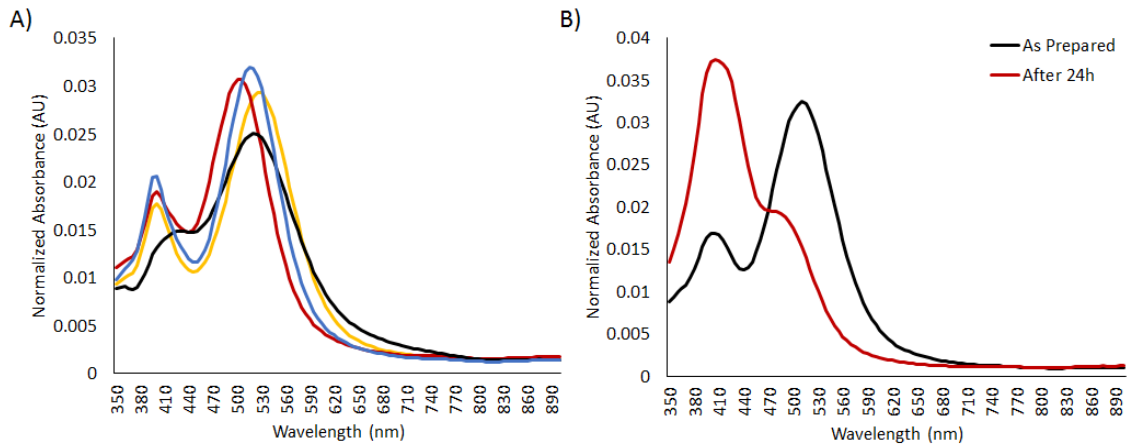


**Figure 4.3.** A) Optical extinction spectra, normalized to an AUC of 1, of repeated preparations of silver nanoprisms using the seeded growth protocol found in Li, et al. While absorbance peaks were similar in all preparations, the results were inconsistent. B) Change in absorbance spectra after 24 hours for nanoprisms prepared using the seeded growth technique.

#### 4.4.2 Optimization of Silver Nanoprism Synthesis

To address the lack of stability and the reproducibility of the citrate-stabilized nanoprism synthesis, a thorough investigation of the technique was performed examining all reagents and synthetic conditions. The two-step synthesis used as a starting point is commonly used in peroxide-etchant based techniques where a seed stock is first prepared using silver nitrate ( $\text{AgNO}_3$ ), hydrogen peroxide ( $\text{H}_2\text{O}_2$ ), trisodium citrate (TSC) and sodium borohydride ( $\text{NaBH}_4$ ) as a reducing agent. The seeds are aged overnight, diluted in  $\text{diH}_2\text{O}$  followed by addition of L-ascorbic acid (AA) prior to prism growth with dropwise addition of  $\text{AgNO}_3$ . In order to determine the contributions of each reagent, they were assayed individually while all other parameters were held constant at the values shown in Fig. 4.4.

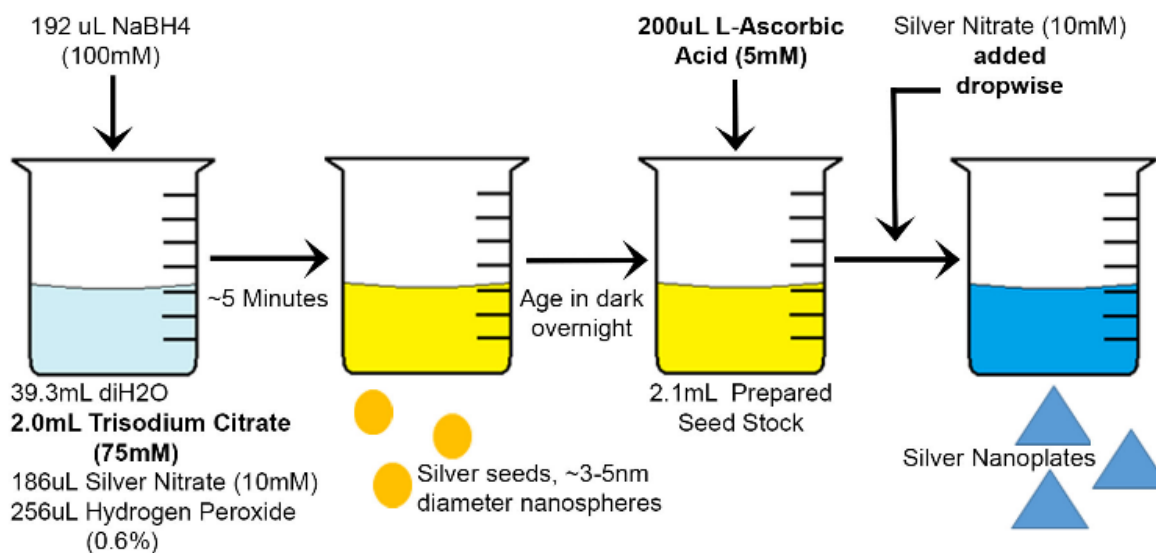


**Figure 4.4.** Reaction schematic of optimized citrate-stabilized nanoprism synthesis using hydrogen peroxide etching. All listed reaction components were evaluated here, those found to have significant effects on nanoprism stability and reproducibility are highlighted in bold.

First, L-ascorbic acid (AA) was evaluated - the reducing agent used in the growth stage of the prisms. It has been reported that the presence of hydrogen peroxide prevents  $\text{NaBH}_4$  from interfering with prism growth, eliminating the need for overnight aging.[10a] Therefore, we evaluated synthesis with fresh and aged-overnight seed solutions. As shown in Figs. 4.5A and 4.5B, AA concentration above  $\sim 0.1\text{mM}$  was required for prism growth to occur, but relatively minute spectral changes were observed above this concentration. However, after 24 hours, samples with high AA concentration ( $>6\text{mM}$ ) demonstrated significant change in UV-Vis spectrum shape that was especially pronounced in the case of fresh seeds (Fig. 4.5C), indicating a lack of stability. This spectral change was quantified using the formula  $Instability = I_{init} \oplus I_{24h} / I_{init} \cap I_{24h}$  where the disagreement ( $\oplus$ ) between initial ( $I_{init}$ ) and 24h ( $I_{24h}$ ) spectra was divided by their agreement ( $\cap$ ); this measure was used as an indicator of stability throughout our study (details in Supporting Information). Scores below 0.15 were considered stable because they correlated with small spectral changes as shown in examples in Fig 4.5 (C and D, blue spectra). AA concentrations ranging from 0.435 to 1.74 mM resulted in the most stable nanoprisms, with optimal results at 0.435 mM. As shown in Fig. 4.5E, stability at high AA concentrations was markedly increased in samples prepared using aged seeds, though this effect proved negligible with reduced AA concentrations. These results show that the secondary reducing agent is required for nanoplate synthesis, but its excess reduces stability of nanoparticles. This effect is likely associated with nanoparticle degradation in solution due to excess of the reducing agent. Further experiments in this study were performed using aged seeds as they demonstrated overall better stability in a broad range of AA concentrations.

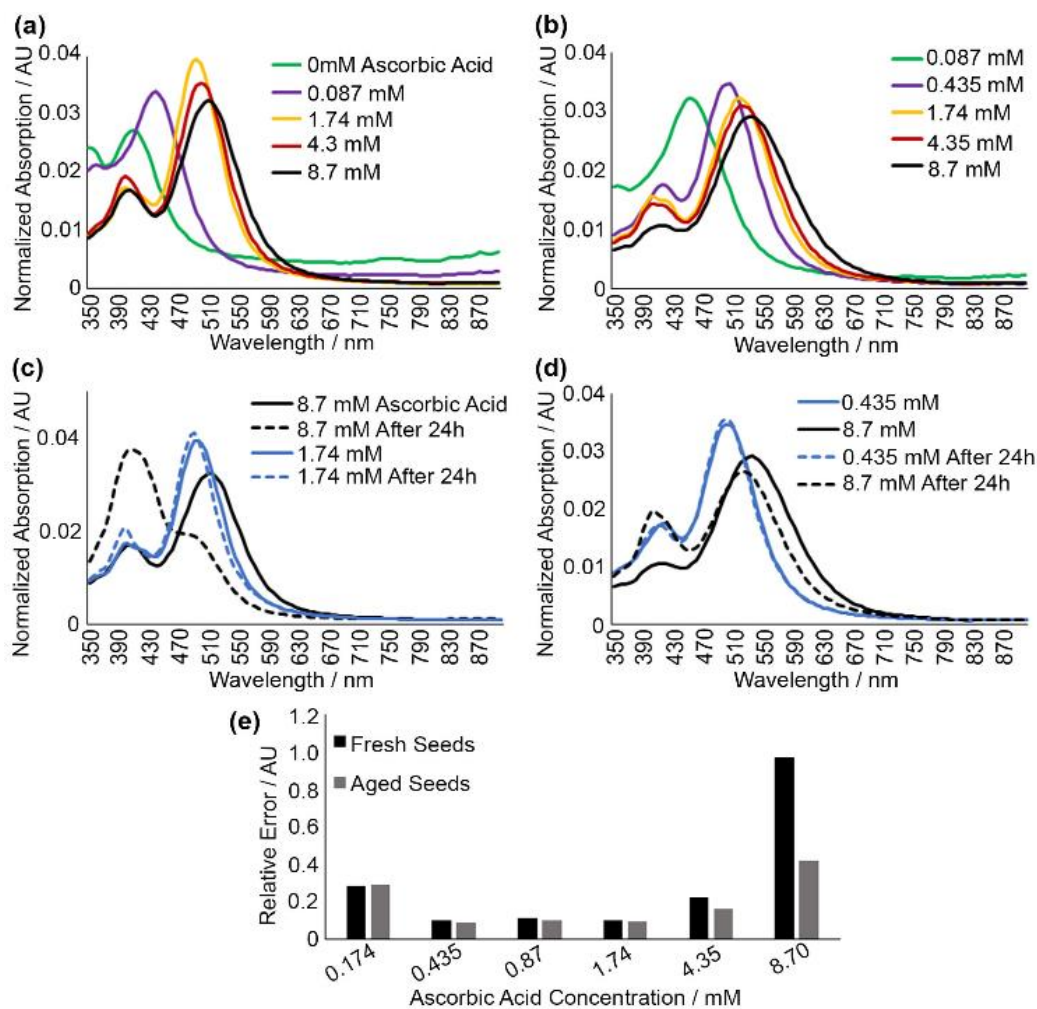


**Figure 4.5.** (A) Spectra demonstrating effects of varying ascorbic acid during nanoprism synthesis with fresh seed solution. (B) Spectra demonstrating effects of varying ascorbic acid during nanoprism synthesis with aged seed solution. (C) Representative examples of unstable and stable nanoprisms prepared using fresh seeds with 8.7mM (black curves) and 1.74mM (blue curves) ascorbic acid concentration, respectively. (D) Examples of spectral changes 24h after nanoprism synthesis using aged seeds. (E) Twenty-four hour stability test for nanoprisms prepared using various concentrations of ascorbic acid with either aged or fresh seeds; note high level of stability for AA concentrations ranging from 0.435 to 1.74 mM.

Next, we studied the effects of hydrogen peroxide, which functions as an etchant, and sodium borohydride - the reducing agent responsible for initial seed production, on prism synthesis and stability. Nanoprisms with the smallest secondary peak at 400nm

resulted from seed stock with  $[H_2O_2]$  between 88 and 121  $\mu M$  (Fig. 4.6A). Neither  $H_2O_2$  nor  $NaBH_4$  demonstrated any impact on prism stability. (Figs. 4.6B and D).

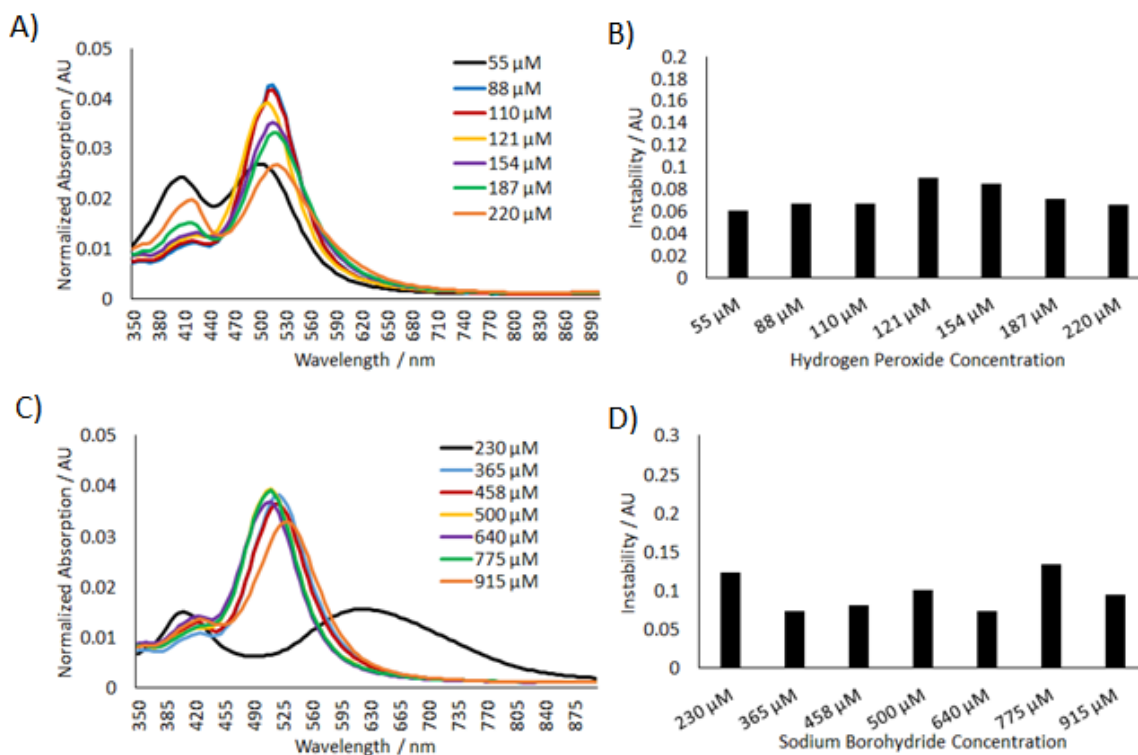


**Figure 4.6.** A) and B) Effect of hydrogen peroxide on nanoprism spectra (A) and stability (B). Ideal nanoprism growth (sharper peaks and reduced 400nm secondary peak) was found to occur with  $H_2O_2$  concentrations ranging from 88 - 121  $\mu M$  in the seed stock preparation. No effect on stability was observed. C) and D) Effect of sodium borohydride on absorption spectra (C) and stability of nanoprisms (D).  $NaBH_4$  concentrations above  $\sim 250 \mu M$  were required for ideal nanoprism growth. No effect on stability was observed.

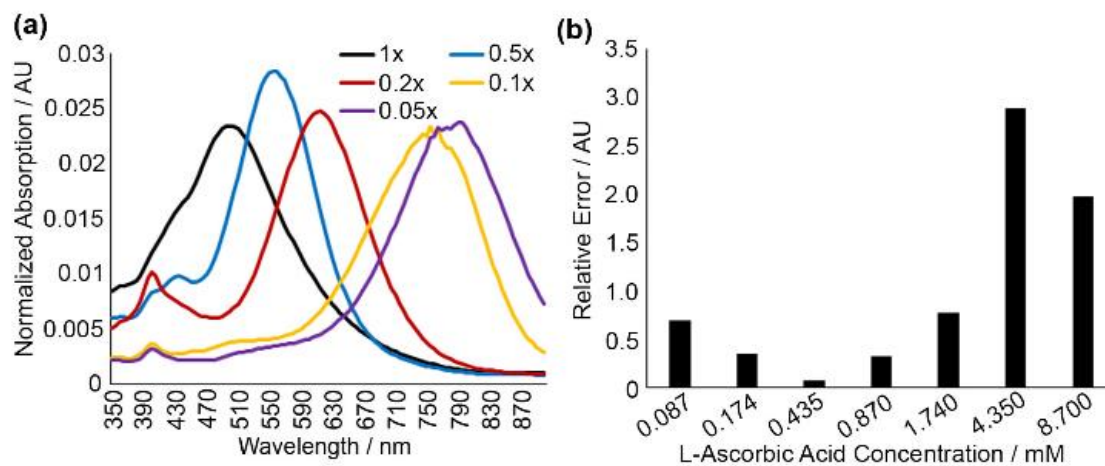


**Figure 4.7.** (A) Absorbance spectra demonstrating effects of seed dilution on nanoprism growth with seed concentrations 1x, 0.5x, 0.2x, 0.1x and 0.05x of the initially prepared seed stock. All experiments were performed with dropwise addition of 100 $\mu$ L of silver nitrate. (B) Twenty-four hour change in spectral shape for varying concentrations of ascorbic acid in nanoprisms prepared from 0.1x seed solution.

It was observed that during the prism growth stage, further addition of silver nitrate beyond one-tenth of the initial reaction volume did not result in further growth, preventing synthesis of larger prisms. In order to address this limitation, the effect of seed concentration was evaluated in the context of increasing nanoprism size. As shown in Fig. 4.7A, reducing seed stock concentration resulted in synthesis of larger nanoprisms with absorbance peaks up to 900 nm, due to fewer seed particles incorporating the same quantity of silver nitrate. Optimal stability occurred at 0.435mM AA (Fig. 4.7B), indicating that ideal AA concentration was not variant with seed concentration. Figure 4.8 shows how silver nanoprism size varies with silver nitrate addition under different dilution conditions.

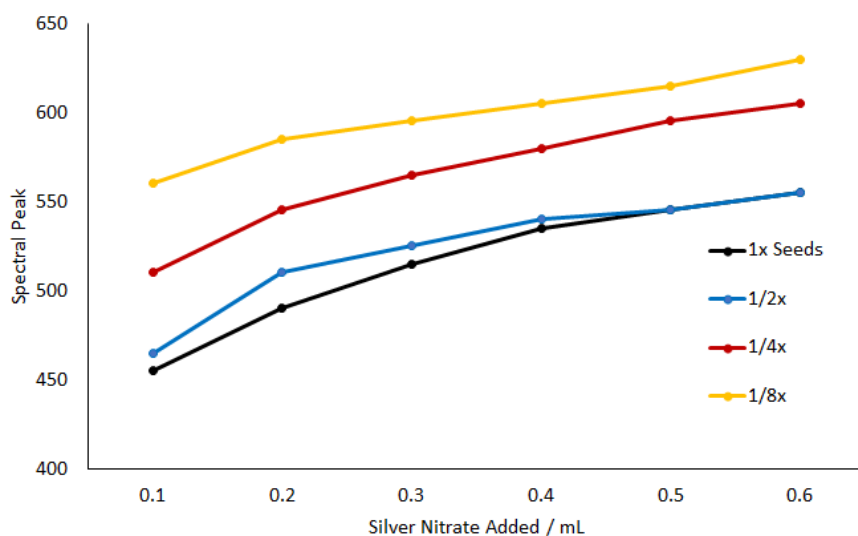


**Figure 4.8.** Absorption peak of silver nanoprisms by volume of silver nitrate added, grown from different dilutions of seed stock. All data points gathered using 10.5mL initial solution. Increased levels of dilution allow for growth of larger nanoplates with the same quantity of silver nitrate added.

Next, we analyzed the effects of trisodium citrate - a capping agent and stabilizer (Fig. 4.9). For small prism sizes with less than ~35 nm edge length, varying the trisodium citrate concentration resulted in little difference in UV-Vis spectra (Fig. 4.9A). For larger prisms, the peaks broadened significantly at lower concentrations of sodium citrate (Fig. 4.9B). Sodium citrate is known to act as a surface stabilization element, binding to the facets and preventing the addition of silver ions thus halting nanoparticle growth [7a]. Therefore, we hypothesized that higher concentrations of sodium citrate are required to achieve consistent synthesis of larger nanoprisms.



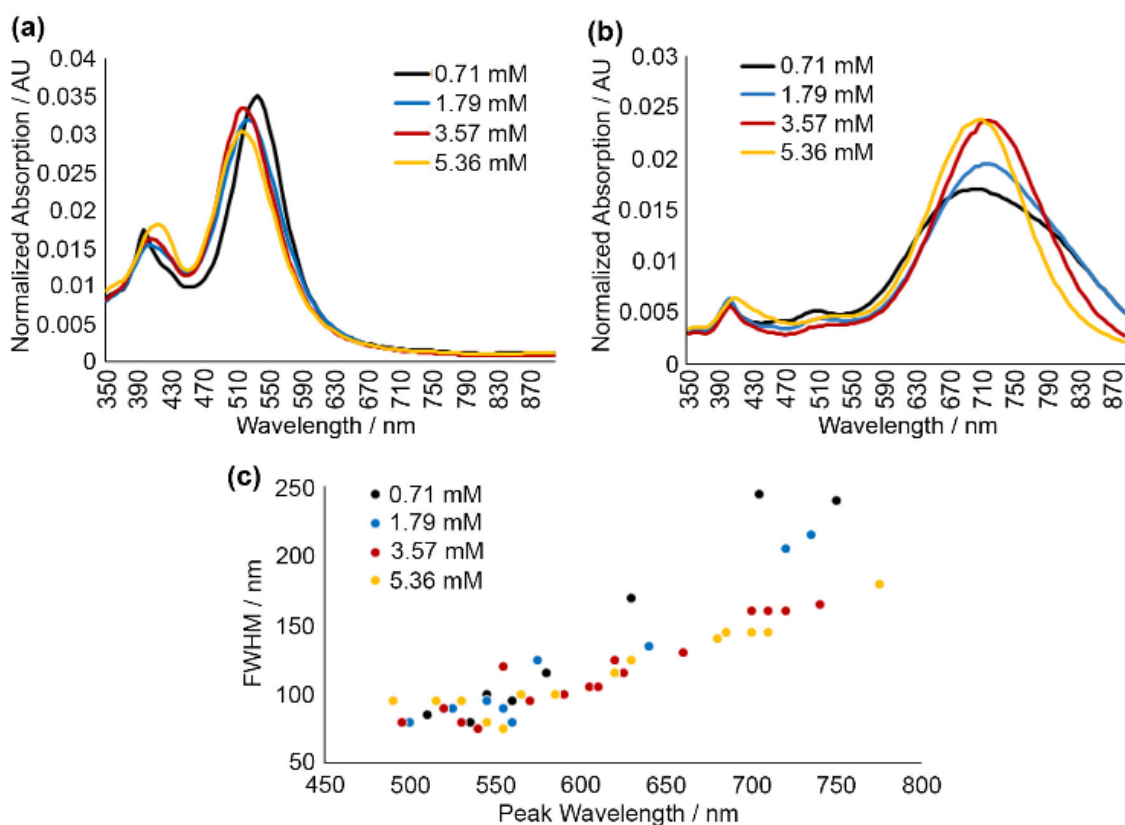


**Figure 4.9.** (A) Absorbance spectra of small nanoprisms ( $\sim 30\text{nm}$  edge length) prepared from aged seed solution with varied concentration of tri-sodium citrate (TSC). Reactions proceed more rapidly with lower TSC concentration, but optical properties remain similar. (B) Spectra of larger nanoprisms ( $\sim 100\text{nm}$  edge length) prepared from seed solution with varied concentration of sodium citrate. Note a significant widening of plasmonic peaks at lower citrate concentrations. (C) Scatter plot of full-width at half-maximum (FWHM) as a function of nanoprism absorption peak wavelength for varied concentrations of sodium citrate; note a relative increase in FWHM for larger nanoprisms at lower concentrations of sodium citrate.

To verify this, nanoprisms were synthesized with concentrations of sodium citrate ranging from 0.71 to 5.36mM. For each concentration, nanoparticles were grown to various sizes by changing the quantity of silver nitrate added, with absorbance peaks ranging from 450nm to 780nm. Then peak full-width at half-maximum (FWHM) was used as an indicator of nanoprism dispersity (Fig. 4.9C). The narrowest FWHM of  $\sim 80\text{nm}$  occurred

for smaller nanoplates (~20nm edge length) for all concentration of sodium citrate. However, FWHM increased faster with prism size for lower sodium citrate concentrations, indicating higher variation in particle morphologies.

Finally, the effect of rate of silver nitrate addition during prism growth was analyzed. Silver nitrate was added continuously to seed stock solution using an automated syringe pump at flow rates ranging from 15 – 400 $\mu$ L/min. Three seed stock formulations were used – 3.57mM TSC (base reaction condition, Fig. 4.4), 0.71mM TSC (reduced citrate) and  $\frac{1}{2}$  seed stock concentration (reduced concentration for larger prism growth). Slower rate of silver nitrate addition was better under all reaction conditions tested; this was evident from a reduced secondary peak at 400nm and red-shifted spectra indicating increased silver incorporation, and thus larger prisms, as well as better control of nanoplate morphology (Fig. 4.10). Little improvement in nanoprism quality was observed below the speed of *ca.* 50  $\mu$ L/min at all conditions tested. We found that flow rate had very little effect on the stability of prisms, as Instability values were consistently below 0.15. (Fig. 4.10D).

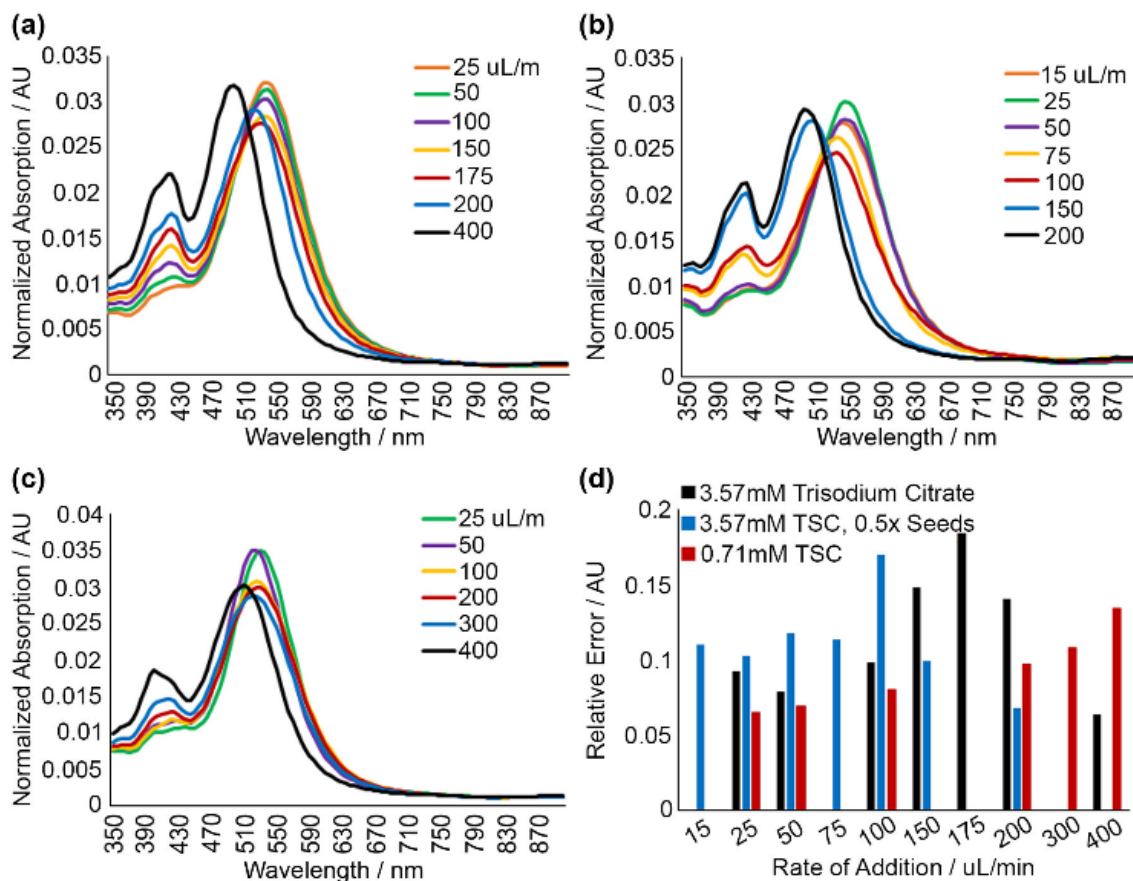


**Figure 4.10.** Absorbance spectra demonstrating effects of varying rate of silver nitrate addition in the case of: (A) 3.57mM TSC seed solution; (B) 3.57mM TSC seed solution diluted 1:1 with diH<sub>2</sub>O prior to prism growth; and (C) 0.71mM TSC seed solution. (D) Relative spectral changes after 24h storage demonstrating stability of nanoprisms at reaction conditions tested.

Using the optimized parameters from our experiments, we developed a finalized protocol for synthesis of stable silver nanoprisms in a wide range of sizes (Fig. 4.11). The nanoprisms exhibit plasmon resonance peaks covering the whole visible and near-infrared (NIR) spectral region (Fig. 4.14, A-B).

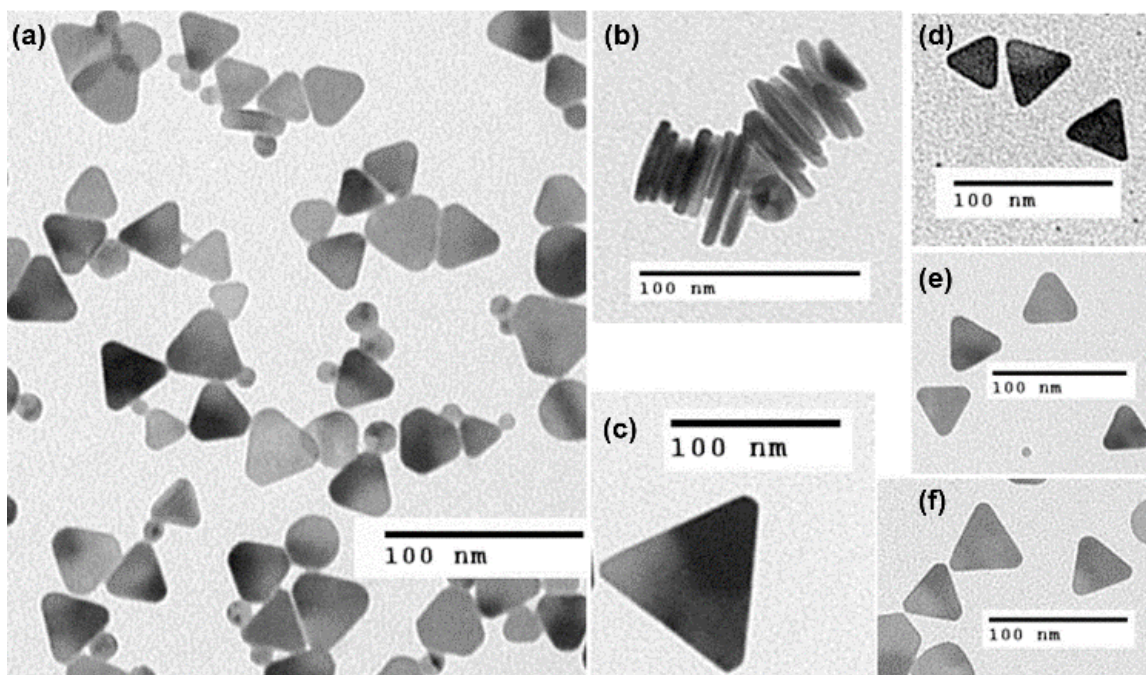


**Figure 4.11.** (A) Representative TEM image of silver nanoplates prepared using the synthesis presented here. Morphology of the prisms is consistent with those reported in literature. (B) TEM showing stacked nanoplates; the plate thickness is *ca.* 7 nm. (C-F) Representative TEM images showing nanoplates with sizes 105nm (C), 40nm (D), 45nm (E), 50nm (F)

Pursuant to our results that nanoplates synthesized from fresh seeds are stable in reactions with low ascorbic acid concentrations, we demonstrated a one-pot variant of the optimized protocol described here for synthesis of stable nanoplates (Fig. 4.12). In this variant, seed solution is prepared as previously described, however, it is then utilized for prism growth without aging. Additionally, we found that the protocol is fully scalable in synthesis volumes ranging from 2.3 to 46 mL prior to addition of silver nitrate (Fig. 4.13).

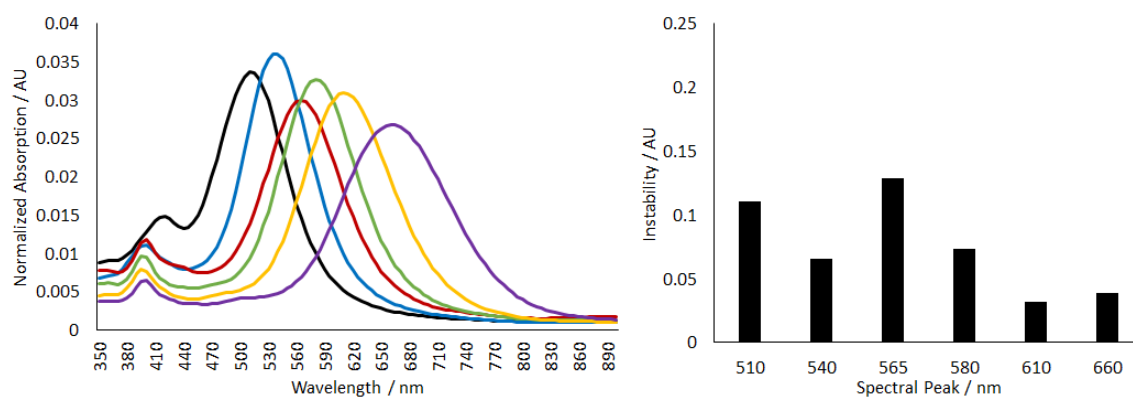


**Figure 4.12.** Demonstration of one-pot synthesis of silver nanoprisms using freshly prepared seed solution and low ascorbic acid concentration (0.435mM). At this concentration of ascorbic acid, fresh seed stock showed no loss in stability compared to aged seed stock, allowing for one-pot synthesis.

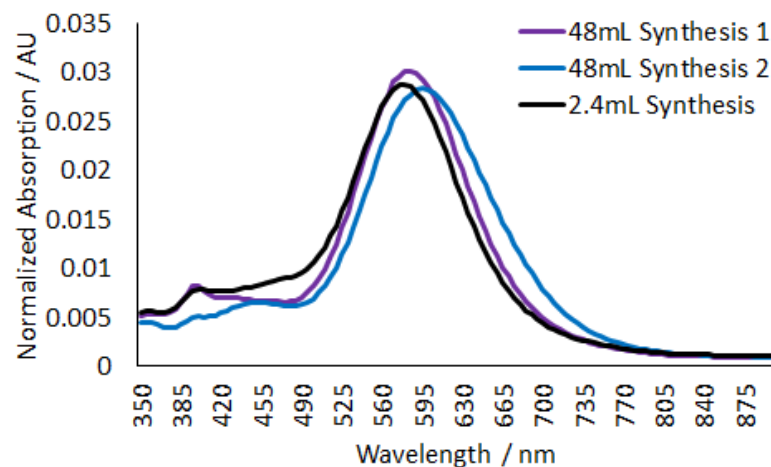


**Figure 4.13.** Comparative absorption spectra of nanoplates using larger synthesis volume. No differences were observed between nanoplate solutions using low volume and high volume syntheses. Volumes larger than 48mL were not tested.

#### 4.4.3 Functionalization and Adhesion of Nanoprisms

In order to verify that the prisms prepared using this protocol can be used for a simple surface functionalization using thiol chemistry, we attached the nanoprisms to a

glass slide coated with (3-mercaptopropyl)trimethoxysilane (MPTMS) (Fig. 4.14C). The nanoprisms formed a uniform dense layer on the thiol-modified glass slide while none adhered to untreated slides.

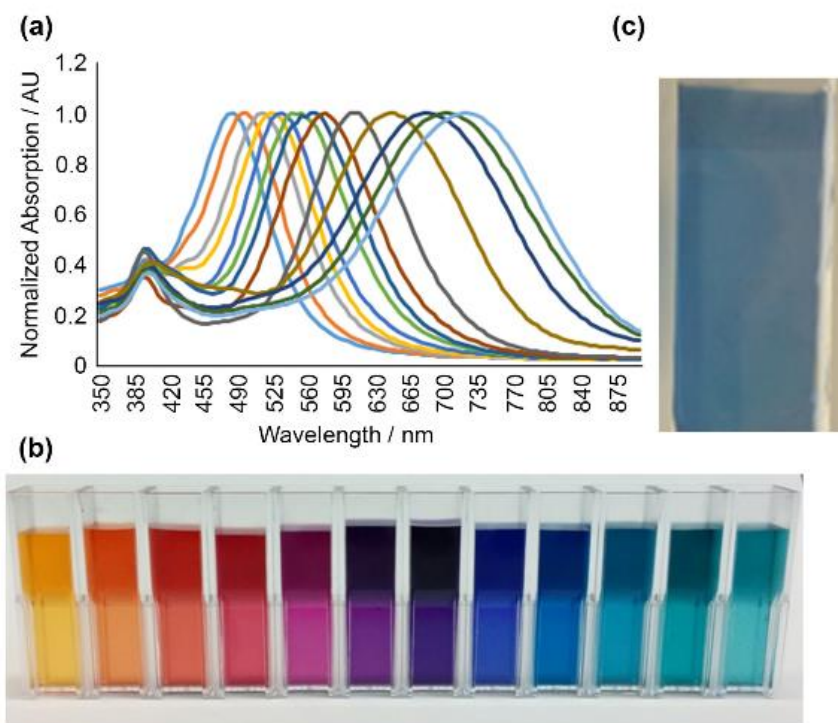


**Figure 4.14.** (A) Absorption spectra, normalized to a peak absorbance of one, for a subset of nanoprism sizes obtained. (B) Nanoprisms in water demonstrating the range of achievable particle colors. (C) Slide coated with  $\sim 50$ nm edge length nanoprisms using thiol modification of the glass surface.

While (3-mercaptopropyl)trimethoxysilane treatment has long been used as a standard for thiol-coating of glass substrates for binding to silver or gold nanoparticles[274], the requirement for careful hydroxylation and silanization prior to adhesion of nanoparticles resulted in a far more complex process than the usage of simple

physisorption of poly-L-lysine, which resulted in similarly consistent nanoparticle monolayers. MPTMS-mediated thiol modification of glass substrates proved to be unreliable compared to PLL, the increased complexity of the reaction resulted in failed monolayers with no adhesion far more often, while PLL proved strongly reliable and did not interfere with probe binding. It was decided to further assay PLL-mediated monolayers to verify they could be used for the LSPR chip.

In order to be usable in the LSPR chip, the nanoprism monolayer needed to be stable under all conditions that the chip would operate under. As shown in Figure 4.15, PLL mediated monolayers maintained integrity under one hour of piezoelectric pumping using the same conditions as would be used in the PCR chip (Fig. 4.15B), as well as heating to 95C for 30 minutes in a microchannel filled with deionized water (Fig.4.15A). As a result of these experiments, PLL was used to immobilize nanoprisms on glass substrates for all further experiments.

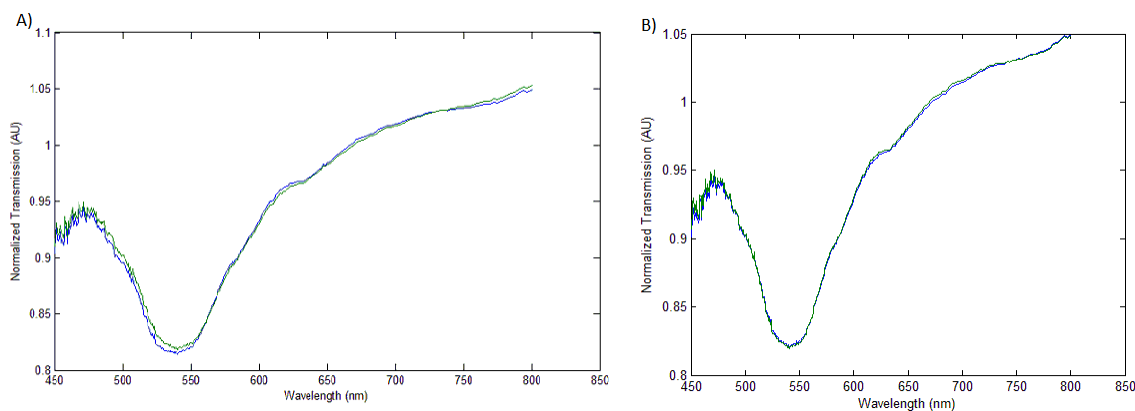


**Figure 4.15.** A) Heating stability test. Hyperspectral results showing comparative spectra before and after heating at 95C for 30 minutes in a flow channel. B) Hyperspectral results showing comparative spectra before and after one hour under piezoelectric pumping at 70V and 110Hz. Neither showed any significant spectra changes, indicating stability under PCR reaction conditions.

#### 4.4.4 Development of Optical LSPRi System

In order to perform LSPR imaging in a microfluidic system, it was necessary to construct an optical system capable of detecting small changes in the absorption spectra of the nanoprisms making up the array. In order to allow for point-of-care diagnostics, this optical system needed to be self-contained, with a relatively small footprint and low power requirements and the ability to take a 2D image. To this end, an optical system based on the use of diffraction and a digital micromirror device (DMD) to fraction out the light into spectral components was utilized in lieu of a dedicated spectrophotometer. The operating principle of the imaging system was to take white light, collimate it through a diffraction grating to break it down into spectral components, focus the separated spectrum onto a DMD, which could then be used to isolate frequency bands and pass them on to an optical fiber, which would collect the output light into a collimator to create a beam incident on the detection zone and into a CCD camera. Figure 4.16 shows a diagram of the optical pathway.

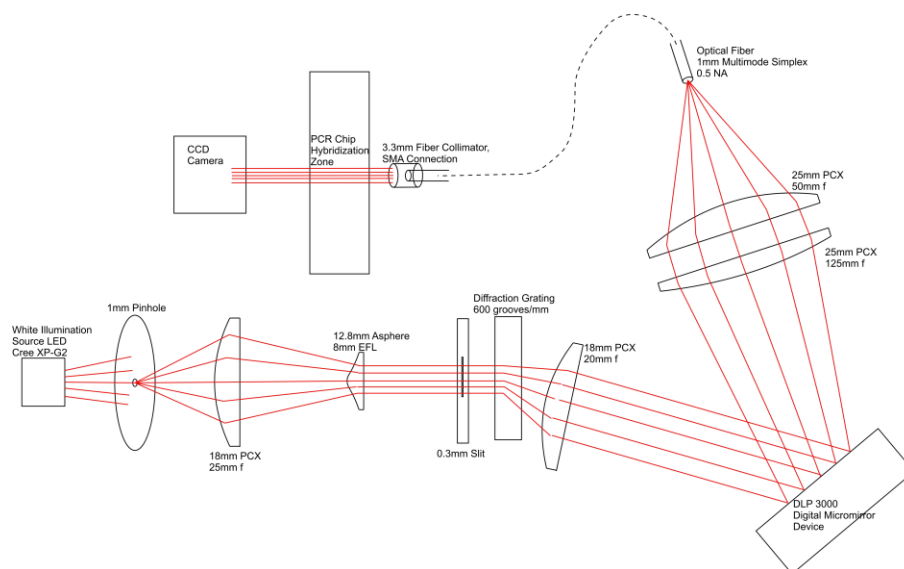


**Figure 4.16.** Planned optical pathway for localized surface plasmon resonance imaging utilizing a digital micromirror device to separate diffracted light for spectral resolution.



The primary components involved in the optimization of luminous flux and spectra resolution for the optical system consisted of the light source, diffraction method, frequency selection at the DMD, and the optical fiber output and collimation. For illumination, white light sources commonly used in microscopy, halogen, xenon and LED sources, were considered. Figure 4.17 shows representative spectral output of each of these options.

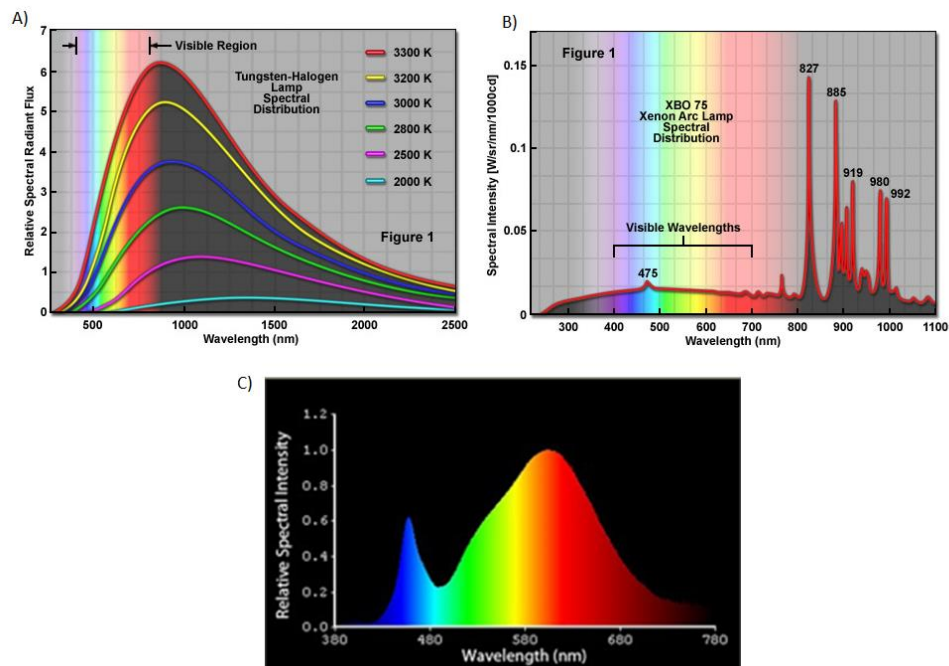


**Figure 4.17.** Typical spectral output of A) halogen lamp (image credit to Zeiss), B) xenon lamp (image credit to Zeiss), C) CREE XP-G2 warm white LED (image credit to RapidLED)

All three provide strong illumination in the 550-700nm range that was ideal for measuring spectral shifts in nanoprisms with a 600nm absorption peak. Halogen and xenon lamps also showed a significant contribution in the near-infrared spectrum, which can

result in significant heat generation in the optical pathway. With a long imaging time and a system already under heating from PCR, extra heat input could prove problematic, so LED illumination was chosen to avoid these heating effects. The CREE XP-G2 warm white LED (RapidLED, Burlingame, CA) was selected for its ideal spectral output (Fig. 4.17C) and high optical flux.

The diffraction system and frequency separation at the DMD were the primary sources of both spectral resolution and loss of optical flux, meaning that these needed to be carefully balanced to achieve maximal resolution without losing signal. Due to the fact that spectral resolution depended on spatial resolution of the diffracted light incident on the DMD, only a portion of the visible spectrum (from approximately 550-680nm) was focused onto the DMD in order to maximize resolution in the region around the absorption peak of the nanoparticles. To verify the selected spectral range, a glass cover slip was coated with a monolayer of nanoprisms with a 600nm absorption peak and placed in the path of spatially separated light reflected from the DMD (Fig. 4.18). A CCD camera (Hamamatsu) was used to collect the light transmitted through the nanoparticle monolayer. The transmitted light spectra were converted to absorption spectra by normalizing by measurements taken through a clean glass cover slip. As shown in Figure 4.18C, the resultant spectrum matched to the expected spectrum from colloidal UV-Vis measurements as well as hyperspectral measurements taken of the same cover slip. The hyperspectral measurements were used to match the exact spectral range measured by the optical system, resulting in a range of 450-650nm.

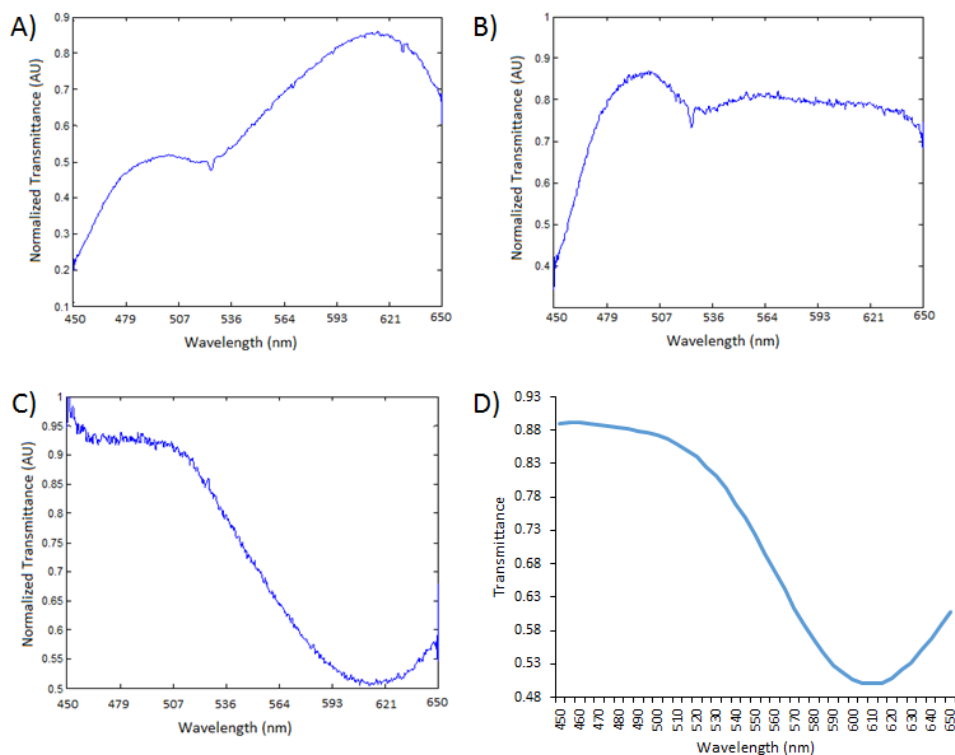


**Figure 4.18.** A) Normalized transmitted spectrum as measured from spatially resolved spectral illumination through a clean glass coverslip. B) Normalized transmittance through a glass coverslip coated with a monolayer of nanoprisms with a 600nm absorbance peak. C) Transmittance through nanoprism monolayer normalized by the measured spectral transmittance through the blank slide. Note that the spectrum matches well to D) Transmittance of colloidal nanoprisms from 450-650nm with an absorbance peak at 600nm as measured using UV-Vis spectroscopy.

In order to improve spectral resolution, the imaging band was narrowed, after which, to further characterize and optimize the spectral resolution of the detection system, images were taken of the spectra resulting from passing the diffracted light through a series of bandpass filters with known spectral throughput – XF3084535AF45 (535nm center, 45nm FWHM), XF1021550DF30 (550nm center, 30nm FWHM), XF1045560DF15 (560nm center, 15nm FWHM), QMAX/EX620-650/25 (620-650nm band), and XF3059QBEM90168 (580-615nm band) (Horiba, Alvin, TX). The obtained images were then correlated to the known spectral bands to determine edge locations and compared to

the calculated edge location assuming perfect spectral resolution. As shown in Figure 4.19A, there was a significant mismatch observed. To reduce this effect, the width of the slit was reduced to 0.5mm and 0.3mm and the same experiment performed. Figure 4.19A also shows the resulting spectral resolution values. Below 0.3mm, the optical flux of the system was deemed too low for effective measurements, so the slit was set to 0.3mm for the remainder of experiments (Fig 4.19B).

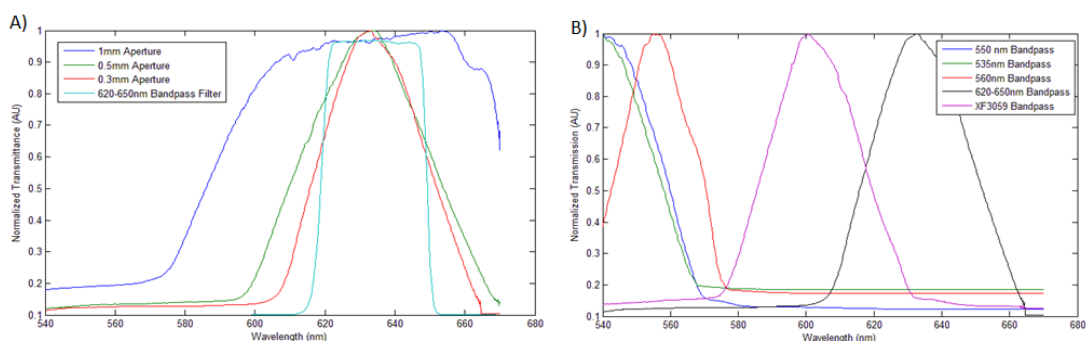


**Figure 4.19.** A) Spatially separated transmission through a 620-650nm bandpass filter using 1mm, 0.5mm and 0.3mm aperture sizes prior to the diffraction grating as compared to actual transmission through the filter. The 0.3mm aperture had a full-width half-maximum from 615-652nm, very close to the theoretical 620-650nm. B) Spatially separated transmission through a series of bandpass filters with a 0.3mm aperture prior to the diffraction grating. Using these values, the spatial separation on the DMD was matched to spectral output, giving a range of 540 to 680nm.

#### 4.4.5 Verification of Optical LSPR Imaging

Once the LSPR optical detection system was finalized, the system was verified by measuring the absorption spectrum of nanoprisms monolayers adhered to glass cover slips. Silver nanoprisms with an absorbance peak at 555nm were utilized and adhered to the substrate. The cover slip was then measured, along with a blank cover slip, on both the LSPR imaging system and hyperspectral. The optical detection system was then used to measure spectral shift in a nanoprism monolayer under different conditions. A layer of dry film adhesive was applied to the cover slip leaving open quadrants. Droplets of solvents –

deionized water (dielectric constant of 88) and glycerol (dielectric constant of 42.5) were placed in the quadrants as indicative of likely shift sizes and pressed down with a clean glass cover slip. Measurements were then taken using the LSPR imaging system and hyperspectral microscopy. The LSPR imaging measurements, taken using the Reitiga EXi camera with 250ms integration time, demonstrated a shift of  $\sim 15\text{nm}$  between dry and water-coated particles, and  $\sim 20\text{nm}$  between water and glycerol coated particles. These results agreed with the hyperspectral measurements. For calculations directly from measured transmission, avoiding the need for normalization by illumination spectra, an average measured shift of 2.6% in measured transmission was observed to correspond to the 20nm shift, indicating an upper bound of expected signal during DNA hybridization experiments.

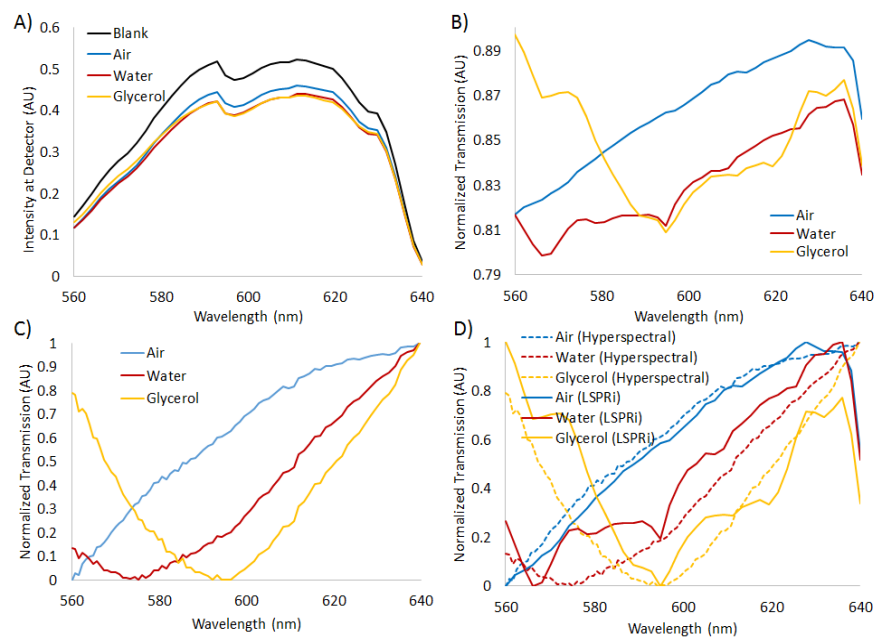


**Figure 4.20.** A) Raw transmission collected by Reitiga EXi camera for LSPR imaging of blank cover slip, dry nanoprism monolayer (colloidal absorbance peak at 555nm), nanoprisms coated in deionized water and nanoprisms coated in glycerol. B) Transmission for nanoprism monolayers normalized by light source spectral output as measured through

blank cover slip. C) Hyperspectral measurements for dry nanoprism monolayer and monolayers coated with deionized water or glycerol. D) Comparison of hyperspectral and LSPRi system measurements of dry nanoprism monolayer, water-coated and glycerol-coated monolayer over the region from 560-640nm. Note strong similarity between curves.

## 4.5 DISCUSSION

Noble metal nanoparticle based detection regimes such as SERS and SPR boast impressive sensitivity to small changes in local dielectric constant such as those resulting from surface binding of biomolecules. They also carry the added benefits of being label-free and applicable to a wide variety potential assays as long as an appropriate thiol-linked probe can be synthesized (DNA hybridization probes, antibodies, etc). In particular, localized surface plasmon resonance using nanoprisms with high anisotropy for strong shifts in absorption spectrum with dielectric changes leads to potential for colorimetric sensors and spatially resolved imaging techniques for multiplex analysis.

As the sensitivity of an LSPR imaging system is highly dependent on the properties of the nanoparticles used to form a monolayer on the detection array substrate, multiple silver nanoprism synthesis techniques were assayed for optical properties and functionalizability. Further, the various components of citrate-stabilized chemical synthesis of silver nanoplates using hydrogen peroxide were systematically tested. Greatly increased stability of nanoprisms was demonstrated by controlling ascorbic acid concentration, allowing for stable one-pot synthesis. Additionally, tight control of nanoprism synthesis was achieved through optimization of seed stock dilution, citrate concentration and rate of silver nitrate addition. Using the optimized parameters of the reaction, a scalable, refined protocol for growth of silver nanoprisms was developed with fully tunable plasmon resonances across the visual spectrum and into the near infrared. These particles were shown to be viable for surface functionalization in biosensor

applications using thiol chemistry. In addition, nanoprism monolayers were tested for viability under the heating and flow conditions in the fluidic system presented in the previous chapter.

An optical imaging system was developed using diffracted white light from an LED incident on a digital micromirror device to allow for two-dimensional, time resolved spectral imaging and measure shift over time in absorption spectra of nanoparticles adsorbed on a glass substrate. This system was optimized for luminous flux and characterized, with a final spectral resolution of 2nm measured in 40 points across the range from 560-640nm. The resulting LSPR imaging system was utilized to measure spectra of nanoprisms under multiple solvent conditions to determine expected levels of optical shift for DNA hybridization. A shift of approximately 20nm was observed between water (dielectric constant of 88) and glycerol (dielectric constant of 42.5), similar to that expected between prisms functionalized with probes and DNA hybridization. For detection purposes, this resulted in a measurable direct shift in transmission of ~2.6%, which can be considered the upper end of expected signal.

#### **4.6 ACKNOWLEDGEMENTS**

The author would like to thank Kenneth Dunner for his expertise and TEM imaging of silver nanoprisms presented in this chapter, as well as directing him towards literature on the use of Poly-L-Lysine as a surface adhesion agent.

## CHAPTER 5:

# Microfluidic PCR with On-Chip LSPRi for Rapid Characterization of Bacterial Genetic Markers

### 5.1 ABSTRACT

The results from the previous two chapters were aimed at developing a rapid platform for thermocycling and an optical localized surface plasmon resonance system, respectively. While each of these systems has novelties that makes them unique, separate neither has potential for overcoming a challenge such as detection and characterization of microbial pathogens or any other rare cells. However, each method was designed to complement the other – recirculating PCR provides advantages to DNA hybridization detection, as discussed in Chapter 3, and LSPR imaging is a highly sensitive platform capable of both label-free and multiplex detection well suited to targeting DNA.

In this chapter, the two systems have been integrated and validated for successful amplification of DNA using both fluorescent measurements on gel electrophoresis and LSPR detection of optical shift. The limit of detection was observed to be  $\sim 5\text{fg}/\mu\text{L}$  of input *E. coli* DNA, or approximately 59 bacteria in a  $200\mu\text{L}$  sample. While this concentration was too low to achieve signal saturation, an observable increase above baseline noise was present. Signal saturation occurred at DNA inputs of  $50\text{fg}/\mu\text{L}$  and higher, resulting in a saturated signal of 1% shift. This shift was lower than anticipated, but the sensitivity of the LSPR imaging system was capable of resolving the difference. Further, multiplex PCR amplification and detection was demonstrated using isolates of *E. coli* *tufB* and *DXS* gene targets. Detection of DNA hybridization was consistently achieved within 15 minutes for positive samples, or about 20 cycles. This demonstrates strong potential for future work in rapid detection of resistance marker panels for bloodstream infections.



## 5.2 INTRODUCTION

When addressing the problem of rapid characterization of pathogens in bloodstream infections, a number of factors must be taken into consideration. While timeliness arises first and foremost, sensitivity and specificity must also be addressed – a rapid detection scheme that cannot discriminate between targets or detect low sample concentrations would not be viable for clinical usage without the time-limiting step of cell culture[165, 166]. The previous chapters discussed the development of some of these elements – rapid thermocycling for amplification of potentially multiplexed target genes, and highly sensitive localized surface plasmon resonance detection using low-cost optical components, neither address the ultimate problem of combined sensitivity and specificity on their own. As a result, it is necessary to consider the whole device and demonstrate functionality of LSPR imaging in the changing environment of a thermocycler, and verify both limit of detection and the ability to discriminate targets for theoretical analysis for a panel of markers.

As a culmination of the work presented in the previous chapters, this chapter describes the implementation of LSPR imaging into a microfluidic thermocycler for real-time detection of target DNA sequences following PCR amplification. The fully constructed LSPR/thermocycling chip was verified using fluorescent detection of amplicons on agarose gel to ensure successful PCR amplification. The sensitivity of the optical system to shifts in extinction spectra following DNA hybridization was analyzed and custom software was developed to maximize detection in a short time frame. In addition, the limit of detection of the completed system was measured using a concentration series of input DNA from E.coli, and potential for multiplexed analysis of

genetic target was determined with side-by-side detection of *tufB*[332] and *DXS*[333] gene targets.

## **5.3 MATERIALS AND METHODS**

### **5.3.1 Nanoprism Synthesis**

Nanoprisms were prepared using a modified form of a citrate-stabilized, hydrogen peroxide etchant based seeded growth technique. In brief, a solution was prepared consisting of 16.97mL diH<sub>2</sub>O, 1mL Trisodium Citrate (75mM), 93μL Silver Nitrate (10mM) and 128μL Hydrogen Peroxide (0.5%). 96μL Sodium Borohydride (100mM) was added under vigorous stirring until the solution turned golden yellow. The solution was allowed to age overnight prior to addition of 21mL diH<sub>2</sub>O and 2mL L-Ascorbic Acid (10mM). Approximately 1mL of Silver Nitrate (10mM) was then added dropwise at a flow rate of 100μL/min until the solution reached an absorption peak at 580nm as observed using a UV-Vis spectrometer.

### **5.3.2 Nanoprism Adhesion to Glass Substrates**

Glass cover slips were coated in nanoprisms using a two-step process. First, 24x40mm borosilicate glass cover slips were cleaned using aqua regia and washed carefully with diH<sub>2</sub>O prior to incubation in a solution of 0.01% Poly-L-Lysine (PLL) for 10 minutes. The PLL physisorbed to the glass substrate, creating a thiol-modified surface. The cover slips were then blown dry under a jet of nitrogen, rinsed in diH<sub>2</sub>O and allowed to incubate for 20 minutes in a colloidal nanoprism solution with an OD >3. Following this incubation period, the cover slips were removed from the nanoparticle solution, rinsed in diH<sub>2</sub>O and

dried under a jet of nitrogen. This technique resulted in reliable formation of consistent nanoprism monolayers for particles of all sizes. Two nanoprism sizes were used in experiments in this chapter - ~50nm edge length particles with an absorbance peak at 600nm, and ~45nm edge length particles with an absorbance peak at 555nm.

### **5.3.3 DNA Probe Bioconjugation**

Thiol-linked probes targeted to the *DXS* and *tufB* genes for *Escherichia coli* were obtained from Sigma Aldrich, (*tufB*: 5'-[Thi-C6]CGTGCGATTGACAAGCCGTTCC, *DXS*: 5'-[Thi-C6]ATCGCTGAACGCTACGCTGGTTCGATAT). A 10 $\mu$ L droplet containing DNA probes in diH<sub>2</sub>O (35 $\mu$ M) was incubated on the detection zone of a nanoprism coated coverslip for one hour. The coverslip was then washed with diH<sub>2</sub>O and dried under a nitrogen jet. The chosen probe concentration was utilized as the minimal concentration required to maximize shift in the absorption spectra of the nanoprism, as determined by experiments that will be described in more detail below.

### **5.3.4 Fabrication of PCR Chip**

Figure 5.1A shows the design scheme for the microfluidic chip. 200 $\mu$ m deep channel structures were milled out from Makrolon polycarbonate and ramped to no depth in a 4x5mm detection zone (Fig. 5.1B). Prior to use in PCR experiments, the polycarbonate chip was filled with 1mg/mL bovine serum albumin (BSA) and allowed to incubate for 30 min prior to the removal of the BSA and dried using a jet of nitrogen to create a passivation monolayer and improve wetting. The polycarbonate chip was then adhered to a nanoprism coated glass coverslip for the detection zone and 36-gauge aluminium for the heating zone

using 100 $\mu$ m layer of dry film adhesive (3M). The boundary between the two materials was sealed using dry film adhesive, followed by a small piece of cut borosilicate glass to prevent deformation under heating. A piezoelectric buzzer and PEEK tubing for input and output were also bonded to the chip. All gaps were then sealed using NOA68 UV-cured adhesive (ThorLabs).

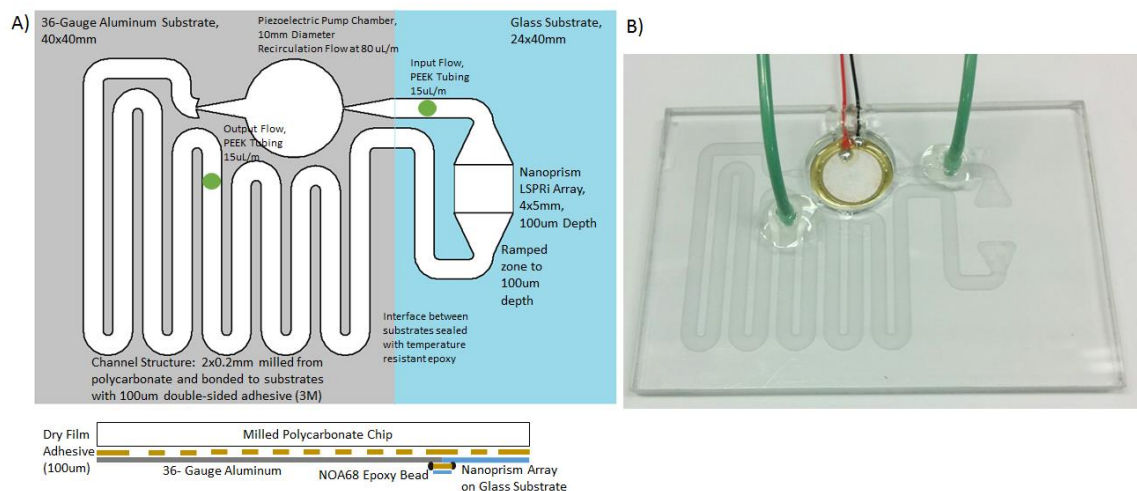


**Figure 5.1.** A) Layout and construction of combined LSPRi/Recirculating PCR chip (top), cross-section of materials used (bottom). B) Image of milled polycarbonate substrate with piezoelectric buzzer and inlets/outlets in place.

### 5.3.5 Piezoelectric Pumping

Piezoelectric pumping was accomplished using a signal generator (BioRad), 10x voltage amplifier and piezoelectric buzzer (Digikey). The piezoelectric buzzer was coated with a 100 $\mu$ m layer of dry film adhesive followed by a 16 $\mu$ m layer of aluminium to prevent inhibition of PCR by leaching of copper ions. The buzzer was then sealed into the milled polycarbonate chip as described above. The signal generator was set to 4V at 110 Hz and connected to the amplifier to achieve a pumping rate of 40 $\mu$ L/m. The output of the

amplifier was connected directly to the piezoelectric buzzer leads. Optimal parameters for pumping were determined by measuring effective flow rate under a range of voltage and frequency conditions as described in Chapter 3.

### **5.3.6 Thermocycling Control**

Heating was provided using a Thermoelectric Cooler (TEC). Power was supplied using a 24V, 4A power supply (BioTec NG 60-5). Temperature control was managed using a resistance thermal detector (RTD, Digikey) connected via wheatstone bridge assembly to an Arduino Uno microcontroller running a custom PID control program. Circuit diagram and PID program control code can be found in the appendices.

### **5.3.7 LSPRi Optical Assembly**

Localized surface plasmon imaging of hybridization detection zone was achieved using the optical system described in Chapter 4. White light was supplied using a CREE XP-G2 Warm White LED (RapidLED). Light from the LED was collimated through a narrow slit onto a diffraction grating with 600 grooves/mm (ThorLabs). The diffracted light was then incident onto a DLP3000 608x684 pixel digital micromirror device (DMD, Texas Instruments) creating a spatial resolution of wavelengths. The DMD was used to reflect specific frequency bands onto a 1mm diameter multimode optical fiber (ThorLabs), after which it was collimated into a 3.3mm diameter beam passing through the nanoprism-coated detection zone of the PCR chip and incident onto a CCD camera. Two camera systems were used for experiments in this chapter: a Hamamatsu C2400 CCD, and a Reitiga EXi (QICam). For the Hamamatsu CCD, frame grabber software was used to collect images at

30 frames per second, followed by analysis in MatLab. For the Reitiga EXi, integration time was set to 250ms and images were collected through QCapture Pro 7 software. Collected images were then converted to .avi video files for subsequent analysis in MatLab.

### 5.3.8 LSPR Imaging Data Analysis

Two image analysis techniques were utilized in the experiments in this chapter. In both cases, images were collected at each multiple wavelength points as defined by spatial separation on the DMD. Prior to running PCR, a single spectral sweep was performed from 560-640nm to generate an initial spectrum. Following this, spectra were measured over time during thermocycling. For the first analysis technique, images taken at each wavelength point were averaged to reduce noise, after which a modified form of the ‘instability’ calculation demonstrated in Chapter 4 was used to quantitatively measure change in spectral shape. In short, time-resolved spectra at each pixel were normalized by their sum, after which normalized spectra were compared to the initial spectrum using the equation:

$$I_{i,j} = \frac{2 \sum_{\lambda} |I_{i,j}^o - I_{i,j}^c|}{(2 - \sum_{\lambda} |I_{i,j}^o - I_{i,j}^c|)}$$

Where  $I^o$  was the initial spectrum and  $I^c$  was the subsequently captured spectrum. This created an image map of the change in spectral shape at each pixel.

While this technique performs well for full spectra, it proved unable to detect changes in spectral shape when only presented with half of a spectrum, as measured when scanning 560-640nm with smaller prism sizes. Spectral shifts appearing largely as simple

decrease in signal were eliminated during the normalization step. Since scanning the sloped region of the spectrum resulted in the best possible resolution, a second analysis technique was utilized. In this variant, measured spectra were compared directly, made possible by the greatly increased signal-to-noise ratio of the Reitiga EXi camera. At each pixel, the difference map value was calculated by  $I_{i,j} = \frac{|I_{i,j}^o - I_{i,j}^c|}{I_{i,j}^c}$ .

### 5.3.9 Hyperspectral Imaging

Hyperspectral imaging of silver nanoprism monolayers was accomplished using a Leica DM6000M microscope and PARISS control software. The microscope was set to brightfield transmitted light using a halogen lamp and 20x objective. PARISS control software was used to control stage movement and image acquisition. Integration time was set to maintain intensity between 180-200. Prior to taking hyperspectral measurements, a lamp spectrum was recorded by placing an uncoated glass slide on the microscope stage, appropriately setting integration time and taking 10 acquisitions of a single slice. Once the lamp spectrum was acquired, the nanoparticle coated slide was placed on the stage and the integration time was set as before. The hyperspectral image was then taken using 100 acquisitions with 5 averages.

After image acquisition, resulting data were analyzed in MatLab using custom functions. Lamp spectra were used to normalize sample spectra to obtain 2D maps of absorption spectra. These maps were then averaged to obtain the average absorption spectra of nanoplates in the imaging area between 450 and 800nm.

### 5.3.10 DNA Isolation Protocol

DNA solutions were prepared from Stb13 E.coli (ThermoFisher, Waltham, MA) transformed with the pUC19 plasmid (Sigma Aldrich, St. Louis, MO). Bacteria were grown

in an incubator at 37C for two days in LB Broth containing 100 $\mu$ M ampicillin prior to harvesting and centrifugation. The resulting bacteria were then lysed and DNA was isolated using a DNEasy Blood and Tissue Kit (Qiagen, Hilden, Germany). DNA samples were then analysed using a NanoDrop (ThermoFisher) to determine concentration and verify purity.

### **5.3.11 PCR Protocols**

The AmpliTaq Gold PCR protocol (ThermoFisher, Waltham, MA) was utilized for all experiments in this chapter. Experimental solutions consisted of 50% v/v AmpliTaq Gold PCR Master Mix (ThermoFisher), 10% v/v sense primer (5 $\mu$ M), 10% v/v anti-sense primer (5 $\mu$ M) and 30% v/v DNA solution prepared from bacterial lysate to result in final concentrations ranging from 5fg/ $\mu$ L to 50pg/ $\mu$ L. All solutions were prepared fresh just prior to thermocycling. Primers were used targeting *E. coli* *tufB* and *DXS* genes. A slight modification to the AmpliTaq Gold protocol was used to guarantee accuracy during fast cycling on the PCR chip: step times were set to 5 seconds at 96C, 6 seconds at 60C and 10 seconds at 70C. A hot-start period of 4 minutes at 95C was utilized for PCR chip experiments.

### **5.3.12 Experimental Setup**

In a typical experiment, the PCR chip was loaded with a small amount of mineral oil to coat channel edges and heated to 94C for 3 minutes to remove interfacial air bubbles. Then 200 $\mu$ L of PCR solution was loaded into the PCR chip prior to closing the microvalves. The chip was then placed on the TEC thermocycler with a thin layer of thermal paste such that the detection zone was in line with the beam from the optical assembly. The optical system was allowed to pass through one spectral sweep as described above prior to turning on the piezoelectric pumping and thermocycling control. Experiments were allowed to run for 35 cycles, or approximately 30 minutes.



## 5.4 RESULTS

### 5.4.1 DNA Probe Functionalization Kinetics

In order to maximize signal from a hybridization based LSPR system, it was first necessary to determine the ideal concentration of DNA probes to use for functionalization. Typically, this is performed by determining the lowest concentration of probes at which maximum spectral shift occurs – past an asymptotic point, further addition of probes does not result in an appreciable increase in functionalization, and thus spectral shift. To determine this, a nanoprism coated cover slip was prepared as previously described, and 10 $\mu$ L droplets containing probes for the *E. coli* DXS gene at concentrations ranging from 7 $\mu$ M to 70 $\mu$ M were placed on the surface and allowed to incubate for one hour. After this, the cover slip was washed, dried under a jet of nitrogen, and hyperspectral measurements of each functionalized region were taken, along with a reference zone that had been incubated with diH<sub>2</sub>O. Figure 5.2 shows the resulting spectra – a concentration of 35 $\mu$ M resulted in the strongest spectral shift, so this concentration was used for all further experiments.

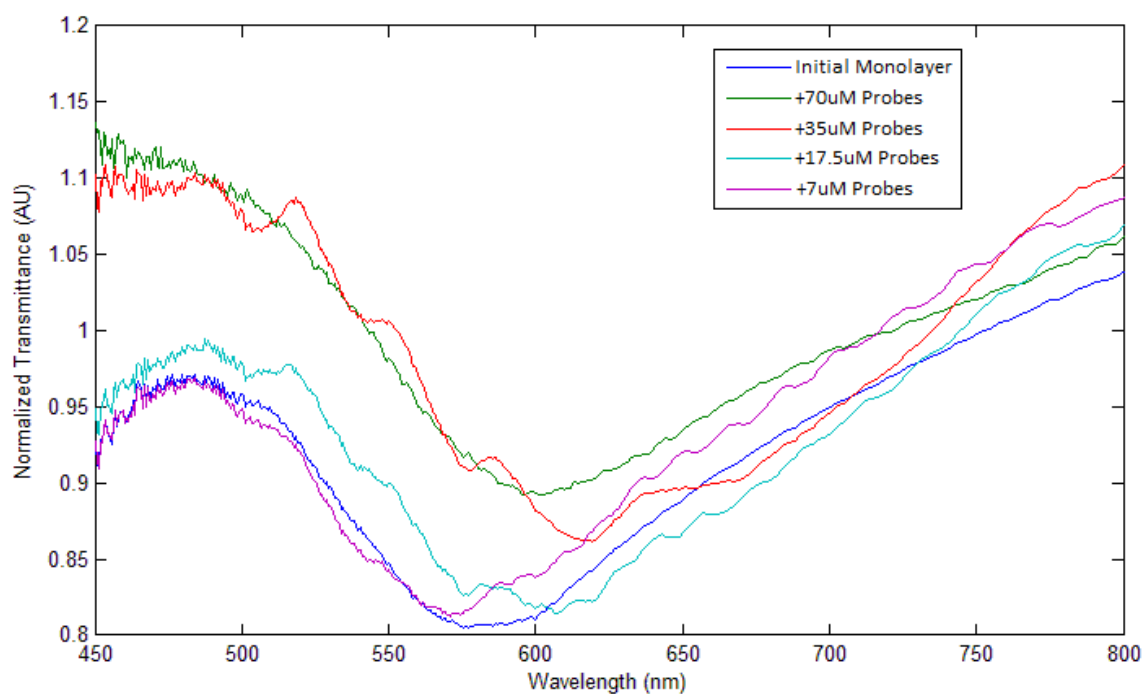


**Figure 5.2.** Observed spectral shift using hyperspectral imaging from a dry nanoprism monolayer following incubation for one hour with varying concentrations of probes for the DXS target gene. 35 $\mu$ M probes resulted in the largest spectral shift, and this concentration was used for all future experiments. Observed distortion effects in the spectra are likely due to the presence of residue dried onto the monolayer surface.

#### 5.4.2 Verification of Combined LSPRi/PCR Chip

After verification of the LSPR detection system in Chapter 4, a separate validation step was performed for the looped PCR system prior to combining elements. A PCR chip was constructed and filled as described above with primers targeting the *E. coli* DXS gene, after which it was allowed to thermocycle for 35 cycles. After PCR completion, the sample was removed from the chip, incubated for 30 minutes with 1X SYBRgreen dye and loaded on a 2% agarose gel for electrophoresis. The resulting bands were then read for fluorescence under UV illumination (Fig. 5.3). The presence of fluorescent bands in only the samples that had undergone PCR on the chip indicated that it was functional, and no PCR inhibition

was caused by the probe-modified silver nanoprisms. The nanoprism layer also remained intact, verifying earlier results on stability under thermocycling and pumping conditions.

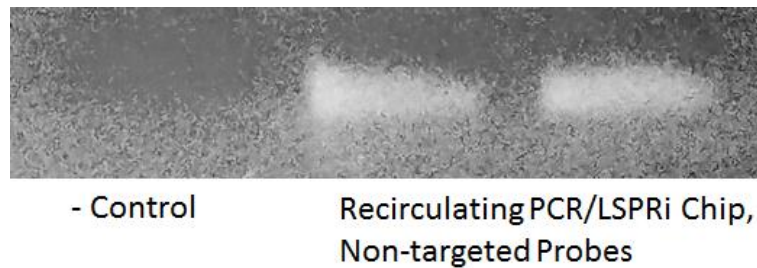


**Figure 5.3.** Gel electrophoresis results following incubation for 20m with 1x SybrGreen dye for output from Recirculating PCR/LSPRi chip. Silver nanoprisms in the detection array were functionalized with probes for the *E.coli tufB* gene rather than the *DXS* gene targeted for amplification to prevent loss of DNA output signal from hybridization.

Following validation of the ability of the fully constructed chip to successfully amplify target DNA, the next step was to demonstrate LSPR imaging detection of such an amplification. To accomplish this, the PCR chip was prepared as previously described, with a nanoprism detection zone functionalized with probes for the *E. coli DXS* gene. PCR reaction mix was prepared for this target gene and loaded into the chip, after which it was placed on the TEC thermocycler with detection zone in the path of the output beam and allowed to run for 35 cycles under constant measurement. Figure 5.4 shows a diagram of the heating cycle time, demonstrating accurate control of temperature across the experiment, though some minor oscillation effects were seen in the hot-start step. This was likely due to damage to the TEC following an electrical short, which resulted in reduced heating potential that the control program did not account for.

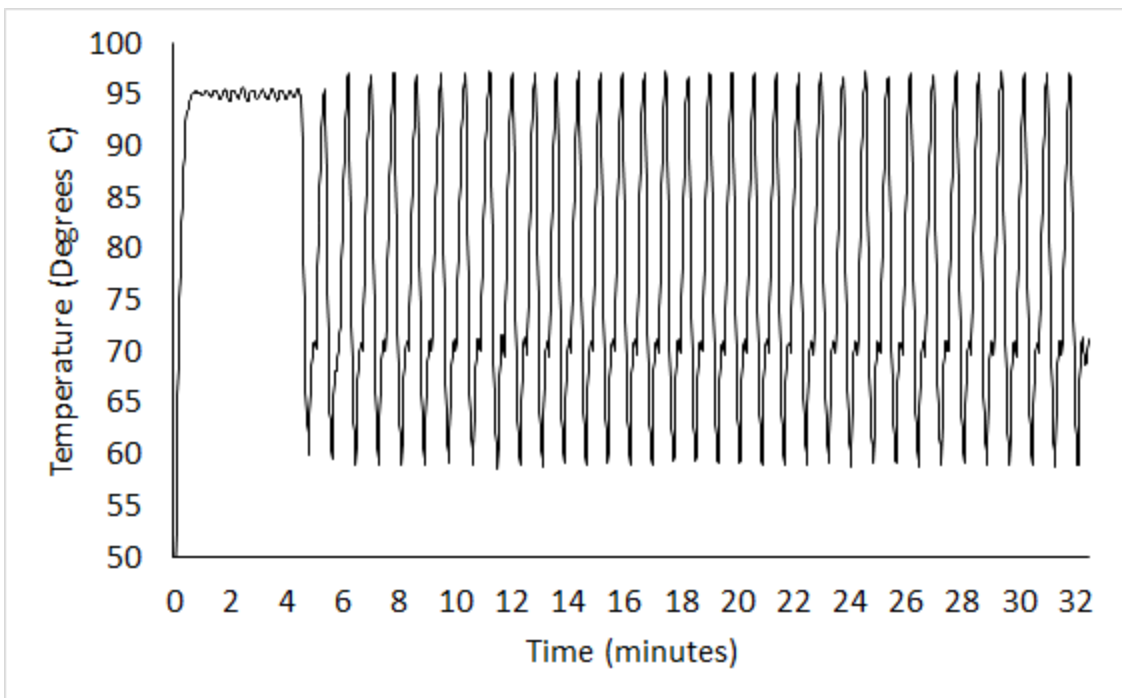


**Figure 5.4.** Thermocycling cycle diagram demonstrating measured temperature over time over the course of a typical PCR experiment consisting of 35 cycles. Oscillation present in the hot-start step is due to change in heating rate parameters resulting from minor damage to the thermoelectric cooler unaccounted for in PID calculations.

Following data collection, images were collated and analyzed in MatLab using method 1 as described in the Materials and Methods section. Figure 5.5A shows the resulting spectral shift after normalization by the spectral output of the light source – the signal was very noisy, particularly on the blue-end of the spectrum (~540-560nm), where luminous flux from the optical system was very low (<30% of maximum flux). The characteristic shape still roughly matched to the expected spectral shift curve (Fig. 5.5B), calculated from a simulated 5nm shift in colloidal UV-Vis spectra of nanoprisms of the same size. Following pixel-by-pixel calculation of change in spectral shape as described above, the heat map in Figure 5.5C was acquired. Large spectral shifts were obtained from the hybridization region (Spectral Change > 0.3), though only near the center where

illumination was brightest. Overall, the signal was very noisy, and artifacts were observed that could obscure results. In order to reduce these effects, the measured spectrum was reduced to 560-640nm, removing portions of the spectrum with low optical flux. The Hamamatsu CCD was replaced with a Reitiga EXi camera with integration functionality and the DMD program was modified to double the resolution across the remaining spectrum, down to 2nm, as the loss in optical flux would be accounted for by integration time.

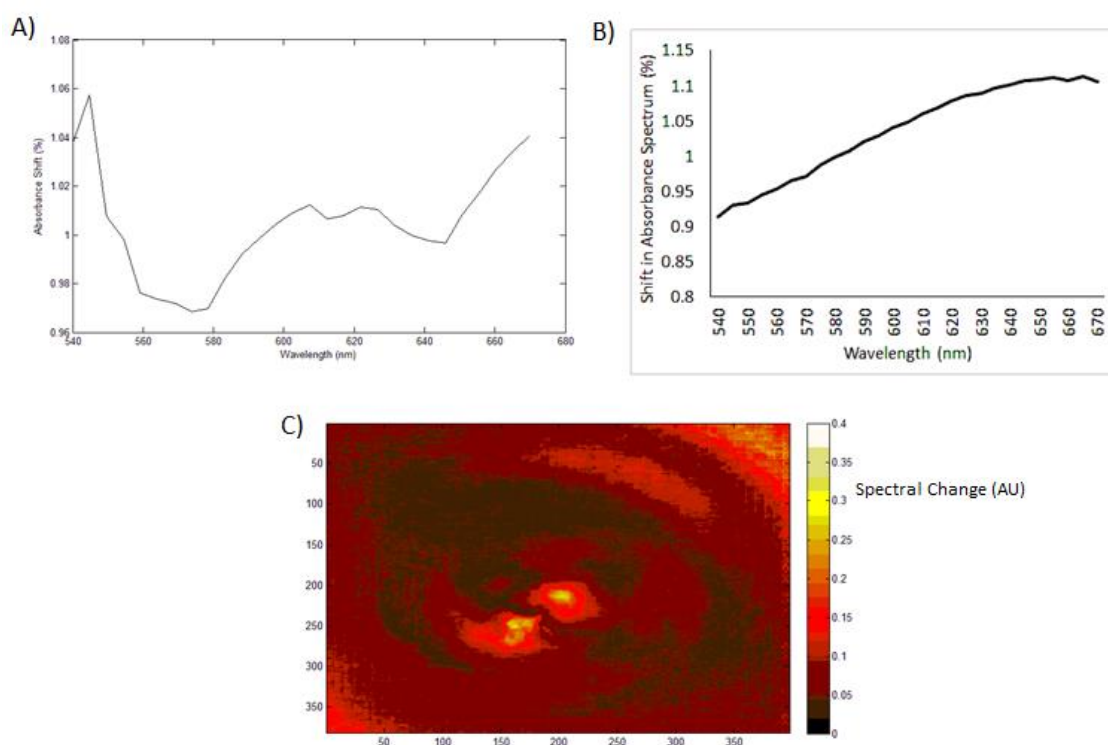


**Figure 5.5.** A) Average measured shift in absorbance spectrum in the region of interest following on-chip PCR targeting the *E. coli* DXS gene with an initial input of 500fg/ $\mu$ L DNA. While the spectrum demonstrates significant noise concerns, the overall shape is reminiscent of B) the expected shift for particles of the same size over the spectral region from 540-670nm. C) Heat map showing spectral shift measurements in the region of interest as a measure of spectral shape change. As in chapter 4, measurements above 0.15 are considered to be significant. While positive results were observed, significant noise and imaging artifacts were present using this analysis.

### 5.4.3 Limit of Detection Analysis

Following these changes, the combined PCR/LSPR detection chip was tested for limit of detection. Prior to each experiment, the PCR chip was disassembled, treated with DNase, sonicated in 70% ethanol, and heated to 70C to remove any residual enzymes prior to being reassembled with a freshly prepared glass coverslip coated with nanoplates and functionalized with DNA probes. The chip was then filled with PCR solutions containing 0, 5, 50, 500 and 5000 fg/ $\mu$ L of DNA isolated from Stb13 E.coli as described above. For each sample, the chip was allowed to thermocycle for 35 cycles with spectral measurements taken every three minutes. Measurements consisted of 170 images taken over 40 wavelength points in the range from 560-640nm for  $\sim$ 2nm resolution using a Reitiga EXi camera with 250ms integration time. Figure 5.6A shows the average measured shift in spectral peak in the detection zone over the course of thermocycling for the various starting concentrations of DNA. In cases with higher concentrations of DNA, peak spectral shift was observed within 10-15 minutes, or less than 20 cycles. Signal was still observed at 5fg/ $\mu$ L, though it was significantly lower indicating that amplification occurred, but not to the level of higher concentration samples. These results indicated that the limit of detection of the system was  $\sim$ 5fg/ $\mu$ L, which corresponds to  $\sim$ 300 bacteria/mL of sample[334]. Fig. 5.6B shows the measured average spectral shift by input DNA concentration, indicating a plateau at an average spectral shift of  $\sim$ 0.5%. Interestingly, seemingly cyclical distortions in the spectral shift data were observed, possible indicating some effect on hybridization from changes in temperature or small motion artifacts.

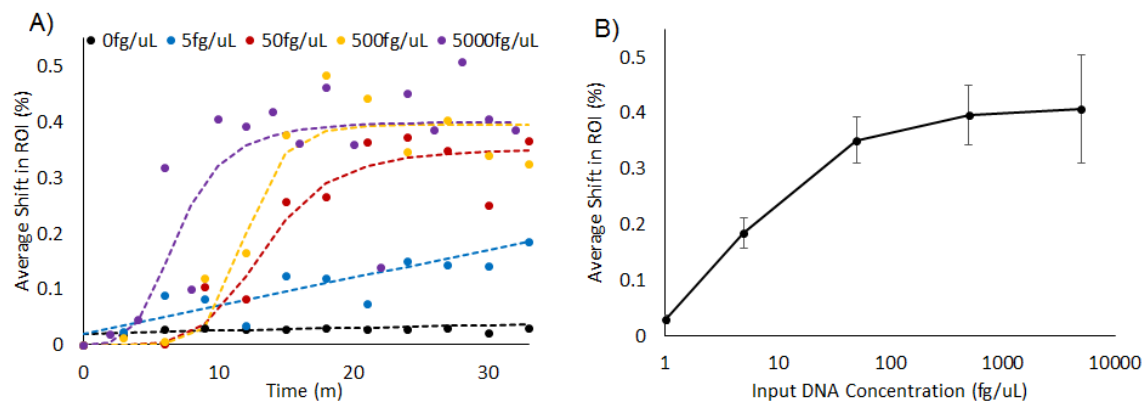


**Figure 5.6.** A) Average spectral shift over time in the ROI as measured by percentage difference from the initial spectrum. Input DNA concentrations of 0, 5, 50, 500, 5000 fg/ $\mu$ L demonstrated. Dashed lines indicate best-fit regression for each experiment. B) Maximum average shift as a function of input DNA concentration. Plateau occurs at an average shift of  $\sim$ 0.4%. Note that average shift across the ROI accounts for both hybridized pixels and non-hybridized, maximum spectral shifts were measured at  $\sim$ 1% in these cases. Error bars indicate error from regression.

While the average spectral shift measured in the region of interest peaked at 0.5%, the calculated difference maps demonstrated improved signal. Measured signal shift was not fully consistent from one pixel to the next, indicating randomly speckled binding in the hybridization zone that never fully saturates. As a result, the regional average measure accounted for both pixels displaying strong plasmonic shift and those that weren't. Maximum spectral shift observed on a pixel-by-pixel basis was consistently double the average measurement, or approximately 1% for DNA concentrations in the plateau region of the response curve. Figure 5.7 demonstrates this effect, showing time-lapsed images of the ROI taken with an input DNA concentration of 5fg/ $\mu$ L. While the regional average spectral shift was approximately 0.2% at this concentration, the maximum spectral shift reached 0.45% with many pixels at 0.3-0.35%.

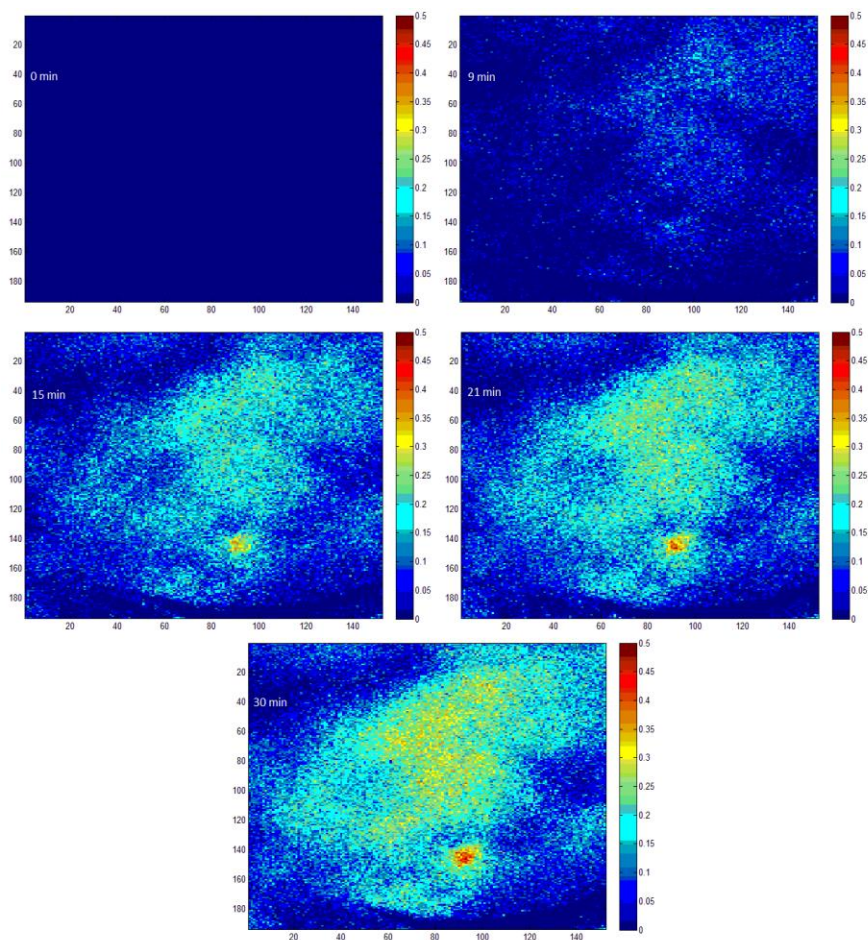


**Figure 5.7.** Heat map series showing spectral shift over time in the region of interest expressed as a percentage of initial spectra. All data were generated using  $5\text{fg}/\mu\text{L}$  input. Probes were localized to a round droplet in the center of the hybridization region. While the largest shifts observed were  $\sim 0.5\%$ , a clear increase in signal over time is observed over the course of thermocycling. Time points are A) initial, B) 9m, C) 15m, D) 21m, E)30m.

#### 5.4.4 On-Chip Multiplex PCR

Following demonstration of single-target PCR, the potential for multiplex PCR utilizing the looped-flow thermocycler/LSPR system was evaluated. A detection zone was prepared as before on a glass slide, but the DNA probes were instead placed in droplets to define two separate regions of interest targeting different genes (*tufB* and *DXS*). As before,



a 10 $\mu$ L droplet of each probe at 35 $\mu$ M concentration was placed on the monolayer surface and allowed to incubate for one hour before washing with diH<sub>2</sub>O. A PCR chip was then constructed using the multiplex coverslip.

After the multiplex chip was constructed, DNA samples were prepared by separately performing PCR targeting *tufB* and *DXS* genes with *E.coli* DNA input. The samples were separated using gel electrophoresis, and the bands indicating the two genes were cut out of the gels, melted with guanidine hydrochloride and isolated using a DNEasy solid-phase extraction kit (Qiagen, Hilden, Germany). PCR experiments for the multiplex chip were then performed by preparing PCR solutions with combinations of the two DNA isolates: positive for both genes, negative for both, and +/- for each. 200nM concentrations of both sense and antisense primers for each target were used, with 500fg/ $\mu$ L concentrations of positive input DNA to ensure complete amplification. Fig. 6 shows pseudocolor difference map images for the multiplex PCR experiment. Similar maximum spectral shift values were observed, at approximately 1% spectral shift in hybridization zones for positive samples. These results demonstrate that multiplex PCR is possible using the looped PCR/LSPR chip.

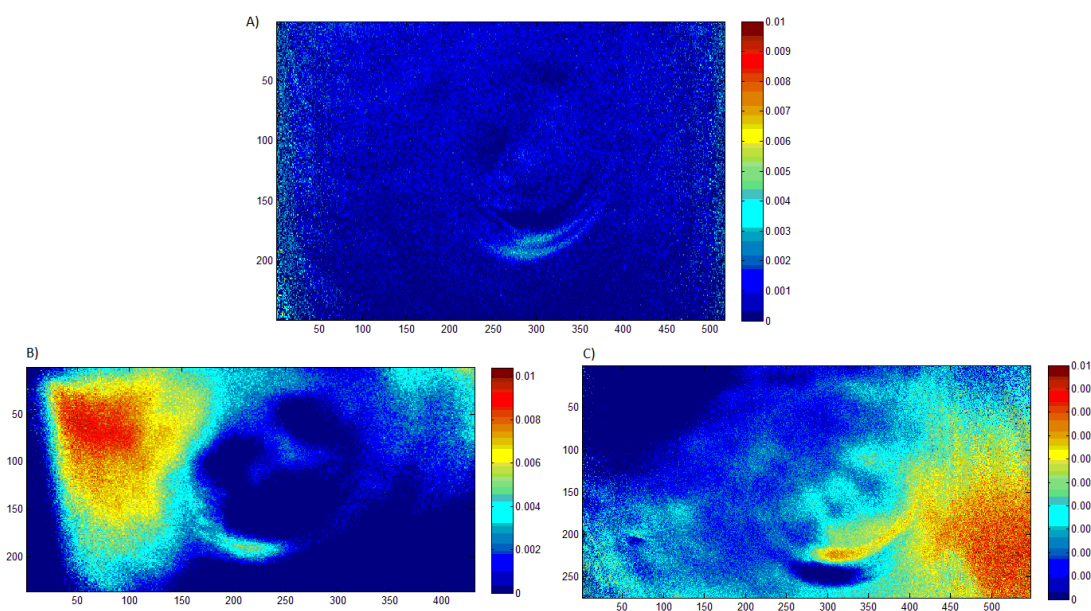


**Figure 5.8.** Output heat map spectra for multiplex PCR experiments. In all cases, *tufB* probes localized to left side of the image and *DXS* probes to the right. A) Blank (no input DNA), B) *tufB* positive, *DXS* negative, C) *tufB* negative, *DXS* positive. Note that while output is noisy, clear localization of signal in the hybridization regions can be seen.

## 5.5 DISCUSSION

A microfluidic PCR chip utilizing piezoelectrically pumped looped flow and an LSPR based detection scheme was constructed and validated, demonstrating a limit of detection of  $5\text{fg}/\mu\text{L}$ , indicating a level of resolution comparable to or better than most conventional PCR systems. Detection of target markers occurred consistently within 20 minutes, allowing for rapid diagnosis, with potential for even faster detection with shorter step times and improved heating rates achievable by replacing the TEC. Additionally, on-chip multiplex detection was demonstrated, increasing the diagnostic potential of such a device. The label-free nature of LSPR compared to standard hybridization arrays or fluorescent detection allows for the

possibility of large arrays with real-time analysis. The looped design of the device makes it ideal for addition to a continuous flow sample preparation system to isolate bacteria from a blood sample for rapid detection of resistance markers in patients suffering from BSIs.

While consistent detection of very low signal was demonstrated, resolving average spectral shifts as low as 0.2%, overall plasmonic shift from the hybridization arrays were lower than expected, indicating a lack of binding saturation that could prove difficult to overcome for any potential increase in device sensitivity. Additionally, periodic drop-off in signal was observed during PCR detection. This could be due to chance overlap of camera imaging with certain heating cycles – tying camera control to certain steps in thermocycling much like motion control for CT/MR scanning could help reduce these effects. On the whole, a combined LSPR/PCR chip has been described that serves as an excellent detection platform with potential for expansion with in-flow sample preparation systems.

## **5.6 ACKNOWLEDGEMENTS**

The author would like to thank Mitchell Hawkins for the fabrication of not one, but two copies of the fluidic chip out of polycarbonate. His timely assistance was invaluable to this project.

## CHAPTER 6:

### Conclusions and Future Directions

#### 6.1 CONCLUSIONS

Due to the prevalence of nosocomial bloodstream infections and the associated mortality and costs, there is an urgent need for rapid, inexpensive assays for characterization of causative pathogens and antimicrobial resistances. This would allow for timely treatment while minimizing the risk of developing new resistant strains and superbugs inherent in broad spectrum antimicrobial treatment, a critical concern in modern medicine. Since such an assay would need to be able to detect a wide range of resistances and pathogenic species, genetic markers are an ideal avenue for analysis. As the concentration of pathogens in BSIs are often very low, amplification prior to detection makes PCR based assays an ideal option, particularly when coupled with microfluidics for rapid analysis and potential for automation and side-by-side assays.

The major components of a PCR-based microfluidic system are thermocycling and temperature control, the fluidic assembly itself, and a detection scheme. In Chapter 3, fluidic and thermocycling systems were developed with a focus on integration of a DNA hybridization array detection scheme for multiplex analysis. A rapid thermocycling platform was created using a thermoelectric heating element controlled by an integrated resistance thermal detector connected to a control board with custom software. Coupled with a fluidic chip utilizing an aluminum substrate for thermal conductivity, three step PCR was achieved with a minimal time between steps of <10s, leading to potential assay time of less than 20 minutes and highly stable thermal control. A continuous flow looped thermocycling chip allows for the potential of in-line integration into sample preparation systems.

Multiplex detection of genetic markers following PCR requires probes specific to the markers amplified – simple detection of DNA quantity would not differentiate between signals. Chapter 4 discusses the optimization of silver nanoprisms for use in a monolayer LSPR imaging hybridization array and the subsequent development of a two-dimensional spectroscopic imaging system for LSPR applications. A highly-tunable citrate stabilized silver nanoprism synthesis protocol was developed for maximal stability and functionalizability. These were then used for an LSPR imaging system which demonstrated ability to detect a shift in absorption spectra as low as 0.2% of the signal. This sensor, while not as sensitive as classical LSPR systems, is significantly lower cost due to usage of a DMD to create spectral resolution rather than full spectroscopy. In addition to the application utilized in this dissertation, such a system has a wide array of potential uses for biosensors due to the label-free and assay non-specific nature of LSPR.

With all three major components of a microfluidic PCR-based total analysis system functional, they were integrated (see Chapter 5) to create a system capable of multiplex detection of genetic markers from a lysed cell input. The limit of detection of the device was characterized, resulting in a lower limit of 5fg/ $\mu$ L of E.coli DNA, approximately equivalent to 59 bacteria, or copies of the target gene in a 200 $\mu$ L sample. While this concentration is not ideal for detection directly from a clinical blood sample due to the low concentration of pathogens in a typical patient with a BSI, it was still surprisingly low, and the continuous flow microchip system lends itself well to adaptation of a sample preparation system for increasing the concentration of pathogens. In addition, multiplex PCR analysis was successfully demonstrated, indicating the potential value for analysis of panels of genetic targets in a short period of time.

The primary focus of the studies in this dissertation was the development of a microfluidic total analysis system designed to take in a pathogen sample, run genetic

analysis and determine the presence of a targeted set of genetic antimicrobial resistance markers in less than two hours in order to minimize the time to effective treatment for patients with bloodstream infections. This work demonstrated a fully realized system utilizing a TEC-based thermocycler and looped continuous flow chip with an optical LSPR imaging system for interrogation of nanoparticle absorption shift with changes in the local dielectric constant due to DNA hybridization between thiol-immobilized probes and target genetic sequences. The hybridization array design allows for multiplex analysis alongside the label-free and highly sensitive detection of LSPR imaging. While the resulting limit of detection was not sensitive enough for direct clinical usage without some form of sample preparation, the overall platform design provides potential for in-line application with sample preparation systems to make it viable for clinical samples.

## **6.2 FUTURE DIRECTIONS**

### **6.2.1 Optical and Microfluidic Improvements**

There is significant opportunity for expansion on the work demonstrated in this dissertation. Further refinement of optical systems, particularly focused on reduction of the inherent diffraction effect found in digital micromirror devices, would allow for increasing the luminous flux of the system and thus its sensitivity. Similarly improving camera sensitivity could allow for a reduced integration time, and thus more measurements taken over time. Automation of camera control could also be used to reduce time between spectral measurements.

On the microfluidics side of the system, the demonstration of multiplex PCR detection opens the door for hybridization panel assays, so characterizing the maximum number of potential targets for amplification and detection in a single multiplex experiment and any effects on SNR would be highly valuable. Other potential avenues of exploration include optimization for usage of stochastic hybridization probes for bacterial

characterization, implementation of alternative reagents for faster PCR protocols, and development of a reagent mix for optimal PCR results.

### **6.2.2 Sample Preparation Systems**

Beyond the current scope of the project, the continuous flow design paradigm adopted for the fluidic components developed herein was intended for the primary purpose of being a modular component of a more extensive total analysis system or other assays. Notably, sample preparation prior to thermocycling would allow for isolation of pathogens from clinical samples and subsequent lysis to concentrate the sample input to the PCR system and allow for rapid detection of resistance markers directly. Such a sample preparation system could consist of introduction of a lysis buffer containing saponin, polyethylene glycol and sodium polyanetholesulfonate[111] for debulking of human blood cells, both red and white, followed by a system for concentration of pathogens using a technique such as dielectrophoretic field-flow fractionation (DEP-FFF). DEP-FFF has previously been demonstrated for trapping of bacteria[335], viruses[336] and fungal spores[337], and could thus be used to isolate such pathogens into a plug flow for input into the thermocycling system.

Of course, such an input system would require lysis as well prior to thermocycling – PCR requires free DNA, and cellular proteins can inhibit the activity of polymerase, thus preventing the reaction from occurring. Treatment of pathogens with sodium dodecyl sulfate has been shown to result in efficient lysis through solubilization of cell walls and viral capsids. While SDS is also known to inhibit PCR by denaturing DNA polymerase enzymes, inclusion of 0.5% Tween-20 in the reaction buffer neutralizes SDS and prevents this, thus allowing for potential PCR following SDS-mediated lysis[163].

Further potential sample preparation side advancements include DNA isolation to improve the limit of detection by concentrating DNA into a smaller sample volume while

simultaneously removing potential protein contaminants. Possible approaches for DNA isolation from bulk solution include solid phase extraction electrophoretic focusing methods. Solid phase extraction techniques for DNA isolation utilize a silicon-based sol gel which DNA will bind to in the presence of a salt such as guanidine hydrochloride. Following binding, trapped DNA is released in the presence of polar solvents. While effective and commonly used in microbiology laboratories for isolation and purification of DNA, solid phase extraction requires flow through a column, multiple buffer washes, and chemical agents that inhibit PCR. On-chip solid phase extraction has been demonstrated, but it is not ideal for a continuous flow system[338].

### **6.2.3 Electrophoretic DNA Focusing**

Electrophoretic isolation is much more ideal for continuous flow applications, and lends itself well to use in a series of sample preparation components prior to analysis. In principle, an electric field is applied transverse to a fluidic channel to induce electrophoretic motion in charged molecules such as DNA to isolate them into a flow stream for output. The primary drawback of electrophoresis across a channel structure is the formation of microbubbles due to electrolysis of water at the surface of the electrodes, which could subsequently be disastrous for PCR. In order to avoid this, a channel structure with sidewalls composed of 3.5kD dialysis membrane can be used, placing electrodes outside the channel structure in buffer reservoirs. This allows small ions to pass the membrane and maintain an electric field while larger DNA molecules remain inside the channel and microbubbles form exclusively external (Fig 6.1). In this manner, an H-bridge channel layout can be used to transfer DNA to a second sample stream.



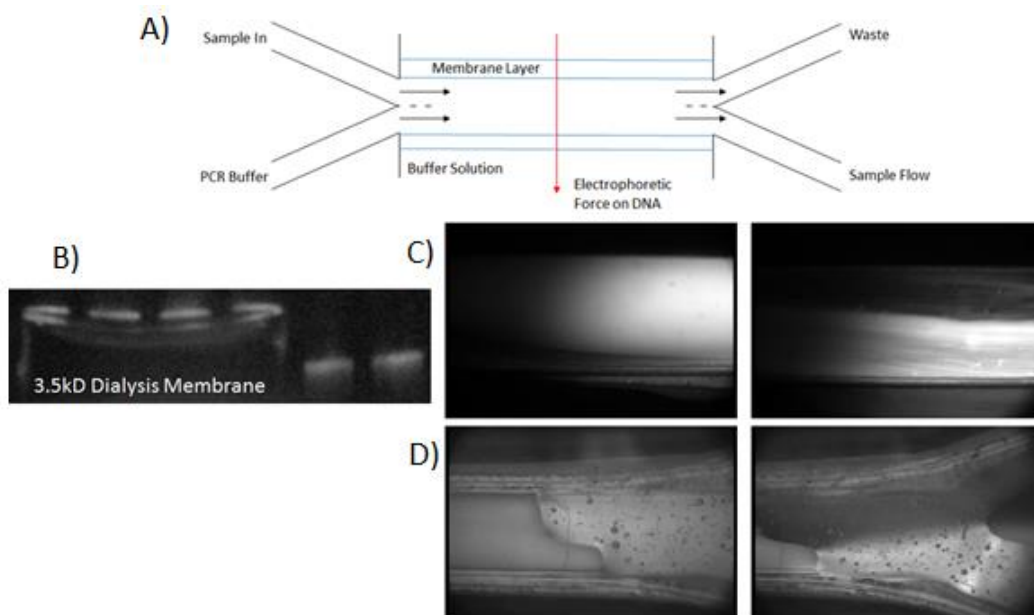


**Figure 6.1.** A) Diagram of transverse electrophoretic concentrator for DNA inputs. The system uses an H-bridge design in conjunction with dialysis membrane separating the sample channel from electrodes in buffer solution to prevent formation of microbubbles through electrolysis. B) Gel electrophoresis of bulk DNA with and without intervening dialysis membrane. DNA in the path of the membrane did not pass through, indicating that the pore size was small enough to keep DNA in the channel. C) Electrophoretic focusing of negatively charged fluorescent beads from an input stream (left) into the secondary output stream (right). D) Electrophoretic focusing of DNA from a single input (left) into the output stream (right).

In preliminary experiments performed for this potential technique, multiple channel cross-sections were utilized for transverse electrophoretic focusing (Fig. 6.2A). DNA concentration was successfully increased from a single bulk solution input into a reduced output stream, however DNA trapping against the dialysis membrane where the net flow rate was zero due to boundary conditions prevented recovery of significant portions of DNA input to the system. In a diagnostic system that requires all present DNA to accurately assess the range of markers present in the sample, this is an unacceptable trade-off.

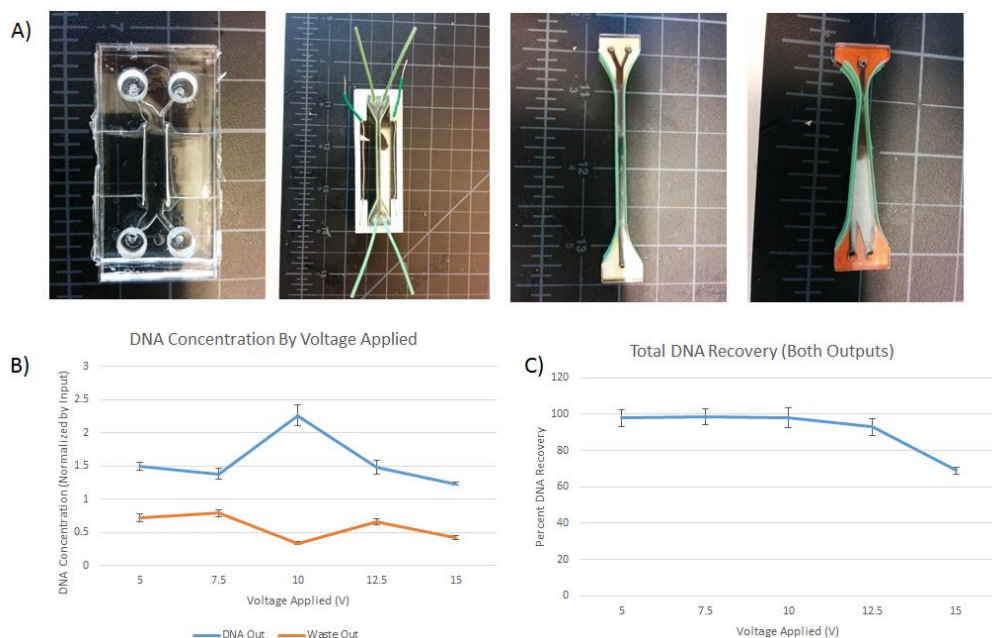


**Figure 6.2.** A) Design iterations on electrophoretic DNA concentrator. From left to right, PDMS H-bridge, narrowed PMMA H-bridge, Y-bridge for concentrating from a single source flow, widening Y-bridge to reduce DNA trapping at the membrane interface from boundary flow conditions. B) DNA concentration as a percentage of input as measured from both concentrator and waste output flows. Maximum focusing was found to occur at 10V/cm, stronger electric fields resulted in turbulent flow and increased trapping, as seen in C), total DNA recovery from both outputs following focusing. Electric fields above 10V/cm resulted in decreased recovery of DNA due to higher levels of trapping at membranes.

While DNA trapping against the channel wall prevents transverse electrophoretic concentration from viability in a system such as the one presented herein, the same physical concepts can be applied to the concept of isoelectric focusing[339]. An ampholytic buffer solution can be introduced to the microchip by sheath flow on either side of the primary input. This creates a spatially resolved pH gradient across the channel which can then be used to separate biomolecules by isoelectric point – the pH at which the net charge of the molecule becomes zero, thus leading to zero electrophoretic mobility. DNA carries a characteristic isoelectric point of 4-4.2, so output flow can be set using relative flow rates to isolate this pH band.

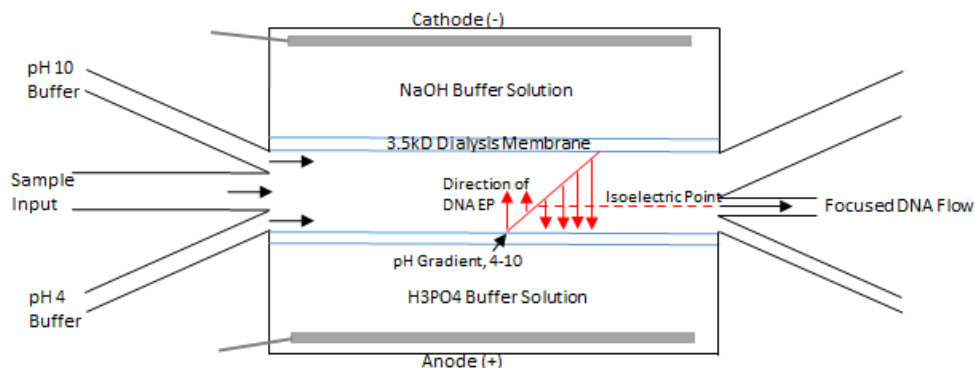


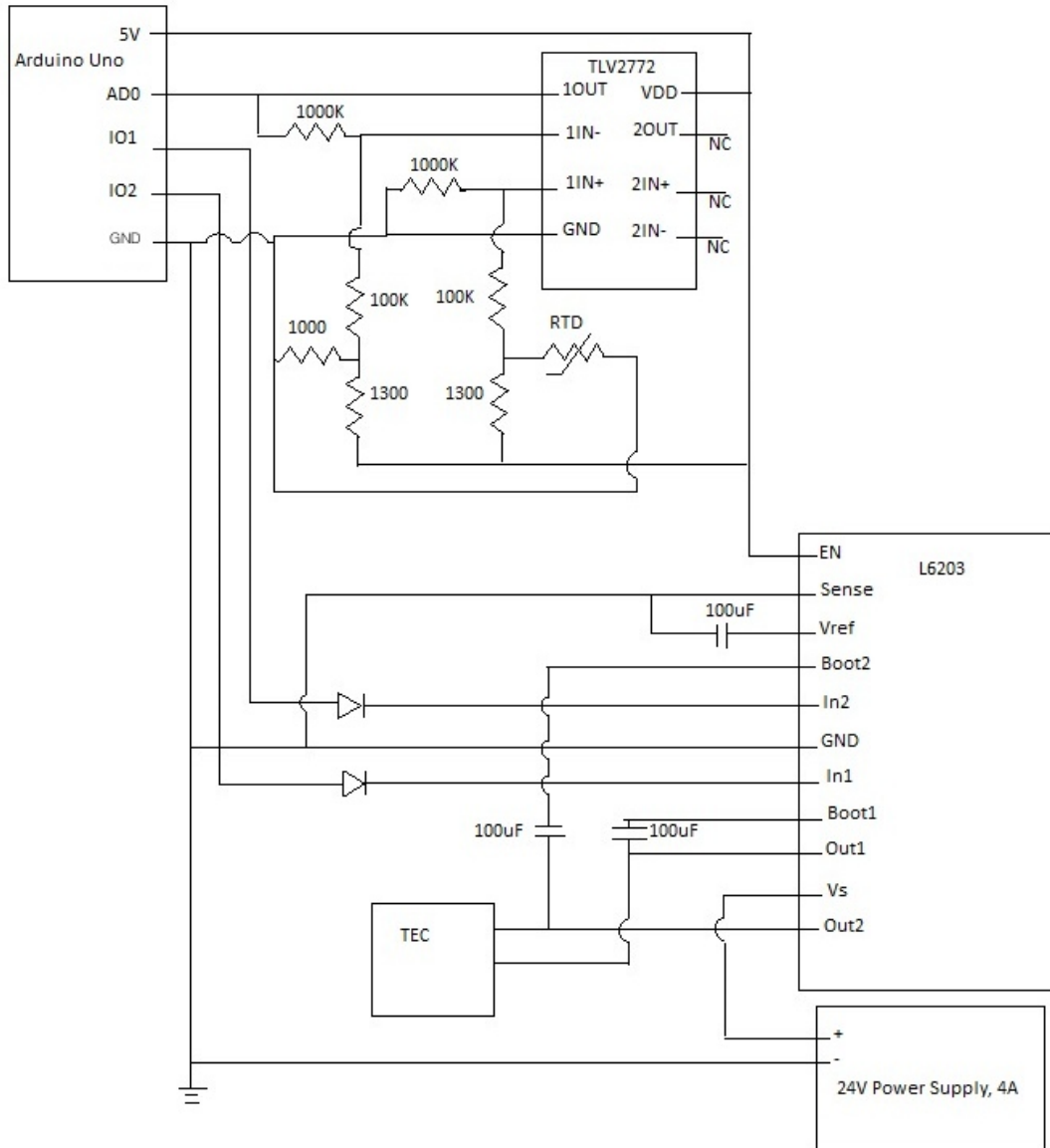
**Figure 6.3.** Schematic of a potential isoelectric focusing flow chamber. Sheath flow is induced from two pH buffers, creating a pH gradient across the channel. Organic molecules, including DNA, will localize to the electrophoretic force minimum, the point at which their charge is zero, or isoelectric point. An output tuned to collect this pH band in the gradient can then be used to isolate DNA away from other biomolecules and debris.

#### 6.2.4 Parallel Assays

One of the greatest advantages of utilizing both a microfluidic system and a label-free detection method such as LSPR imaging is that there is strong potential for parallel assays within the same chip design paradigm and sensing method. LSPR imaging has been demonstrated for detection of analytes in a wide variety of commonly used molecular biology assays, including ELISA[340], cell assays[341], and others. With a sample preparation step to separate sample streams and careful tuning of flow chamber resistances, it would be possible to expand the device presented here to perform more than one of these assays simultaneously. For example, proteins separated during a DNA isolation step could be diverted to a channel passing over an LSPR imaging array functionalized with antibodies for protein targets, allowing simultaneous analysis of pathogenic DNA and protein content with minimal increase in device costs. While addition of other detection modalities would allow for even further exploration, multiple detection schemes would dramatically increase the cost of manufacturing and maintenance.

# APPENDIX

## Appendix A - Circuit Diagram for TEC Thermocycler



## Appendix B - PID Control Program for Arduino – AmpliTaq Gold PCR Protocol

```
// PCR Thermocycle control through RTD

// Initialize all global variables for the program
int cycle = 1;
int maxCycle = 36;
int currentStep = 0;
int pulseMax = 100;
int timeStep = 100; //Time step in milliseconds
double integral = 0; //PID control variables
double diff = 0;
double previousError = 0;
int timeAtTemp = 0; //Time since current target reached
int ct = 0;
boolean firstPoint = true;
double sets[] = {96, 64, 70}; //Target temperatures
int locks[] = {75, 10, 30}; // "Lock" points for each target (output at which the temperature is stable)
double set = 95;
int lock = 75;
int pulseSum = 0;
boolean atTarget = false;
boolean problem = false; //True if an error is encountered, resets current step
int repeatErrorCount = 0; //Check for repeated incorrect error readings

void setup(){
  // Initialize feed to computer
  Serial.begin(9600);
  Serial.println("Vin  Temperature  Error  Integral  Pulse Time  Target Time  Cycle");

  // Set output pins to H-bridge
  pinMode(2, OUTPUT);
  pinMode(3, OUTPUT);
  digitalWrite(0, LOW);
  digitalWrite(0, LOW);
}

// Main program loop
void loop(){
  // Exit functionality if the program is done or a problem is encountered (the loop never ends on Arduino,
  // so the controller will just idle)
  if (cycle<=maxCycle && !problem){

    boolean stepChange = false;
    // Check for end of step conditions, modify targets appropriately\
    //55
    if (currentStep == 2 && timeAtTemp > 0 && set > 60){
      set = set - 0.08;
    }
    if (timeAtTemp == 65 && currentStep == 2){
      currentStep = 3;
      set = sets[2];
      lock = locks[2];
      locks[1] = pulseSum/(timeAtTemp - 10);
      stepChange = true;
    }
    //55
  }
}
```

```

if (timeAtTemp == 55 && currentStep == 1){
  currentStep = 2;
  set = sets[1];
  lock = locks[1];
  if (cycle != 1){
    locks[0] = pulseSum/(timeAtTemp - 10);
  }
  stepChange = true;
}
//100
if (timeAtTemp == 100 && currentStep == 3){
  if (cycle!= 35){
    currentStep = 1;
    set = sets[0];
    lock = locks[0];
    locks[2] = (locks[2] + pulseSum/(timeAtTemp - 10))/2;
    stepChange = true;
  } else{
    timeAtTemp = 0;
  }
  cycle++;
}

// First step, first cycle ending
if (timeAtTemp == 2400 && cycle == 1 && currentStep == 0){
  currentStep = 1;
  set = sets[0];
  lock = locks[0];
  stepChange = true;
}

if (stepChange){
  pulseSum = 0;
  integral = 0;
  pulseMax = 100;
  timeAtTemp = 0;
  firstPoint = true;
  atTarget = false;
  stepChange = false;
}

// Read in voltage and calculate current temperature
double input = analogRead(0);
double vin = 5*input/1024;
double res = (1280*(vin + 21.55))/(28.05 - vin);
double temp2 = (res - 1000)/3.853;
double temp = 25 + 1.2*(temp2-25);

// Calculate error
double error = set - temp;

// If the error is more than 3 degrees above the target, something is wrong - cease heating
if (error < -2 && (currentStep!=2 || atTarget)){
  problem = true;
}

// Within two degrees of target, start count and activate the integral
// Original second condition: ((currentStep!=2 && error < 2) || (currentStep==2 && abs(error) < 1))

```

```

if (!atTarget && ((currentStep!=2 && error < 2) || (currentStep==2 && error >= -1 && temp > 0))) {
    atTarget = true;
    integral = (pulseMax*lock)/200;
}

if (!firstPoint) {
    // If the change in error is too high, there is a misread, keep the old error
    if (abs(error - previousError) > 7) {
        error = previousError;
        repeatErrorCount++;
        // If too many high change errors encountered in a row, heating is out of control and needs to be stopped
        if (repeatErrorCount > 5) {
            problem = true;
        }
    } else {repeatErrorCount = 0;}
    diff = 10*(error - previousError); // Calculate differential term
}

// If the target is near, calculate the integral term and increment target count
if (atTarget) {
    integral += (error/4);
    timeAtTemp++;
}

previousError = error;
int PIDout = error + 2*diff + 2*integral; // Calculate PID output

if (abs(error) < 5) {
    PIDout = 2*error + 2*diff + 2*integral;
}

// If PID output is greater than the max seen thus far, update the max
if (abs(PIDout) > pulseMax) {
    pulseMax = abs(PIDout);
}
int pulseOut = (timeStep*PIDout)/pulseMax; // Calculate pulse output time (milliseconds)

// If not at the target yet, full power
if (!atTarget) {
    if (currentStep==3) {
        pulseOut = timeStep - 10;

        // If getting close to target, reduce power towards lockpoint to prevent overshoot
        if (error < 10) {
            pulseOut = lock + (timeStep - lock)*error/10;
            if (ct%10==0 && error < 5) {
                lock = lock + 1;
            }
        }
    } else if (currentStep!=2) {
        pulseOut = timeStep;
    } else { pulseOut = -1*(timeStep-15); } //Until problem with Peltier cooling is fixed
}

if (temp<0 || temp > 97 || problem) { pulseOut = 0;}
// Output in the appropriate direction to h-bridge
if (pulseOut > 0) {
    digitalWrite(3,LOW);
}

```

```

digitalWrite(2,HIGH);
delay(pulseOut);
} else if (pulseOut < 0){
digitalWrite(2,LOW);
digitalWrite(3,HIGH);
delay(abs(pulseOut));
}
// If not running at full power, turn off output for appropriate time
if (abs(pulseOut) < timeStep){
int downPulse = timeStep - abs(pulseOut);
digitalWrite(2,LOW);
digitalWrite(3,LOW);
delay(downPulse);
}

if (timeAtTemp > 10 && cycle != 1){
pulseSum += pulseOut;
}

// Output relevant stats to computer screen once per second
if (ct%10 == 0){
if (ct != 0 && ct%200 == 0){
Serial.println();
Serial.println("Vin Temperature Error Integral Pulse Time Target Time Cycle");
}
}

Serial.print(vin);
Serial.print(" ");
Serial.print(temp);
Serial.print(" ");
Serial.print(error);
Serial.print(" ");
Serial.print(integral);
Serial.print(" ");
Serial.print(pulseOut);
Serial.print(" ");
Serial.print(timeAtTemp/10);
Serial.print(" ");
Serial.println(cycle);
}
ct++;
firstPoint = false;
} else{

// If outside the main program, shut down output. The controller will idle here after program completion.
digitalWrite(2,LOW);
digitalWrite(3,LOW);

// If the program was exited because of an error, reset the target count and reactivate
if (problem){
atTarget = false;
firstPoint = true;
problem = false;
}
}
}
}

```



## REFERENCES

1. Brock, T.D., *Milestones in Microbiology*. Academic Medicine, 1961. **36**(7): p. 847.
2. Koch, R. and T. Saure, *Aetiology of tuberculosis*. 1890: William R. Jenkins.
3. Abbe, E., *Note on the Proper Definition of the Amplifying Power of a Lens or Lens-system*. Journal of the Royal Microscopical Society, 1884. **4**(3): p. 348-351.
4. Seynaeve, P. and J. Broos, [*The history of tomography*]. Journal belge de radiologie, 1995. **78**(5): p. 284-288.
5. Lauterbur, P.C., *Image formation by induced local interactions: examples employing nuclear magnetic resonance*. 1973.
6. Doi, K., *Computer-aided diagnosis in medical imaging: historical review, current status and future potential*. Computerized medical imaging and graphics, 2007. **31**(4): p. 198-211.
7. Rudin, M. and R. Weissleder, *Molecular imaging in drug discovery and development*. Nature reviews Drug discovery, 2003. **2**(2): p. 123-131.
8. Betzig, E., et al., *Imaging intracellular fluorescent proteins at nanometer resolution*. Science, 2006. **313**(5793): p. 1642-1645.
9. Peercy, P.S., *The drive to miniaturization*. Nature, 2000. **406**(6799): p. 1023-1026.
10. Squires, T.M. and S.R. Quake, *Microfluidics: Fluid physics at the nanoliter scale*. Reviews of modern physics, 2005. **77**(3): p. 977.
11. Gravesen, P., J. Branebjerg, and O.S. Jensen, *Microfluidics-a review*. Journal of Micromechanics and Microengineering, 1993. **3**(4): p. 168.
12. Haeblerle, S. and R. Zengerle, *Microfluidic platforms for lab-on-a-chip applications*. Lab on a Chip, 2007. **7**(9): p. 1094-1110.
13. Whitesides, G.M., *The origins and the future of microfluidics*. Nature, 2006. **442**(7101): p. 368-373.
14. Sia, S.K. and G.M. Whitesides, *Microfluidic devices fabricated in poly (dimethylsiloxane) for biological studies*. Electrophoresis, 2003. **24**(21): p. 3563-3576.
15. Li, X., D.R. Ballerini, and W. Shen, *A perspective on paper-based microfluidics: current status and future trends*. Biomicrofluidics, 2012. **6**(1): p. 011301.
16. Clarke, S. and J. Foster, *A history of blood glucose meters and their role in self-monitoring of diabetes mellitus*. British journal of biomedical science, 2012. **69**(2): p. 83.
17. Ehrenkranz, J.R., *Home and point-of-care pregnancy tests: a review of the technology*. Epidemiology, 2002. **13**(3): p. S15-S18.
18. Merriman, B., et al., *Progress in ion torrent semiconductor chip based sequencing*. Electrophoresis, 2012. **33**(23): p. 3397-3417.
19. Mueller, O., et al., *A microfluidic system for high-speed reproducible DNA sizing and quantitation*. Electrophoresis, 2000. **21**(1): p. 128-134.
20. Stasiak, J., S. Richards, and S. Angelos, *Hewlett Packard's inkjet MEMS technology: past, present, and future*. 2009.

21. Linder, V., *Microfluidics at the crossroad with point-of-care diagnostics*. *Analyst*, 2007. **132**(12): p. 1186-1192.
22. Sorger, P.K., *Microfluidics closes in on point-of-care assays*. *Nat Biotechnol*, 2008. **26**(12): p. 1345-1346.
23. Choi, S., et al., *Microfluidic-based biosensors toward point-of-care detection of nucleic acids and proteins*. *Microfluidics and Nanofluidics*, 2011. **10**(2): p. 231-247.
24. Hu, M., et al., *Ultrasensitive, multiplexed detection of cancer biomarkers directly in serum by using a quantum dot-based microfluidic protein chip*. *ACS nano*, 2009. **4**(1): p. 488-494.
25. Andersson, H. and A. Van den Berg, *Microfluidic devices for cellomics: a review*. *Sensors and Actuators B: Chemical*, 2003. **92**(3): p. 315-325.
26. Gascoyne, P.R., et al., *Isolation of rare cells from cell mixtures by dielectrophoresis*. *Electrophoresis*, 2009. **30**(8): p. 1388-1398.
27. Chen, C.H., et al., *Antimicrobial susceptibility testing using high surface-to-volume ratio microchannels*. *Analytical chemistry*, 2010. **82**(3): p. 1012-1019.
28. Paturzo, M., et al., *Microscopy imaging and quantitative phase contrast mapping in turbid microfluidic channels by digital holography*. *Lab on a Chip*, 2012. **12**(17): p. 3073-3076.
29. Roco, M.C., *International perspective on government nanotechnology funding in 2005*. *Journal of Nanoparticle Research*, 2005. **7**(6): p. 707-712.
30. Bianco, A., K. Kostarelos, and M. Prato, *Applications of carbon nanotubes in drug delivery*. *Current opinion in chemical biology*, 2005. **9**(6): p. 674-679.
31. Liu, Z., et al., *Far-field optical hyperlens magnifying sub-diffraction-limited objects*. *science*, 2007. **315**(5819): p. 1686-1686.
32. Li, J., et al., *Experimental demonstration of an acoustic magnifying hyperlens*. *Nature materials*, 2009. **8**(12): p. 931-934.
33. Cai, H., et al., *Carbon nanotube-enhanced electrochemical DNA biosensor for DNA hybridization detection*. *Analytical and bioanalytical chemistry*, 2003. **375**(2): p. 287-293.
34. Hu, K., et al., *Electrochemical DNA biosensor based on nanoporous gold electrode and multifunctional encoded DNA– Au bio bar codes*. *Analytical chemistry*, 2008. **80**(23): p. 9124-9130.
35. Na, H.B., I.C. Song, and T. Hyeon, *Inorganic nanoparticles for MRI contrast agents*. *Advanced materials*, 2009. **21**(21): p. 2133-2148.
36. O'Neal, D.P., et al., *Photo-thermal tumor ablation in mice using near infrared-absorbing nanoparticles*. *Cancer letters*, 2004. **209**(2): p. 171-176.
37. Neuberger, T., et al., *Superparamagnetic nanoparticles for biomedical applications: possibilities and limitations of a new drug delivery system*. *Journal of Magnetism and Magnetic Materials*, 2005. **293**(1): p. 483-496.
38. Silin, V., H. Weetall, and D.J. Vanderah, *SPR studies of the nonspecific adsorption kinetics of human IgG and BSA on gold surfaces modified by self-assembled*

- monolayers (SAMs)*. Journal of colloid and interface science, 1997. **185**(1): p. 94-103.
39. Guo, L. and D.-H. Kim, *LSPR biomolecular assay with high sensitivity induced by aptamer–antigen–antibody sandwich complex*. Biosensors and Bioelectronics, 2012. **31**(1): p. 567-570.
  40. McFarland, A.D. and R.P. Van Duyne, *Single silver nanoparticles as real-time optical sensors with zeptomole sensitivity*. Nano letters, 2003. **3**(8): p. 1057-1062.
  41. Ornatska, M., et al., *Paper bioassay based on ceria nanoparticles as colorimetric probes*. Analytical chemistry, 2011. **83**(11): p. 4273-4280.
  42. Posthuma-Trumpie, G.A., J. Korf, and A. van Amerongen, *Lateral flow (immuno) assay: its strengths, weaknesses, opportunities and threats. A literature survey*. Analytical and bioanalytical chemistry, 2009. **393**(2): p. 569-582.
  43. Pankhurst, Q.A., et al., *Applications of magnetic nanoparticles in biomedicine*. Journal of physics D: Applied physics, 2003. **36**(13): p. R167.
  44. Pamme, N., J.C. Eijkel, and A. Manz, *On-chip free-flow magnetophoresis: Separation and detection of mixtures of magnetic particles in continuous flow*. Journal of Magnetism and Magnetic Materials, 2006. **307**(2): p. 237-244.
  45. Zhao, C.-X., et al., *Nanoparticle synthesis in microreactors*. Chemical Engineering Science, 2011. **66**(7): p. 1463-1479.
  46. Karnik, R., et al., *Microfluidic platform for controlled synthesis of polymeric nanoparticles*. Nano letters, 2008. **8**(9): p. 2906-2912.
  47. Destremaut, F., et al., *Microfluidics with on-line dynamic light scattering for size measurements*. Lab on a Chip, 2009. **9**(22): p. 3289-3296.
  48. Homola, J., S.S. Yee, and G. Gauglitz, *Surface plasmon resonance sensors: review*. Sensors and Actuators B: Chemical, 1999. **54**(1): p. 3-15.
  49. Anker, J.N., et al., *Biosensing with plasmonic nanosensors*. Nature materials, 2008. **7**(6): p. 442-453.
  50. Kneipp, K., et al., *Single molecule detection using surface-enhanced Raman scattering (SERS)*. Physical review letters, 1997. **78**(9): p. 1667.
  51. Jönsson, U., et al., *Real-time biospecific interaction analysis using surface plasmon resonance and a sensor chip technology*. Biotechniques, 1991. **11**(5): p. 620-627.
  52. Haynes, C.L. and R.P. Van Duyne, *Nanosphere lithography: a versatile nanofabrication tool for studies of size-dependent nanoparticle optics*. The Journal of Physical Chemistry B, 2001. **105**(24): p. 5599-5611.
  53. Lesuffleur, A., et al., *Periodic nanohole arrays with shape-enhanced plasmon resonance as real-time biosensors*. Applied Physics Letters, 2007. **90**(24): p. 243110.
  54. Kelly, K.L., et al., *The optical properties of metal nanoparticles: the influence of size, shape, and dielectric environment*. The Journal of Physical Chemistry B, 2003. **107**(3): p. 668-677.
  55. Leibovici, L., et al., *The benefit of appropriate empirical antibiotic treatment in patients with bloodstream infection*. JOURNAL OF INTERNAL MEDICINE- OXFORD-, 1998. **244**: p. 379-386.

56. Valles, J., et al., *Community-acquired bloodstream infection in critically ill adult patients: impact of shock and inappropriate antibiotic therapy on survival*. CHEST Journal, 2003. **123**(5): p. 1615-1624.
57. Yarden, S.-I., et al., *Reappraisal of community-acquired bacteremia: a proposal of a new classification for the spectrum of acquisition of bacteremia*. Clinical infectious diseases, 2002. **34**(11): p. 1431-1439.
58. Lee, C.-C., et al., *Comparison of clinical manifestations and outcome of community-acquired bloodstream infections among the oldest old, elderly, and adult patients*. Medicine, 2007. **86**(3): p. 138-144.
59. Friedman, N.D., et al., *Health care-associated bloodstream infections in adults: a reason to change the accepted definition of community-acquired infections*. Annals of internal medicine, 2002. **137**(10): p. 791-797.
60. Diekema, D., et al., *Epidemiology and outcome of nosocomial and community-onset bloodstream infection*. Journal of clinical microbiology, 2003. **41**(8): p. 3655-3660.
61. Saint, S., D.L. Veenstra, and B.A. Lipsky, *The clinical and economic consequences of nosocomial central venous catheter-related infection: are antimicrobial catheters useful?* Infection Control & Hospital Epidemiology, 2000. **21**(06): p. 375-380.
62. Lubelchek, R.J. and R.A. Weinstein, *Antibiotic resistance and nosocomial infections*. The Social Ecology of Infectious Diseases, 2008: p. 241-274.
63. Kleven, R.M., et al., *Estimating health care-associated infections and deaths in US hospitals, 2002*. Public health reports, 2007: p. 160-166.
64. Artero, A., et al., *Prognostic factors of mortality in patients with community-acquired bloodstream infection with severe sepsis and septic shock*. Journal of Critical Care, 2010. **25**(2): p. 276-281.
65. Young, E.M., M.L. Commiskey, and S.J. Wilson, *Translating evidence into practice to prevent central venous catheter-associated bloodstream infections: a systems-based intervention*. American journal of infection control, 2006. **34**(8): p. 503-506.
66. O'Grady, N.P., et al., *Draft guideline for the prevention of intravascular catheter-related infections*. Centers for Disease Control: Atlanta, GA, 2001.
67. Centers for Disease, C. and Prevention, *Vital Signs: Central Line-Associated Blood Stream Infections—United States, 2001, 2008, and 2009*. Annals of Emergency Medicine, 2011. **58**(5): p. 447-450.
68. Blot, S., et al., *Attributable mortality in critically ill patients with bacteremia involving methicillin susceptible (MSSA) and methicillin resistant Staphylococcus aureus (MRSA)*. Critical Care, 2001. **5**(1): p. 1-2.
69. Alonso-Echanove, J., et al., *Effect of Nurse Staffing and Antimicrobial-Impregnated Central Venous Catheters on the Risk for Bloodstream Infections in Intensive Care Units*. Infection Control & Hospital Epidemiology, 2003. **24**(12): p. 916-925.

70. Marschall, J., et al., *Strategies to prevent central line-associated bloodstream infections in acute care hospitals: 2014 update*. Infection Control & Hospital Epidemiology, 2014. **35**(S2): p. S89-S107.
71. Maki, D.G., D.M. Kluger, and C.J. Crnich, *The Risk of Bloodstream Infection in Adults With Different Intravascular Devices: A Systematic Review of 200 Published Prospective Studies*. Mayo Clinic Proceedings, 2006. **81**(9): p. 1159-1171.
72. Esteve, F., et al., *Bloodstream infection related to catheter connections: a prospective trial of two connection systems*. Journal of Hospital Infection, 2007. **67**(1): p. 30-34.
73. Yeung, S.-C.J., C.P. Escalante, and R.F. Gagel, *Medical care of cancer patients*. 2009: Pmph-usa.
74. Weinstein, M.P., et al., *The Clinical Significance of Positive Blood Cultures: A Comprehensive Analysis of 500 Episodes of Bacteremia and Fungemia in Adults. I. Laboratory and Epidemiologic Observations*. Review of Infectious Diseases, 1983. **5**(1): p. 35-53.
75. Pittet, D., et al., *Microbiological factors influencing the outcome of nosocomial bloodstream infections: a 6-year validated, population-based model*. Clinical infectious diseases, 1997. **24**(6): p. 1068-1078.
76. Rodríguez-Baño, J., et al., *Epidemiology and clinical features of community-acquired, healthcare-associated and nosocomial bloodstream infections in tertiary-care and community hospitals*. Clinical Microbiology and Infection, 2010. **16**(9): p. 1408-1413.
77. Pittet, D., D. Tarara, and R. Wenzel, *Nosocomial bloodstream infection in critically ill patients. Excess length of stay, extra costs and attributable mortality*. JAMA, 1994. **271**.
78. DiGiovine, B., et al., *The Attributable Mortality and Costs of Primary Nosocomial Bloodstream Infections in the Intensive Care Unit*. American Journal of Respiratory and Critical Care Medicine, 1999. **160**(3): p. 976-981.
79. Tabah, A., et al., *Characteristics and determinants of outcome of hospital-acquired bloodstream infections in intensive care units: the EUROBACT International Cohort Study*. Intensive Care Medicine, 2012. **38**(12): p. 1930-1945.
80. Micek, S.T., et al., *Pseudomonas aeruginosa Bloodstream Infection: Importance of Appropriate Initial Antimicrobial Treatment*. Antimicrobial Agents and Chemotherapy, 2005. **49**(4): p. 1306-1311.
81. Vogelaers, D., et al., *Patterns of antimicrobial therapy in severe nosocomial infections: empiric choices, proportion of appropriate therapy, and adaptation rates—a multicentre, observational survey in critically ill patients*. International Journal of Antimicrobial Agents, 2010. **35**(4): p. 375-381.
82. Dimopoulos, G., et al., *Candida albicans versus non-albicans intensive care unit-acquired bloodstream infections: differences in risk factors and outcome*. Anesthesia & Analgesia, 2008. **106**(2): p. 523-529.
83. Leblebicioglu, H., et al., *Device-associated hospital-acquired infection rates in Turkish intensive care units. Findings of the International Nosocomial Infection*

- Control Consortium (INICC)*. Journal of Hospital infection, 2007. **65**(3): p. 251-257.
84. Gould, I., *The epidemiology of antibiotic resistance*. International Journal of Antimicrobial Agents, 2008. **32**: p. S2-S9.
  85. Edmond, M.B., et al., *Nosocomial Bloodstream Infections in United States Hospitals: A Three-Year Analysis*. Clinical Infectious Diseases, 1999. **29**(2): p. 239-244.
  86. Schwalbe, R.S., J.T. Stapleton, and P.H. Gilligan *Emergence of Vancomycin Resistance in Coagulase-Negative Staphylococci*. New England Journal of Medicine, 1987. **316**(15): p. 927-931.
  87. Warren, D.K., et al., *Attributable cost of catheter-associated bloodstream infections among intensive care patients in a nonteaching hospital\**. Critical Care Medicine, 2006. **34**(8): p. 2084-2089.
  88. Elward, A.M., et al., *Attributable Cost of Nosocomial Primary Bloodstream Infection in Pediatric Intensive Care Unit Patients*. Pediatrics, 2005. **115**(4): p. 868-872.
  89. Mermel, L.A., *Prevention of Intravascular Catheter-Related Infections*. Annals of Internal Medicine, 2000. **132**(5): p. 391-402.
  90. Capriotti, T., *Resistant 'superbugs' create need for novel antibiotics*. Dermatology Nursing, 2007. **19**(1): p. 65.
  91. Brusselaers, N., D. Vogelaers, and S. Blot, *The rising problem of antimicrobial resistance in the intensive care unit*. Annals of intensive care, 2011. **1**(1): p. 1.
  92. Levy, S.B., *The challenge of antibiotic resistance*. Scientific American, 1998. **278**(3): p. 32-9.
  93. Cohen, M.L., *Epidemiology of drug resistance: implications for a post-antimicrobial era*. Science(Washington), 1992. **257**(5073): p. 1050-1055.
  94. Watanabe, T., *Infective heredity of multiple drug resistance in bacteria*. Bacteriological Reviews, 1963. **27**(1): p. 87.
  95. Kruse, H. and H. Sørnum, *Transfer of multiple drug resistance plasmids between bacteria of diverse origins in natural microenvironments*. Applied and Environmental Microbiology, 1994. **60**(11): p. 4015-4021.
  96. Cunha, B.A., *Antibiotic resistance: control strategies*. Critical care clinics, 1998. **14**(2): p. 309-327.
  97. Kaye, K.S., et al., *Risk Factors for Emergence of Resistance to Broad-Spectrum Cephalosporins among Enterobacterspp*. Antimicrobial agents and chemotherapy, 2001. **45**(9): p. 2628-2630.
  98. Weber, D.J., R. Raasch, and W.A. Rutala, *Nosocomial infections in the ICU: the growing importance of antibiotic-resistant pathogens*. Chest, 1999. **115**(3): p. 34S-41S.
  99. Zhang, R., et al., *Antibiotic resistance as a global threat: evidence from China, Kuwait and the United States*. Globalization and Health, 2006. **2**(1): p. 1.
  100. Binder, S., et al., *Emerging infectious diseases: public health issues for the 21st century*. Science, 1999. **284**(5418): p. 1311-1313.

101. Laxminarayan, R., et al., *Antibiotic resistance—the need for global solutions*. The Lancet infectious diseases, 2013. **13**(12): p. 1057-1098.
102. Control, C.f.D. and Prevention, *Nosocomial enterococci resistant to vancomycin--United States, 1989-1993*. MMWR. Morbidity and mortality weekly report, 1993. **42**(30): p. 597.
103. Slayton, R.B., et al., *Vital signs: estimated effects of a coordinated approach for action to reduce antibiotic-resistant infections in health care facilities—United States*. MMWR. Morbidity and mortality weekly report, 2015. **64**(30): p. 826.
104. Tavernise, S., *Antibiotic-Resistant Infections Lead to 23,000 Deaths a Year, CDC Finds*. New York Times September, 2013. **17**.
105. Lockhart, S.R., et al., *Antimicrobial resistance among Gram-negative bacilli causing infections in intensive care unit patients in the United States between 1993 and 2004*. Journal of clinical microbiology, 2007. **45**(10): p. 3352-3359.
106. Wang, S., et al., *Healthcare-associated outbreak due to pan-drug resistant Acinetobacter baumannii in a surgical intensive care unit*. Journal of Hospital Infection, 2003. **53**(2): p. 97-102.
107. Gupta, N., et al., *Carbapenem-resistant Enterobacteriaceae: epidemiology and prevention*. Clinical infectious diseases, 2011. **53**(1): p. 60-67.
108. Lockhart, S.R., et al., *Species identification and antifungal susceptibility testing of Candida bloodstream isolates from population-based surveillance studies in two US cities from 2008 to 2011*. Journal of clinical microbiology, 2012. **50**(11): p. 3435-3442.
109. Hajjeh, R.A., et al., *Incidence of bloodstream infections due to Candida species and in vitro susceptibilities of isolates collected from 1998 to 2000 in a population-based active surveillance program*. Journal of clinical microbiology, 2004. **42**(4): p. 1519-1527.
110. Beekmann, S., et al., *Effects of rapid detection of bloodstream infections on length of hospitalization and hospital charges*. Journal of clinical microbiology, 2003. **41**(7): p. 3119-3125.
111. Jarvis, W.R., et al., *WAMPOLE ISOLATOR 10*. J. Clin. Microbiol, 2000. **38**(8): p. 2994.
112. Weinstein, M.P., *Current blood culture methods and systems: clinical concepts, technology, and interpretation of results*. Clinical infectious diseases, 1996. **23**(1): p. 40-46.
113. Jorgensen, J.H. and J.D. Turnidge, *Susceptibility test methods: dilution and disk diffusion methods*, in *Manual of Clinical Microbiology, Eleventh Edition*. 2015, American Society of Microbiology. p. 1253-1273.
114. Reller, L.B., et al., *Antimicrobial susceptibility testing: a review of general principles and contemporary practices*. Clinical infectious diseases, 2009. **49**(11): p. 1749-1755.
115. Dowling, J.N., D.A. McDevitt, and A. Pasculle, *Disk diffusion antimicrobial susceptibility testing of members of the family Legionellaceae including*

- erythromycin-resistant variants of Legionella micdadei*. Journal of clinical microbiology, 1984. **19**(6): p. 723-729.
116. Kiehlbauch, J.A., et al., *Use of the National Committee for Clinical Laboratory Standards guidelines for disk diffusion susceptibility testing in New York state laboratories*. Journal of clinical microbiology, 2000. **38**(9): p. 3341-3348.
  117. Swenson, J.M., F.C. Tenover, and C.D.S. Group, *Results of disk diffusion testing with cefoxitin correlate with presence of mecA in Staphylococcus spp.* Journal of clinical microbiology, 2005. **43**(8): p. 3818-3823.
  118. Unal, S., et al., *Comparison of tests for detection of methicillin-resistant Staphylococcus aureus in a clinical microbiology laboratory*. Antimicrobial agents and chemotherapy, 1994. **38**(2): p. 345-347.
  119. Wieser, A., et al., *MALDI-TOF MS in microbiological diagnostics—identification of microorganisms and beyond (mini review)*. Applied Microbiology and Biotechnology, 2012. **93**(3): p. 965-974.
  120. Choi, J., et al., *Rapid antibiotic susceptibility testing by tracking single cell growth in a microfluidic agarose channel system*. Lab on a Chip, 2013. **13**(2): p. 280-287.
  121. Mohan, R., et al., *A multiplexed microfluidic platform for rapid antibiotic susceptibility testing*. Biosensors and Bioelectronics, 2013. **49**: p. 118-125.
  122. Sutcliffe, J., et al., *Detection of erythromycin-resistant determinants by PCR*. Antimicrobial Agents and Chemotherapy, 1996. **40**(11): p. 2562-2566.
  123. Oliveira, D.C. and H. de Lencastre, *Multiplex PCR strategy for rapid identification of structural types and variants of the mec element in methicillin-resistant Staphylococcus aureus*. Antimicrobial agents and chemotherapy, 2002. **46**(7): p. 2155-2161.
  124. Dutka-Malen, S., S. Evers, and P. Courvalin, *Detection of glycopeptide resistance genotypes and identification to the species level of clinically relevant enterococci by PCR*. Journal of clinical microbiology, 1995. **33**(1): p. 24-27.
  125. Strommenger, B., et al., *Multiplex PCR assay for simultaneous detection of nine clinically relevant antibiotic resistance genes in Staphylococcus aureus*. Journal of Clinical Microbiology, 2003. **41**(9): p. 4089-4094.
  126. Ng, L.-K., et al., *Genetic characterization of antimicrobial resistance in Canadian isolates of Salmonella serovar Typhimurium DT104*. Antimicrobial agents and chemotherapy, 1999. **43**(12): p. 3018-3021.
  127. Lanz, R., P. Kuhnert, and P. Boerlin, *Antimicrobial resistance and resistance gene determinants in clinical Escherichia coli from different animal species in Switzerland*. Veterinary microbiology, 2003. **91**(1): p. 73-84.
  128. Woodford, N., et al., *Multiplex PCR for genes encoding prevalent OXA carbapenemases in Acinetobacter spp.* International journal of antimicrobial agents, 2006. **27**(4): p. 351-353.
  129. Vannuffel, P., et al., *Specific detection of methicillin-resistant Staphylococcus species by multiplex PCR*. Journal of Clinical Microbiology, 1995. **33**(11): p. 2864-2867.



130. Cattoir, V., et al., *Multiplex PCR for detection of plasmid-mediated quinolone resistance qnr genes in ESBL-producing enterobacterial isolates*. Journal of antimicrobial chemotherapy, 2007. **60**(2): p. 394-397.
131. Erlich, H.A., D. Gelfand, and J.J. Sninsky, *Recent advances in the polymerase chain reaction*. Science, 1991. **252**(5013): p. 1643-1651.
132. Kasai, K., R. White, and Y. Nakamura, *Amplification of a variable number of tandem repeats (VNTR) locus (pMCT118) by the polymerase chain reaction (PCR) and its application to forensic science*. Journal of Forensic Science, 1990. **35**(5): p. 1196-1200.
133. Sajantila, A., et al., *The polymerase chain reaction and post-mortem forensic identity testing: application of amplified DIS80 and HLA-DQ $\alpha$  loci to the identification of fire victims*. Forensic science international, 1991. **51**(1): p. 23-34.
134. Lee, J.C.-I. and J.-G. Chang, *ABO genotyping by polymerase chain reaction*. Journal of Forensic Science, 1992. **37**(5): p. 1269-1275.
135. Newton, C., et al., *Diagnosis of  $\alpha 1$  antitrypsin deficiency by enzymatic amplification of human genomic DNA and direct sequencing of polymerase chain reaction products*. Nucleic acids research, 1988. **16**(17): p. 8233-8243.
136. Zietkiewicz, E., A. Rafalski, and D. Labuda, *Genome fingerprinting by simple sequence repeat (SSR)-anchored polymerase chain reaction amplification*. Genomics, 1994. **20**(2): p. 176-183.
137. Gyllensten, U.B. and H.A. Erlich, *Generation of single-stranded DNA by the polymerase chain reaction and its application to direct sequencing of the HLA-DQA locus*. Proceedings of the National Academy of Sciences, 1988. **85**(20): p. 7652-7656.
138. Mullis, K., et al. *Specific enzymatic amplification of DNA in vitro: the polymerase chain reaction*. in *Cold Spring Harbor symposia on quantitative biology*. 1986. Cold Spring Harbor Laboratory Press.
139. Eckert, K.A. and T.A. Kunkel, *DNA polymerase fidelity and the polymerase chain reaction*. Genome Research, 1991. **1**(1): p. 17-24.
140. Kubista, M., et al., *The real-time polymerase chain reaction*. Molecular aspects of medicine, 2006. **27**(2): p. 95-125.
141. Ramakers, C., et al., *Assumption-free analysis of quantitative real-time polymerase chain reaction (PCR) data*. Neuroscience letters, 2003. **339**(1): p. 62-66.
142. Ririe, K.M., R.P. Rasmussen, and C.T. Wittwer, *Product differentiation by analysis of DNA melting curves during the polymerase chain reaction*. Analytical biochemistry, 1997. **245**(2): p. 154-160.
143. Fischer, S. and L. Lerman, *DNA fragments differing by single base-pair substitutions are separated in denaturing gradient gels: correspondence with melting theory*. Proceedings of the national Academy of Sciences, 1983. **80**(6): p. 1579-1583.
144. Breslauer, K.J., et al., *Predicting DNA duplex stability from the base sequence*. Proceedings of the National Academy of Sciences, 1986. **83**(11): p. 3746-3750.

145. Dieffenbach, C., T. Lowe, and G. Dveksler, *General concepts for PCR primer design*. PCR Methods Appl, 1993. **3**(3): p. S30-S37.
146. Abd-Elsalam, K.A., *Bioinformatic tools and guideline for PCR primer design*. african Journal of biotechnology, 2003. **2**(5): p. 91-95.
147. Steitz, T.A., *DNA polymerases: structural diversity and common mechanisms*. Journal of Biological Chemistry, 1999. **274**(25): p. 17395-17398.
148. Gelfand, D.H., *Taq DNA polymerase*, in *PCR technology*. 1989, Springer. p. 17-22.
149. Ling, L.L., et al., *Optimization of the polymerase chain reaction with regard to fidelity: modified T7, Taq, and vent DNA polymerases*. Genome Research, 1991. **1**(1): p. 63-69.
150. Corless, C.E., et al., *Contamination and sensitivity issues with a real-time universal 16S rRNA PCR*. Journal of clinical microbiology, 2000. **38**(5): p. 1747-1752.
151. Brownie, J., et al., *The elimination of primer-dimer accumulation in PCR*. Nucleic acids research, 1997. **25**(16): p. 3235-3241.
152. Vandesompele, J., A. De Paepe, and F. Speleman, *Elimination of primer-dimer artifacts and genomic coamplification using a two-step SYBR green I real-time RT-PCR*. Analytical biochemistry, 2002. **303**(1): p. 95-98.
153. Chou, Q., et al., *Prevention of pre-PCR mis-priming and primer dimerization improves low-copy-number amplifications*. Nucleic Acids Research, 1992. **20**(7): p. 1717-1723.
154. Lebedev, A.V., et al., *Hot start PCR with heat-activatable primers: a novel approach for improved PCR performance*. Nucleic acids research, 2008. **36**(20): p. e131-e131.
155. Paul, N., J. Shum, and T. Le, *Hot start PCR*. RT-PCR Protocols: Second Edition, 2010: p. 301-318.
156. Sagripant, J. and K. Kraemer, *Site-specific oxidative DNA damage at polyguanosines produced by copper plus hydrogen peroxide*. Journal of Biological Chemistry, 1989. **264**(3): p. 1729-1734.
157. De Franchis, R., et al., *A potent inhibitor of Taq polymerase copurifies with human genomic DNA*. Nucleic acids research, 1988. **16**(21): p. 10355.
158. Wiedbrauk, D.L., J.C. Werner, and A.M. Drevon, *Inhibition of PCR by aqueous and vitreous fluids*. Journal of clinical microbiology, 1995. **33**(10): p. 2643-2646.
159. Schrader, C., et al., *PCR inhibitors—occurrence, properties and removal*. Journal of applied microbiology, 2012. **113**(5): p. 1014-1026.
160. Madisen, L., et al., *The effects of storage of blood and isolated DNA on the integrity of DNA*. American journal of medical genetics, 1987. **27**(2): p. 379-390.
161. Kreader, C.A., *Relief of amplification inhibition in PCR with bovine serum albumin or T4 gene 32 protein*. Applied and environmental microbiology, 1996. **62**(3): p. 1102-1106.
162. Nagai, M., A. Yoshida, and N. Sato, *Additive effects of bovine serum albumin, dithiothreitol and glycerol on PCR*. IUBMB Life, 1998. **44**(1): p. 157-163.
163. Bachmann, B., W. Lüke, and G. Hunsmann, *Improvement of PCR amplified DNA sequencing with the aid of detergents*. Nucleic acids research, 1990. **18**(5): p. 1309.

164. Demeke, T. and R. Adams, *The effects of plant polysaccharides and buffer additives on PCR*. Biotechniques, 1992. **12**(3): p. 332-334.
165. Sykes, P., et al., *Quantitation of targets for PCR by use of limiting dilution*. Biotechniques, 1992. **13**(3): p. 444-449.
166. Taberlet, P., et al., *Reliable genotyping of samples with very low DNA quantities using PCR*. Nucleic acids research, 1996. **24**(16): p. 3189-3194.
167. D'aquila, R.T., et al., *Maximizing sensitivity and specificity of PCR by pre-amplification heating*. Nucleic Acids Research, 1991. **19**(13): p. 3749.
168. Nath, P. and K. Chopra, *Thermal conductivity of copper films*. Thin Solid Films, 1974. **20**(1): p. 53-62.
169. Nagai, H., et al., *High-throughput PCR in silicon based microchamber array*. Biosensors and Bioelectronics, 2001. **16**(9): p. 1015-1019.
170. Warner, B.D., et al., *Releasable multiwell plate cover*. 1997, Google Patents.
171. Jalal, H., et al., *Development and validation of a rotor-gene real-time PCR assay for detection, identification, and quantification of Chlamydia trachomatis in a single reaction*. Journal of clinical microbiology, 2006. **44**(1): p. 206-213.
172. Benton, P. and H. Reisner, *A Low-Cost Air-Driven Cycling Oven*. PCR Protocols: A Guide to Methods and Applications, 2012: p. 435.
173. Zhao, Z., et al., *Monolithically integrated PCR biochip for DNA amplification*. Sensors and Actuators A: Physical, 2003. **108**(1): p. 162-167.
174. Khandurina, J., et al., *Integrated system for rapid PCR-based DNA analysis in microfluidic devices*. Analytical Chemistry, 2000. **72**(13): p. 2995-3000.
175. Ke, C., et al., *Single step cell lysis/PCR detection of Escherichia coli in an independently controllable silicon microreactor*. Sensors and Actuators B: Chemical, 2007. **120**(2): p. 538-544.
176. Schneegaß, I., R. Bräutigam, and J.M. Köhler, *Miniaturized flow-through PCR with different template types in a silicon chip thermocycler*. Lab on a Chip, 2001. **1**(1): p. 42-49.
177. Kopp, M.U., A.J. De Mello, and A. Manz, *Chemical amplification: continuous-flow PCR on a chip*. Science, 1998. **280**(5366): p. 1046-1048.
178. Liu, H.-B., et al., *Micro air bubble formation and its control during polymerase chain reaction (PCR) in polydimethylsiloxane (PDMS) microreactors*. Journal of Micromechanics and Microengineering, 2007. **17**(10): p. 2055.
179. Volk, A., et al., *Growth control of sessile microbubbles in PDMS devices*. Lab on a Chip, 2015. **15**(24): p. 4607-4613.
180. Kinzie, P.A. and L.G. Rubin, *Thermocouple temperature measurement*. Physics Today, 1973. **26**: p. 52.
181. Sarma, U. and P.K. Boruah, *Design and development of a high precision thermocouple based smart industrial thermometer with on line linearisation and data logging feature*. Measurement, 2010. **43**(10): p. 1589-1594.
182. Greeff, A., C. Louw, and H. Swart, *The oxidation of industrial FeCrMo steel*. Corrosion Science, 2000. **42**(10): p. 1725-1740.

183. Antontsev, S. and M. Chipot, *The thermistor problem: existence, smoothness uniqueness, blowup*. SIAM Journal on Mathematical Analysis, 1994. **25**(4): p. 1128-1156.
184. de Györgyfalva, G.C. and I. Reaney, *Decomposition of NiMn<sub>2</sub>O<sub>4</sub> spinel: an NTC thermistor material*. Journal of the European Ceramic Society, 2001. **21**(10): p. 2145-2148.
185. Tzeng, J., R. Hsieh, and D.-J. Cheng, *Resistance temperature detector (RTD) formed with a surface-mount-device (SMD) structure*. 2000, Google Patents.
186. Kim, J., et al., *A study on the fabrication of an RTD (resistance temperature detector) by using Pt thin film*. Korean Journal of Chemical Engineering, 2001. **18**(1): p. 61-66.
187. Childs, P., J. Greenwood, and C. Long, *Review of temperature measurement*. Review of scientific instruments, 2000. **71**(8): p. 2959-2978.
188. Terry, S.C., J.H. Jerman, and J.B. Angell, *A gas chromatographic air analyzer fabricated on a silicon wafer*. IEEE Transactions on Electron Devices, 1979. **26**(12): p. 1880-1886.
189. Manz, A., N. Graber, and H.á. Widmer, *Miniaturized total chemical analysis systems: a novel concept for chemical sensing*. Sensors and actuators B: Chemical, 1990. **1**(1): p. 244-248.
190. Reyes, D.R., et al., *Micro total analysis systems. 1. Introduction, theory, and technology*. Analytical chemistry, 2002. **74**(12): p. 2623-2636.
191. van den Berg, A. and T. Lammerink, *Micro total analysis systems: microfluidic aspects, integration concept and applications*, in *Microsystem technology in chemistry and life science*. 1998, Springer. p. 21-49.
192. Auroux, P.-A., et al., *Micro total analysis systems. 2. Analytical standard operations and applications*. Analytical chemistry, 2002. **74**(12): p. 2637-2652.
193. Arora, A., et al., *Latest developments in micro total analysis systems*. Analytical chemistry, 2010. **82**(12): p. 4830-4847.
194. Tüdös, A.J., G.A. Besselink, and R.B. Schasfoort, *Trends in miniaturized total analysis systems for point-of-care testing in clinical chemistry*. Lab on a Chip, 2001. **1**(2): p. 83-95.
195. Lorenz, H., et al., *SU-8: a low-cost negative resist for MEMS*. Journal of Micromechanics and Microengineering, 1997. **7**(3): p. 121.
196. Lin, C.-H., et al., *A new fabrication process for ultra-thick microfluidic microstructures utilizing SU-8 photoresist*. Journal of Micromechanics and Microengineering, 2002. **12**(5): p. 590.
197. Chen, G., et al. *Three-dimensional biologically-active nanostructured architectures in polymer-based microfluidic devices for biomarker detection*. in *Japan Academic Association Inc*. 2006.
198. Joensson, H., et al. *Concurrent multi-sample analysis of low expressed biomarkers on single human cells by enzymatically amplified immunodetection in droplets*. in *12th International Conference on Miniaturized Systems for Chemistry and Life*

- Sciences, MicroTAS 2008, 12 October 2008 through 16 October 2008, San Diego, CA, United States.* 2008. Chemical and Biological Microsystems Society.
199. Zhang, Y., et al., *A surface topography assisted droplet manipulation platform for biomarker detection and pathogen identification.* Lab on a Chip, 2011. **11**(3): p. 398-406.
  200. Li, H. and T. Kenny. *High speed particles separation using ultrasound for microTAS and lab-on-a-chip application.* in *Engineering in Medicine and Biology Society, 2004. IEMBS'04. 26th Annual International Conference of the IEEE.* 2004. IEEE.
  201. Pamme, N. and A. Manz, *On-chip free-flow magnetophoresis: continuous flow separation of magnetic particles and agglomerates.* Analytical chemistry, 2004. **76**(24): p. 7250-7256.
  202. Evander, M. and M. Tenje, *Microfluidic PMMA interfaces for rectangular glass capillaries.* Journal of Micromechanics and Microengineering, 2014. **24**(2): p. 027003.
  203. Zhang, W., et al., *PMMA/PDMS valves and pumps for disposable microfluidics.* Lab on a Chip, 2009. **9**(21): p. 3088-3094.
  204. Rhee, S.W., et al., *Patterned cell culture inside microfluidic devices.* Lab on a Chip, 2005. **5**(1): p. 102-107.
  205. Anderson, J.R., et al., *Fabrication of topologically complex three-dimensional microfluidic systems in PDMS by rapid prototyping.* Analytical chemistry, 2000. **72**(14): p. 3158-3164.
  206. Song, Y., C.S. Kumar, and J. Hormes, *Fabrication of an SU-8 based microfluidic reactor on a PEEK substrate sealed by a 'flexible semi-solid transfer'(FST) process.* Journal of Micromechanics and Microengineering, 2004. **14**(7): p. 932.
  207. Puntambekar, A. and C.H. Ahn, *Self-aligning microfluidic interconnects for glass- and plastic-based microfluidic systems.* Journal of Micromechanics and Microengineering, 2001. **12**(1): p. 35.
  208. Grosse, A., M. Grewe, and H. Fouckhardt, *Deep wet etching of fused silica glass for hollow capillary optical leaky waveguides in microfluidic devices.* Journal of micromechanics and microengineering, 2001. **11**(3): p. 257.
  209. Abgrall, P., C. Lattes, and X. Dollat, *A novel fabrication method of flexible and monolithic 3D microfluidic structures using lamination of SU-8 films.* Journal of Micromechanics and Microengineering, 2005. **16**(1): p. 113.
  210. Mao, X. and T.J. Huang, *Microfluidic diagnostics for the developing world.* Lab on a Chip, 2012. **12**(8): p. 1412-1416.
  211. Dungchai, W., O. Chailapakul, and C.S. Henry, *Electrochemical detection for paper-based microfluidics.* Analytical chemistry, 2009. **81**(14): p. 5821-5826.
  212. Kong, Y., et al., *Fabrication of a gold microelectrode for amperometric detection on a polycarbonate electrophoresis chip by photodirected electroless plating.* Electrophoresis, 2006. **27**(14): p. 2940-2950.

213. Peterson, S.L., et al., *Poly (dimethylsiloxane) thin films as biocompatible coatings for microfluidic devices: cell culture and flow studies with glial cells*. Journal of Biomedical Materials Research Part A, 2005. **72**(1): p. 10-18.
214. Bhattacharya, S., et al., *Studies on surface wettability of poly (dimethyl) siloxane (PDMS) and glass under oxygen-plasma treatment and correlation with bond strength*. Journal of microelectromechanical systems, 2005. **14**(3): p. 590-597.
215. Wilbur, J.L., et al., *Microfabrication by microcontact printing of self-assembled monolayers*. Advanced Materials, 1994. **6**(7-8): p. 600-604.
216. Martinez, A.W., S.T. Phillips, and G.M. Whitesides, *Three-dimensional microfluidic devices fabricated in layered paper and tape*. Proceedings of the National Academy of Sciences, 2008. **105**(50): p. 19606-19611.
217. Chiu, D.T., et al., *Patterned deposition of cells and proteins onto surfaces by using three-dimensional microfluidic systems*. Proceedings of the National Academy of Sciences, 2000. **97**(6): p. 2408-2413.
218. Vladislavjević, G.T., et al., *Industrial lab-on-a-chip: Design, applications and scale-up for drug discovery and delivery*. Advanced drug delivery reviews, 2013. **65**(11): p. 1626-1663.
219. Reynolds, O., *An experimental investigation of the circumstances which determine whether the motion of water shall be direct or sinuous, and of the law of resistance in parallel channels*. Proceedings of the royal society of London, 1883. **35**(224-226): p. 84-99.
220. Purcell, E.M., *Life at low Reynolds number*. Am. J. Phys, 1977. **45**(1): p. 3-11.
221. Tice, J.D., et al., *Formation of droplets and mixing in multiphase microfluidics at low values of the Reynolds and the capillary numbers*. Langmuir, 2003. **19**(22): p. 9127-9133.
222. Stone, H.A. and S. Kim, *Microfluidics: basic issues, applications, and challenges*. AIChE Journal, 2001. **47**(6): p. 1250-1254.
223. Li, Y., et al., *Continuous dielectrophoretic cell separation microfluidic device*. Lab on a Chip, 2007. **7**(2): p. 239-248.
224. Stone, H.A., A.D. Stroock, and A. Ajdari, *Engineering flows in small devices: microfluidics toward a lab-on-a-chip*. Annu. Rev. Fluid Mech., 2004. **36**: p. 381-411.
225. Ward, T., et al., *Microfluidic flow focusing: Drop size and scaling in pressure versus flow-rate-driven pumping*. Electrophoresis, 2005. **26**(19): p. 3716-3724.
226. Terray, A., J. Oakey, and D.W. Marr, *Microfluidic control using colloidal devices*. Science, 2002. **296**(5574): p. 1841-1844.
227. Walker, G.M. and D.J. Beebe, *A passive pumping method for microfluidic devices*. Lab on a Chip, 2002. **2**(3): p. 131-134.
228. Zhang, C., D. Xing, and Y. Li, *Micropumps, microvalves, and micromixers within PCR microfluidic chips: advances and trends*. Biotechnology advances, 2007. **25**(5): p. 483-514.

229. Takao, H., M. Ishida, and K. Sawada, *A pneumatically actuated full in-channel microvalve with MOSFET-like function in fluid channel networks*. Journal of microelectromechanical systems, 2002. **11**(5): p. 421-426.
230. Chen, C.-H. and J.G. Santiago, *A planar electroosmotic micropump*. Journal of Microelectromechanical Systems, 2002. **11**(6): p. 672-683.
231. Au, A.K., et al., *Microvalves and micropumps for BioMEMS*. Micromachines, 2011. **2**(2): p. 179-220.
232. Hong, F., J. Cao, and P. Cheng, *A parametric study of AC electrothermal flow in microchannels with asymmetrical interdigitated electrodes*. International Communications in Heat and Mass Transfer, 2011. **38**(3): p. 275-279.
233. Skaftø-Pedersen, P., et al., *Multi-channel peristaltic pump for microfluidic applications featuring monolithic PDMS inlay*. Lab on a Chip, 2009. **9**(20): p. 3003-3006.
234. Yeo, L.Y. and J.R. Friend, *Ultrafast microfluidics using surface acoustic waves*. Biomicrofluidics, 2009. **3**(1): p. 012002.
235. Ullmann, A., *The piezoelectric valve-less pump—performance enhancement analysis*. Sensors and Actuators A: Physical, 1998. **69**(1): p. 97-105.
236. Stemme, E. and G. Stemme, *A valveless diffuser/nozzle-based fluid pump*. Sensors and Actuators A: physical, 1993. **39**(2): p. 159-167.
237. Wittwer, C.T., et al., *Continuous fluorescence monitoring of rapid cycle DNA amplification*. Biotechniques, 1997. **22**(1): p. 130-139.
238. Kapuscinski, J., *DAPI: a DNA-specific fluorescent probe*. Biotechnic & Histochemistry, 2009.
239. Giglio, S., P.T. Monis, and C.P. Saint, *Demonstration of preferential binding of SYBR Green I to specific DNA fragments in real-time multiplex PCR*. Nucleic Acids Research, 2003. **31**(22): p. e136-e136.
240. Stellwagen, N.C., *DNA gel electrophoresis*, in *Nucleic acid electrophoresis*. 1998, Springer. p. 1-53.
241. Zhang, P., T. Beck, and W. Tan, *Design of a molecular beacon DNA probe with two fluorophores*. Angewandte Chemie, 2001. **113**(2): p. 416-419.
242. Dugat-Bony, E., et al., *Detecting unknown sequences with DNA microarrays: explorative probe design strategies*. Environmental microbiology, 2012. **14**(2): p. 356-371.
243. Li, J., et al., *Hairpin fluorescence DNA probe for real-time monitoring of DNA methylation*. Analytical chemistry, 2007. **79**(3): p. 1050-1056.
244. Freeman, W.M., D.J. Robertson, and K.E. Vrana, *Fundamentals of DNA hybridization arrays for gene expression analysis*. Biotechniques, 2000. **29**(5): p. 1042-1055.
245. Peterson, A.W., R.J. Heaton, and R.M. Georgiadis, *The effect of surface probe density on DNA hybridization*. Nucleic acids research, 2001. **29**(24): p. 5163-5168.
246. Diamandis, E.P. and T.K. Christopoulos, *The biotin-(strept) avidin system: principles and applications in biotechnology*. Clinical chemistry, 1991. **37**(5): p. 625-636.

247. Shalon, D., S.J. Smith, and P.O. Brown, *A DNA microarray system for analyzing complex DNA samples using two-color fluorescent probe hybridization*. Genome research, 1996. **6**(7): p. 639-645.
248. Barbaro, M., et al., *A CMOS, fully integrated sensor for electronic detection of DNA hybridization*. IEEE Electron Device Letters, 2006. **27**(7): p. 595-597.
249. Thiel, A.J., et al., *In situ surface plasmon resonance imaging detection of DNA hybridization to oligonucleotide arrays on gold surfaces*. Analytical Chemistry, 1997. **69**(24): p. 4948-4956.
250. Hutter, E. and M.-P. Pileni, *Detection of DNA hybridization by gold nanoparticle enhanced transmission surface plasmon resonance spectroscopy*. The Journal of Physical Chemistry B, 2003. **107**(27): p. 6497-6499.
251. Liedberg, B., C. Nylander, and I. Lundström, *Biosensing with surface plasmon resonance—how it all started*. Biosensors and Bioelectronics, 1995. **10**(8): p. i-ix.
252. Van Der Merwe, P.A., *Surface plasmon resonance*. 2001, Oxford University Press: New York, NY, USA. p. 137-170.
253. Piliarik, M., H. Vaisocherová, and J. Homola, *Surface plasmon resonance biosensing*. Biosensors and Biodetection, 2009: p. 65-88.
254. Pockrand, I., et al., *Surface plasmon spectroscopy of organic monolayer assemblies*. Surface Science, 1978. **74**(1): p. 237-244.
255. Liedberg, B., C. Nylander, and I. Lunström, *Surface plasmon resonance for gas detection and biosensing*. Sensors and actuators, 1983. **4**: p. 299-304.
256. Kanai, N., et al., *Surface plasmon resonance sensor*. 2007, Google Patents.
257. Kretschmann, E., *Die bestimmung optischer konstanten von metallen durch anregung von oberflächenplasmaschwingungen*. Zeitschrift für Physik, 1971. **241**(4): p. 313-324.
258. McDonnell, J.M., *Surface plasmon resonance: towards an understanding of the mechanisms of biological molecular recognition*. Current opinion in chemical biology, 2001. **5**(5): p. 572-577.
259. Campbell, K., et al., *Comparison of ELISA and SPR biosensor technology for the detection of paralytic shellfish poisoning toxins*. Journal of Chromatography B, 2009. **877**(32): p. 4079-4089.
260. Yman, I.M., et al., *Food allergen detection with biosensor immunoassays*. Journal of AOAC International, 2006. **89**(3): p. 856-861.
261. Homola, J. and S.S. Yee, *Novel polarization control scheme for spectral surface plasmon resonance sensors*. Sensors and Actuators B: Chemical, 1998. **51**(1): p. 331-339.
262. Yu, F., et al., *Attomolar sensitivity in bioassays based on surface plasmon fluorescence spectroscopy*. Journal of the American Chemical Society, 2004. **126**(29): p. 8902-8903.
263. Sharma, A.K., R. Jha, and B. Gupta, *Fiber-optic sensors based on surface plasmon resonance: a comprehensive review*. IEEE Sensors Journal, 2007. **7**(8): p. 1118-1129.



264. Nelson, B.P., et al., *Surface plasmon resonance imaging measurements of DNA and RNA hybridization adsorption onto DNA microarrays*. Analytical chemistry, 2001. **73**(1): p. 1-7.
265. Suraniti, E., et al., *Real-time detection of lymphocytes binding on an antibody chip using SPR imaging*. Lab on a Chip, 2007. **7**(9): p. 1206-1208.
266. Willets, K.A. and R.P. Van Duyne, *Localized surface plasmon resonance spectroscopy and sensing*. Annu. Rev. Phys. Chem., 2007. **58**: p. 267-297.
267. Sepúlveda, B., et al., *LSPR-based nanobiosensors*. Nano Today, 2009. **4**(3): p. 244-251.
268. Haes, A.J., et al., *A localized surface plasmon resonance biosensor: First steps toward an assay for Alzheimer's disease*. Nano Letters, 2004. **4**(6): p. 1029-1034.
269. Gouesbet, G., *Generalized lorenz-mie theory and applications*. Particle & particle systems characterization, 1994. **11**(1): p. 22-34.
270. Qian, X.-M. and S. Nie, *Single-molecule and single-nanoparticle SERS: from fundamental mechanisms to biomedical applications*. Chemical Society Reviews, 2008. **37**(5): p. 912-920.
271. Blaber, M.G., et al., *LSPR imaging of silver triangular nanoprisms: correlating scattering with structure using electrostatics for plasmon lifetime analysis*. The Journal of Physical Chemistry C, 2011. **116**(1): p. 393-403.
272. Piliarik, M., et al., *High-resolution biosensor based on localized surface plasmons*. Optics express, 2012. **20**(1): p. 672-680.
273. Jensen, T.R., et al., *Nanosphere lithography: tunable localized surface plasmon resonance spectra of silver nanoparticles*. The Journal of Physical Chemistry B, 2000. **104**(45): p. 10549-10556.
274. Goss, C.A., D.H. Charych, and M. Majda, *Application of (3-mercaptopropyl) trimethoxysilane as a molecular adhesive in the fabrication of vapor-deposited gold electrodes on glass substrates*. Analytical Chemistry, 1991. **63**(1): p. 85-88.
275. Sharpe, J.C., et al., *Gold nanohole array substrates as immunobiosensors*. Analytical chemistry, 2008. **80**(6): p. 2244-2249.
276. Anker, J.N., et al., *Detection and identification of bioanalytes with high resolution LSPR spectroscopy and MALDI mass spectrometry*. The Journal of Physical Chemistry C, 2009. **113**(15): p. 5891-5894.
277. Cao, W., et al., *Localized surface plasmon resonance of single silver nanoparticles studied by dark-field optical microscopy and spectroscopy*. Journal of applied physics, 2011. **109**(3): p. 034310.
278. Aaron, J., et al., *Dynamic imaging of molecular assemblies in live cells based on nanoparticle plasmon resonance coupling*. Nano letters, 2009. **9**(10): p. 3612-3618.
279. Fairbairn, N., et al., *Hyperspectral darkfield microscopy of single hollow gold nanoparticles for biomedical applications*. Physical Chemistry Chemical Physics, 2013. **15**(12): p. 4163-4168.
280. Kreuzer, M.P., et al., *Colloidal-based localized surface plasmon resonance (LSPR) biosensor for the quantitative determination of stanozolol*. Analytical and bioanalytical chemistry, 2008. **391**(5): p. 1813-1820.

281. Hall, W.P., S.N. Ngatia, and R.P. Van Duyne, *LSPR Biosensor Signal Enhancement Using Nanoparticle–Antibody Conjugates*. The Journal of Physical Chemistry C, 2011. **115**(5): p. 1410-1414.
282. Mukherjee, P., et al., *Fungus-mediated synthesis of silver nanoparticles and their immobilization in the mycelial matrix: a novel biological approach to nanoparticle synthesis*. Nano Letters, 2001. **1**(10): p. 515-519.
283. Grzelczak, M., et al., *Shape control in gold nanoparticle synthesis*. Chemical Society Reviews, 2008. **37**(9): p. 1783-1791.
284. Laurent, S., et al., *Magnetic iron oxide nanoparticles: synthesis, stabilization, vectorization, physicochemical characterizations, and biological applications*. Chemical reviews, 2008. **108**(6): p. 2064-2110.
285. Hanemann, T. and D.V. Szabó, *Polymer-nanoparticle composites: from synthesis to modern applications*. Materials, 2010. **3**(6): p. 3468-3517.
286. Trewyn, B.G., et al., *Synthesis and functionalization of a mesoporous silica nanoparticle based on the sol–gel process and applications in controlled release*. Accounts of Chemical Research, 2007. **40**(9): p. 846-853.
287. Panáček, A., et al., *Silver colloid nanoparticles: synthesis, characterization, and their antibacterial activity*. The Journal of Physical Chemistry B, 2006. **110**(33): p. 16248-16253.
288. Jin, R., et al., *Photoinduced conversion of silver nanospheres to nanoprisms*. Science, 2001. **294**(5548): p. 1901-1903.
289. Sun, Y. and Y. Xia, *Shape-controlled synthesis of gold and silver nanoparticles*. Science, 2002. **298**(5601): p. 2176-2179.
290. Sun, Y., et al., *Uniform silver nanowires synthesis by reducing AgNO<sub>3</sub> with ethylene glycol in the presence of seeds and poly (vinyl pyrrolidone)*. Chemistry of Materials, 2002. **14**(11): p. 4736-4745.
291. Lohse, S.E. and C.J. Murphy, *The quest for shape control: a history of gold nanorod synthesis*. Chemistry of Materials, 2013. **25**(8): p. 1250-1261.
292. Zhang, J., et al., *Plasmon-Mediated Synthesis of Silver Triangular Bipyramids*. Angewandte Chemie, 2009. **121**(42): p. 7927-7931.
293. Wu, C.-H. and K. Sokolov, *Synthesis of immunotargeted magneto-plasmonic nanoclusters*. Journal of visualized experiments: JoVE, 2014(90).
294. Xue, C., et al., *Plasmon-Driven Synthesis of Triangular Core–Shell Nanoprisms from Gold Seeds*. Angewandte Chemie, 2007. **119**(44): p. 8588-8591.
295. Wiley, B., et al., *Shape-controlled synthesis of metal nanostructures: the case of silver*. Chemistry–A European Journal, 2005. **11**(2): p. 454-463.
296. Busbee, B.D., S.O. Obare, and C.J. Murphy, *An Improved Synthesis of High-Aspect-Ratio Gold Nanorods*. Advanced Materials, 2003. **15**(5): p. 414-416.
297. Jin, R., et al., *Controlling anisotropic nanoparticle growth through plasmon excitation*. Nature, 2003. **425**(6957): p. 487-490.
298. Yang, Y., et al., *Solvothermal synthesis of multiple shapes of silver nanoparticles and their SERS properties*. The Journal of Physical Chemistry C, 2007. **111**(26): p. 9095-9104.

299. Zhang, Q., et al., *Seeded growth of uniform Ag nanoplates with high aspect ratio and widely tunable surface plasmon bands*. Nano letters, 2010. **10**(12): p. 5037-5042.
300. Zhang, Q., et al., *A systematic study of the synthesis of silver nanoplates: is citrate a "magic" reagent?* Journal of the American Chemical Society, 2011. **133**(46): p. 18931-18939.
301. Aherne, D., et al., *Optical properties and growth aspects of silver nanoprisms produced by a highly reproducible and rapid synthesis at room temperature*. Advanced Functional Materials, 2008. **18**(14): p. 2005-2016.
302. Seifert, H., et al., *Bloodstream infection in neutropenic cancer patients related to short-term nontunnelled catheters determined by quantitative blood cultures, differential time to positivity, and molecular epidemiological typing with pulsed-field gel electrophoresis*. Journal of clinical microbiology, 2003. **41**(1): p. 118-123.
303. Roe, M.T., E. Vega, and S.D. Pillai, *Antimicrobial resistance markers of class 1 and class 2 integron-bearing Escherichia coli from irrigation water and sediments*. Emerging infectious diseases, 2003. **9**(7): p. 822-826.
304. Micheltore, R.W., I. Paran, and R. Kesseli, *Identification of markers linked to disease-resistance genes by bulked segregant analysis: a rapid method to detect markers in specific genomic regions by using segregating populations*. Proceedings of the National Academy of Sciences, 1991. **88**(21): p. 9828-9832.
305. Perez-Roth, E., et al., *Multiplex PCR for Simultaneous Identification of Staphylococcus aureus and Detection of Methicillin and Mupirocin Resistance*. Journal of Clinical Microbiology, 2001. **39**(11): p. 4037-4041.
306. Mahjoob, S., K. Vafai, and N.R. Beer, *Rapid microfluidic thermal cycler for polymerase chain reaction nucleic acid amplification*. International Journal of Heat and Mass Transfer, 2008. **51**(9): p. 2109-2122.
307. Ottesen, E.A., et al., *Microfluidic digital PCR enables multigene analysis of individual environmental bacteria*. science, 2006. **314**(5804): p. 1464-1467.
308. Focke, M., et al., *Centrifugal microfluidic system for primary amplification and secondary real-time PCR*. Lab on a Chip, 2010. **10**(23): p. 3210-3212.
309. Zhong, Q., et al., *Multiplex digital PCR: breaking the one target per color barrier of quantitative PCR*. Lab on a Chip, 2011. **11**(13): p. 2167-2174.
310. Park, S., et al., *Advances in microfluidic PCR for point-of-care infectious disease diagnostics*. Biotechnology advances, 2011. **29**(6): p. 830-839.
311. Hegner, M., P. Wagner, and G. Semenza, *Immobilizing DNA on gold via thiol modification for atomic force microscopy imaging in buffer solutions*. FEBS letters, 1993. **336**(3): p. 452-456.
312. Huang, C., et al., *Gold nanoring as a sensitive plasmonic biosensor for on-chip DNA detection*. Applied Physics Letters, 2012. **100**(17): p. 173114.
313. Alivisatos, A.P., et al., *Organization of nanocrystal molecules' using DNA*. Nature, 1996. **382**(6592): p. 609-611.
314. Ma, Z., et al., *Optical DNA detection based on gold nanorods aggregation*. Analytica chimica acta, 2010. **673**(2): p. 179-184.

315. Si, G., et al., *Incident-angle dependent color tuning from a single plasmonic chip*. Nanotechnology, 2014. **25**(45): p. 455203.
316. Zhang, Y., Y. Liu, and S. Wang, *Digital mirror device application in reduction of wave-front phase errors*. Sensors, 2009. **9**(4): p. 2345-2351.
317. Maron, P.-A., et al., *Metaproteomics: a new approach for studying functional microbial ecology*. Microbial Ecology, 2007. **53**(3): p. 486-493.
318. Davey, H.M. and D.B. Kell, *Flow cytometry and cell sorting of heterogeneous microbial populations: the importance of single-cell analyses*. Microbiological reviews, 1996. **60**(4): p. 641-696.
319. Izzo, I., et al., *Modeling and experimental validation of a piezoelectric micropump with novel no-moving-part valves*. Sensors and Actuators A: Physical, 2007. **133**(1): p. 128-140.
320. Forster, F.K., et al., *Design, fabrication and testing of fixed-valve micro-pumps*. ASME-PUBLICATIONS-FED, 1995. **234**: p. 39-44.
321. Lee, H.H., et al., *Recirculating flow accelerates DNA microarray hybridization in a microfluidic device*. Lab on a Chip, 2006. **6**(9): p. 1163-1170.
322. Flechsig, G.-U., et al., *DNA hybridization detection at heated electrodes*. Langmuir, 2005. **21**(17): p. 7848-7853.
323. Nabavi, M., *Steady and unsteady flow analysis in microdiffusers and micropumps: a critical review*. Microfluidics and nanofluidics, 2009. **7**(5): p. 599-619.
324. Thompson, S., H. Ma, and C. Wilson, *Investigation of a flat-plate oscillating heat pipe with Tesla-type check valves*. Experimental Thermal and Fluid Science, 2011. **35**(7): p. 1265-1273.
325. Chung, Y.-C., et al., *Microfluidic chip for fast nucleic acid hybridization*. Lab on a Chip, 2003. **3**(4): p. 228-233.
326. Chow, K.-F., F. Mavr e, and R.M. Crooks, *Wireless electrochemical DNA microarray sensor*. Journal of the American Chemical Society, 2008. **130**(24): p. 7544-7545.
327. Hegde, P., et al., *A concise guide to cDNA microarray analysis*. Biotechniques, 2000. **29**(3): p. 548-563.
328. Gorsuch, J. and S. Klaine, *Toxicity and fate of silver in the environment*. Environmental Toxicology and Chemistry, 1998. **17**(4): p. 537-538.
329. Xue, C., et al., *Mechanistic study of photomediated triangular silver nanoprism growth*. Journal of the American Chemical Society, 2008. **130**(26): p. 8337-8344.
330. Li, N., et al., *H<sub>2</sub>O<sub>2</sub>-Aided Seed-Mediated Synthesis of Silver Nanoplates with Improved Yield and Efficiency*. ChemPhysChem, 2012. **13**(10): p. 2526-2530.
331. Parnklang, T., et al., *H<sub>2</sub>O<sub>2</sub>-triggered shape transformation of silver nanospheres to nanoprisms with controllable longitudinal LSPR wavelengths*. RSC Advances, 2013. **3**(31): p. 12886-12894.
332. Maheux, A.F., et al., *Rapid Concentration and Molecular Enrichment Approach for Sensitive Detection of Escherichia coli/Shigella in Potable Water Samples*. Applied and environmental microbiology, 2011: p. AEM. 02337-10.

333. Lee, C., et al., *Absolute and relative QPCR quantification of plasmid copy number in Escherichia coli*. Journal of biotechnology, 2006. **123**(3): p. 273-280.
334. Kohara, Y., K. Akiyama, and K. Isono, *The physical map of the whole E. coli chromosome: application of a new strategy for rapid analysis and sorting of a large genomic library*. Cell, 1987. **50**(3): p. 495-508.
335. Lapizco-Encinas, B.H., et al., *Dielectrophoretic concentration and separation of live and dead bacteria in an array of insulators*. Analytical chemistry, 2004. **76**(6): p. 1571-1579.
336. Morgan, H. and N.G. Green, *Dielectrophoretic manipulation of rod-shaped viral particles*. Journal of Electrostatics, 1997. **42**(3): p. 279-293.
337. Moon, H.-S., et al., *Dielectrophoretic separation of airborne microbes and dust particles using a microfluidic channel for real-time bioaerosol monitoring*. Environmental science & technology, 2009. **43**(15): p. 5857-5863.
338. Kutter, J.P., S.C. Jacobson, and J.M. Ramsey, *Solid phase extraction on microfluidic devices*. Journal of Microcolumn Separations, 2000. **12**(2): p. 93-97.
339. Macounova, K., et al., *Generation of natural pH gradients in microfluidic channels for use in isoelectric focusing*. Analytical chemistry, 2000. **72**(16): p. 3745-3751.
340. Nie, X.-M., et al., *Plasmonic ELISA for the ultrasensitive detection of Treponema pallidum*. Biosensors and Bioelectronics, 2014. **58**: p. 314-319.
341. Xu, X.-H.N., et al., *Real-time probing of membrane transport in living microbial cells using single nanoparticle optics and living cell imaging*. Biochemistry, 2004. **43**(32): p. 10400-10413.

## VITA

Jason Michael Haber was born in Houston, Texas on July 25, 1988 to Steven and Leslie Haber. He graduated as valedictorian from Memorial Senior High School in 2006 and enrolled at the Georgia Institute of Technology in the Biomedical Engineering department. During this time, he picked up a fondness for instrumentation, electronic devices and multidisciplinary research. He completed his Bachelors of Science in Biomedical Engineering with highest honors in 2010 and immediately enrolled at the University of Texas at Austin Department of Biomedical Engineering for graduate studies under the supervision of Dr. Peter Gascoyne. In 2013, Dr. Konstantin Sokolov agreed to be his co-supervisor, and he joined the Biomedical Optics and Nanodiagnostics Lab.

Permanent Address: 3131 West Bellfort Avenue #1018, Houston, TX 77054

This dissertation was typed by the author.